A Numerical Method for Doubly-Periodic Stokes Flow in 3D with and without a Bounding Plane

AN ABSTRACT
SUBMITTED ON THE FIFTEENTH DAY OF APRIL, 2015
TO THE DEPARTMENT OF MATHEMATICS
OF THE SCHOOL OF SCIENCE AND ENGINEERING OF
TULANE UNIVERSITY
IN PARTIAL FULFILLMENT OF THE REQUIREMENTS
FOR THE DEGREE OF
DOCTOR OF PHILOSOPHY
BY

_____

FRANZ HOFFMANN

APPROVED: _____
RICARDO CORTEZ
CHAIRMAN

_____
LISA FAUCI

_____
JAMES (MAC) HYMAN

_____
MORRIS KALKA

_____
KUN ZHAO

Abstract

A numerical method for computing three-dimensional Stokes flow driven by a doubly-periodic array of regularized forces is presented. In the non-periodic direction either a free boundary or a homogeneous Dirichlet condition is enforced. The method consists of finding a regularized Green's function in Fourier space analytically. Then only an inverse fast Fourier transform (inverse FFT) has to be computed. Accuracy is verified by comparing numerical results to a solution that is independent of the method. In an Ewald splitting, the FFT method can be used to compute the smooth component of the flow, which allows for a splitting parameter as small as a few grid cells. This selection makes the sum in physical space converge extremely fast. Numerical examples demonstrate that fact. Since the forces are regularized, in some cases splitting is not even needed, depending on the relative sizes of the numerical parameters. The method is applied to model the flow created by carpets of nodal cilia based on cilium shape.

A Numerical Method for Doubly-Periodic Stokes Flow in 3D with and without a Bounding Plane

A DISSERTATION
SUBMITTED ON THE FIFTEENTH DAY OF APRIL, 2015
TO THE DEPARTMENT OF MATHEMATICS
OF THE SCHOOL OF SCIENCE AND ENGINEERING OF
TULANE UNIVERSITY
IN PARTIAL FULFILLMENT OF THE REQUIREMENTS
FOR THE DEGREE OF
DOCTOR OF PHILOSOPHY
BY

_____

FRANZ HOFFMANN

APPROVED: _____
RICARDO CORTEZ
CHAIRMAN

_____
LISA FAUCI

_____
JAMES (MAC) HYMAN

_____
MORRIS KALKA

_____
KUN ZHAO

Acknowledgement

Most importantly I owe special thanks to my thesis advisor RICARDO CORTEZ for his ideas, comments and questions that fundamentally shaped and significantly improved my research itself as well the form it is presented in. I am particularly grateful that he always found time to talk whenever I asked for advice while at the same time leaving me great amounts of freedom to pursue my own ideas.

Let me continue by thanking the people whose contributions and support have directly impacted the presented work[1]: ELHAM (ELLIE) AHMADI for her continued interest in my work over many years and for being a supportive office mate in many regards, FOREST MANNAN for his continued challenging of my understanding of computational mathematics as well as for keeping up the spirits at the most dreadful times, JACEK WROBEL for engaging and entertaining discussions about Stokes flow as well as for leading our weekly group discussions that extended my scope well beyond just my own dissertation research, ARMIN STRAUB (now at University of Illinois at Urbana-Champaign) for contributing to the summation in the appendix but more importantly for being an inspiring teacher, roommate and friend, as well as TEWODROS (TEDDY) AMDEBERHAN for providing the proof to Lemma B.3.1 but more importantly for showing me the ropes first as his a teaching assistant and later when I taught my own classes. I also want to extend my thanks to my dissertation committee members LISA FAUCI, JAMES (MAC) HYMAN, MORRIS KALKA and KUN

---

[1] Neither here nor in the following is the order in which their names are mentioned intended to diminish the importance of any of their contributions.

ZHAO. Mac Hyman was also an integral part in our establishing a SIAM[2] student chapter at Tulane University.

A special thanks is also due to the people who profoundly impacted my mathematical upbringing: KYLE HICKMAN (now at Los Alamos National Lab) for sharing his interest and knowledge in virtually any area of mathematics as well as for making the office more fun, SUSH MAJHI for spreading his curiosity and admiration for mathematics and for being extremely funny, LIN JIU and JAMES SALVATORE for lively discussions about pure mathematics and for organizing tea time, SHUMO CUI for long nights of coding, HIDEKI FUJIOKA for sharing his profound knowledge of mathematics, computers and Python in particular, KARL and ISOLDE HOFMANN for bringing me to Tulane University and New Orleans in the first place, as well as KARL-HERMANN NEEB (now at Universität Erlangen) for teaching the clearest mathematics class I have ever taken (Analysis I at TU Darmstadt) and for providing free of charge beautifully written lecture notes covering analysis, linear algebra, abstract algebra and topology. Finally I want to thank my parents ERIKA and MICHAEL HOFFMANN for their continuous support and love over the years.

Lastly, let me share my deepest gratitude towards the many contributers to LaTeX, Python and Ubuntu as well as to the multitude of people who have posted questions, comments, answers and excerpts of their code on various websites, most notably on STACKOVERFLOW.

---

[2] Society for Industrial and Applied Mathematics

List of Tables

List of Figures

Contents

Chapter 1

Introduction

We present an efficient numerical method to compute three-dimensional Stokes flow that is periodic in two space dimensions. While doubly-periodic Stokes flow is interesting from a fundamental point of view, we are motivated by the particular example of flow generated by carpets of *cilia*. Cilia are hair-like structures that attach to the surfaces of cells and move the surrounding fluid through coordinated beating (Figure 1.1). The beat cycle of a cilium consist of two parts. The *effective* stroke moves fluid in the preferred direction while the *recovery* stroke is in the opposite direction. During the recovery stroke the cilium moves closer to the cell surface where fluid is slowed down by surface interactions. Therefore, in total more fluid is moved in the direction of the effective stroke (Figure 1.2(a)). In the human body cilia drive fluid exchange in the ventricles of the brain and transport mucus in the sinuses and lungs (*pulmonary* cilia) [MN06]. We focus on *nodal* cilia, which rotate along the lateral surface of an imaginary cone with constant velocity. If the cone is tilted with respect to the cell surface, fluid above the cilium is transported in the direction of the cilium motion when the cilium is the most upright [dTO13] (Figure 1.2(b)). In nature nodal cilia are responsible for left-right asymmetry in vertebrae development [MN06]. Recently synthetic nodal cilia actuated by an exter-
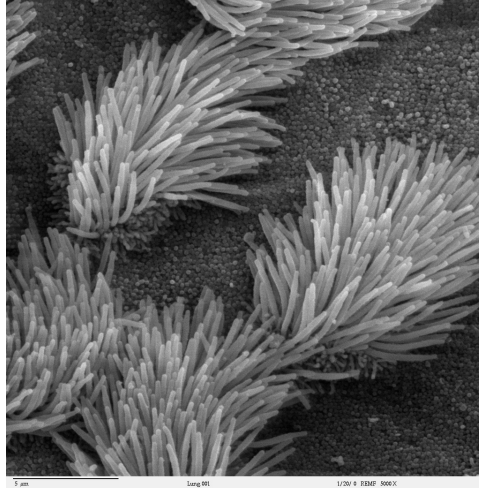
Figure 1.1: Scanning electron microscope (SEM) micrograph of cilia in the human lungs. *Source:* This image is public domain. *Author*: Charles Daghlian, Dartmouth College. *File*: ☞ http://remf.dartmouth.edu/images/mammalianLungSEM/source/9.html. *License*: ☞ http://remf.dartmouth.edu/imagesindex.html.

nal magnetic field were proven experimentally to create fluid mixing [CCLH13] and transport [VPK⁺10, SFE⁺10, WGW⁺13, WGW⁺14].

In many applications it is crucial to analyze the fluid flow close to the individual cilium, which requires a detailed model with fine resolution. On the other hand the fluid flow around a cilium is significantly influenced by the motion of surrounding cilia, which requires a larger scale. For example, cilia can transport fluid more efficiently if instead of beating in perfect synchrony there is a slight phase difference between neighboring cilia. Because of the appearance of a traveling wave, this process is referred to as *metachronal wave*. Numerical models, therefore, have to incorporate the effects of large arrays of cilia while at the same time allowing to resolve individual cilia accurately. An obvious approach is to compute large numbers of individual cilia [GLG98, SGB07, SBG08, DNMNK14], which captures both near-field and far-field effects but is computationally expensive. Instead, in our method we use only a few cilia, for instance comprising one metachronal wave length, and enforce periodic boundary conditions in two spatial dimensions.

It should be pointed out that besides just saving computational time, periodic boundary conditions can also profoundly change fundamental properties of the sys-
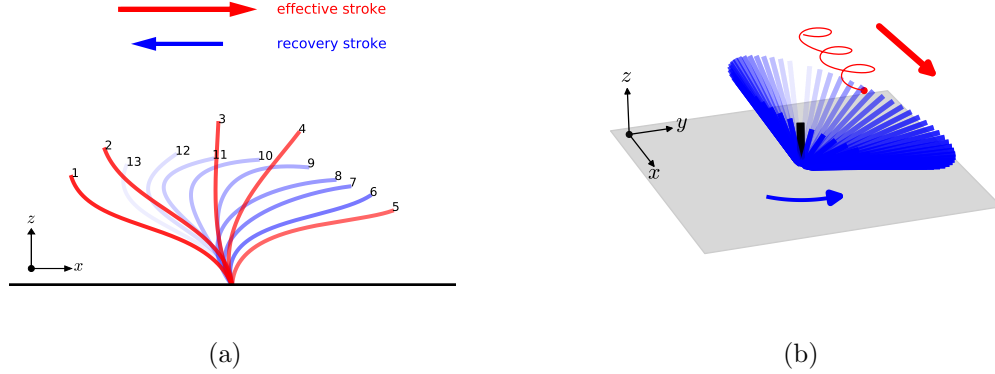
Figure 1.2: Beat pattern of (a) a pulmonary cilium [SS81, FB86] and (b) a nodal cilium. In both cases the fluid above the cilium is transported in the direction of the cilium motion when the cilium is the most upright (positive x-direction). *Source:* (a) pulmonary_cilium.py. (b) trajectory_from_forces_3D.py.

tem. Lenz and Ryskin, who analyzed analytically and numerically the evolution of the phase difference between neighboring cilia in one-dimensional arrays [LR06], found that for general beat patterns the metachronal wave is unstable for free boundary conditions but stable for periodic boundary conditions. A number of numerical methods use periodic boundary conditions to model ciliary arrays. Elgeti and Gompper imposed periodic boundary conditions for two-dimensional arrays of cilia using multiparticle collision dynamics, where the fluid is represented by point particles with unit mass [EG13]. Mitran modeled rows of pulmonary cilia using a flexible grid around each cilium and enforced periodic boundary conditions on a background Cartesian grid [Mit07]. Khaderi et al. and Gauger et al. proposed two-dimensional models incorporating periodicity in one spatial variable for artificial cilia that take into account interactions of an external magnetic field, cilia geometry and fluid flow [GDS09, KdTO11]. In the approach presented here, a simple model gives the doubly-periodic three-dimensional velocity field based on forces that come from a prescribed cilium shape.

1.1 Mathematical model

Our goal is to compute fluid velocity based on the shape of the cilium during its beat cycle. The procedure consist of the following steps.

$$\begin{array}{ccccccc} \text{shape} & \xrightarrow{1.} & \text{velocity} & \xrightarrow{2.} & \text{force exerted} & \xrightarrow{3.} & \text{fluid velocity} \\ \text{of cilium} & & \text{of cilium} & & \text{by cilium} & & \text{everywhere} \end{array} \qquad (*)$$

Step 1 is readily performed by differentiating. Steps 2 and 3 require that we understand the relationship between force and velocity. As length scales are tiny[1], fluid flow is governed by *Stokes equation*. As a result, velocity depends linearly on force, which for us has to profound implications. (a) We can decompose the fluid velocity due to a complex force distribution into so-called *fundamental solutions*, which describes the fluid velocity due to an individual point force. In particular, representing the force distribution along the cilium by finitely many point forces, the resulting fluid velocity is simply the sum of the fundamental solutions corresponding to each point force (Step 3). (b) The relationship between force and velocity is easy to invert. In particular, prescribing the velocity at n points along the cilium, we can find the strengths of n many point forces that recreated these velocities by solving an n by n linear system (Step 2).

Our task is now to find the fundamental solution that satisfies the boundary conditions of our problem (Figure 1.3), which will enable us to perform algorithm $(*)$.

Task. *Find a fundamental solution* $\mathbf{u}$ *to Stokes equation, where*

I. $\mathbf{u}$ *is periodic in* x *and* y,

II. $\mathbf{u} = \mathbf{0}$ *at the infinite plane* $z = 0$.

---

[1] Pulmonary cilia are about 5-6μm [FB86] while synthetic cilia are typically 10-100μm [dTO13].

In 1896 Lorentz derived a fundamental solution analytically in the absence of any boundaries, the co-called free space *Stokeslet* [Lor96]. The Stokeslet is singular at the force location. As a way of removing singularity, we change the corresponding point force to a smooth force field. The resulting velocity field is smooth throughout the domain while approximating the Stokeslet away from the force location and is called a *regularized Stokeslet* [Cor01]. In 1971 Blake derived a singular fundamental solution satisfying condition ***II*** using the *method of images* [Bla71a]. The fluid velocity is written as the sum of a Stokeslet and the velocity fields due to so-called image elements, which are defined to be derivatives of a Stokeslet whose singularity lies outside of the computational domain. The image system of a regularized Stokeslet is also known [ADE+08, CV15]. The novelty of our work is that we, at least numerically, compute a regularized fundamental solution satisfying conditions ***I*** and ***I+II***, respectively. In other words, we compute the doubly-periodic regularized Stokeslet and its image system. Previously our results have been published as follows.

I. Ricardo Cortez and Franz Hoffmann. A fast numerical method for computing doubly-periodic regularized Stokes flow in 3D. *Journal of Computational Physics*, 258:1-14, 2014.

I+II. Franz Hoffmann and Ricardo Cortez. Numerical treatment of nodal cilia using doubly-periodic regularized Stokes flow. *in preparation.*

About *I*. We follow the derivation of the free space Stokeslet, which consist of two steps.

1. Solve the *biharmonic equation* for the *Green's function B*

$$\Delta^2 B\left(\mathbf{x}\right) = \delta\left(\mathbf{x} - \mathbf{x}_0\right),\tag{1.1}$$

where Δ is the Lapalce operator and δ is the Dirac delta distribution.

(a)   (b)
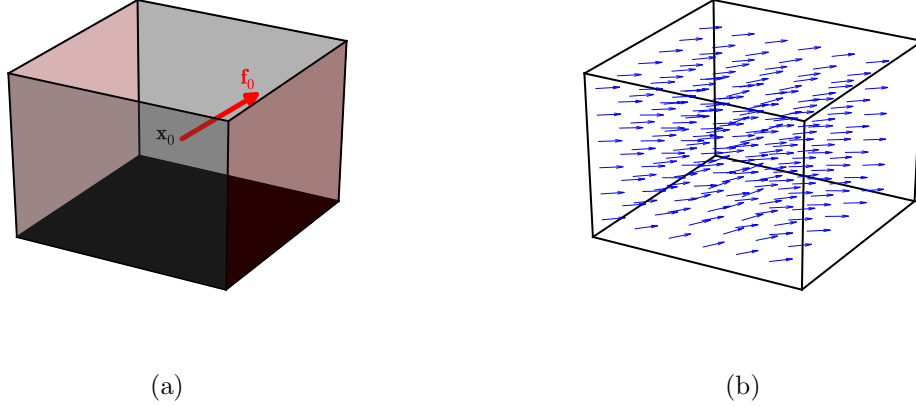
Figure 1.3: (a) For our problem we consider a single point force of strength $\mathbf{f}_0$ at a location $\mathbf{x}_0$. We enforce periodic boundary conditions at the lateral faces and homogeneous Dirichlet boundary conditions at the bottom face of the box. (b) The solution to our problem is the velocity field everywhere in the computational domain. *Source:* cube.py.

2. Apply the differential operator

$$\mu\mathbf{u}\left(\mathbf{x}\right) = \left(\left(\mathbf{f}_0 \cdot \nabla\right)\nabla - \mathbf{f}_0\Delta\right) B\left(\mathbf{x}\right),$$

where $\mathbf{f}_0$ is the strength of the point force at $\mathbf{x}_0$ and μ is the viscosity of the fluid.

The regularized Stokeslet is obtained by replacing the right-hand side in Eq. (1.1) by a family of smooth functions whose distributional limit is the delta function. In order to derive the doubly-periodic regularized Stokeslet we perform the same two steps in Fourier space (with respect to the two periodic directions). As we are able to perform the computations analytically, we obtain an exact expression for the regularized Stokeslet in Fourier space. We take an inverse fast Fourier transform (FFT) to translate our solution back into physical space, which is the only numerical step of our method (Table 1.1).

In order for the inverse FFT to be accurate the solution needs to be smooth. After regularizing Eq. (1.1) our solution is indeed smooth but in some cases additional smoothness is needed. In those cases we split the Green's function B into two pieces, a *fast decaying* and a *regular* piece, which is known as *Ewald splitting*. The regular

Real space   Fourier transform   *Fourier space*

Biharmonic equation	**Biharmonic equation**
↓ solve	↓ solve
Green's function	**Green's function**
↓ differentiate	↓ differentiate
fluid velocity	**fluid velocity**

inverse FFT

doubly-periodic fluid velocity
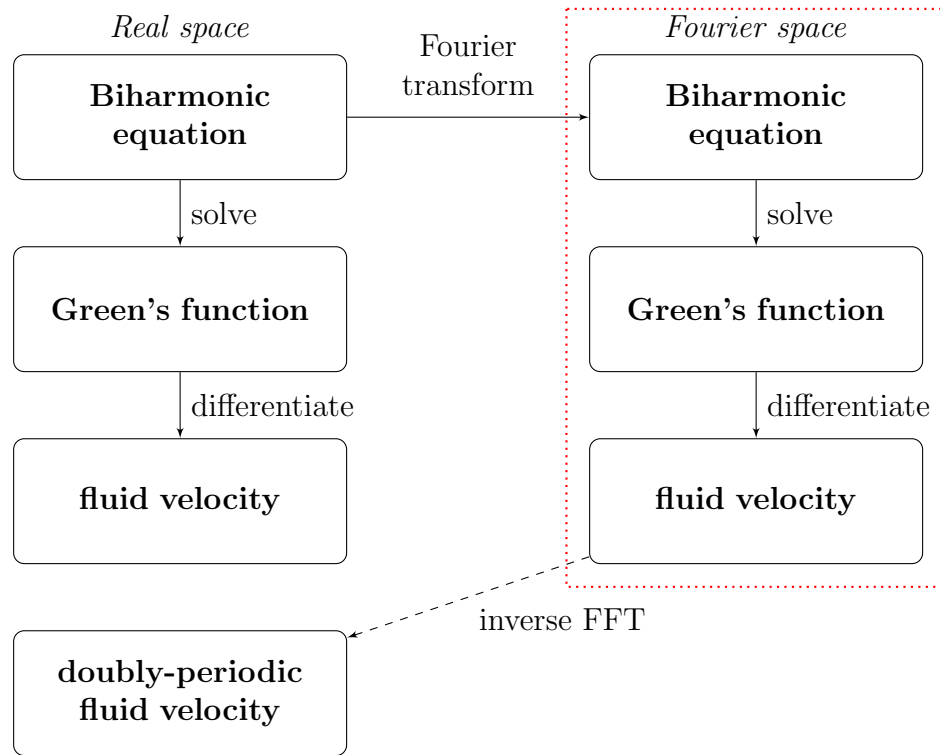
Table 1.1: The fundamental solution to Stokes equation in free space is found by computing the fundamental solution to the biharmonic equation and then applying an appropriate differential operator. In order to find the doubly-periodic fluid velocity we repeat the same steps in Fourier space. All steps are done analytically with the exception of the last step (taking the inverse fast Fourier transform), which is done numerically. A more detailed schematic can be found in Table 3.1.

piece is smooth enough to be treated in Fourier space as described above. The fast decaying piece is computed in physical space. The decay typically happens within one period which makes it is easy to enforce periodicity.

About I+II. We compute the image elements corresponding to the regularized doubly-periodic Stokeslet derived above. We can simply differentiate the exact Fourier space expression of the regularized Stokeslet obtained earlier in order to obtain Fourier space versions of the regularized image elements. Once more, taking an inverse FFT gives the solution in physical space. It is straightforward to generalize the Ewald splitting used above to also include the other image elements.

1.2   Outline of the thesis

In Chapter 2 we review the fundamental solutions derived by Lorentz in free space and by Blake in the presence of a wall as well as their regularized versions. In Chapter 3 we present our method using FFTs first without Ewald splitting and then in Chapter 4 with Ewald splitting. In Chapter 5 we show numerical results from modeling carpets of nodal cilia. In Chapter 6 we sum up our work and present some possible future directions. For a graphical overview see Table 1.2.

1.3   Software

1.3.1   Computer algebra

We use Mathematica® 9 for some analytical computations, in particular computing Fourier transforms, solving ODEs, and some term rearrangements in the appendix. Whenever we use results obtained from Mathematica we provide a link to the respective Mathematica notebook. We also provide the source code as pdf so that it can

be viewed without a `Mathematica` license.

1.3.2 Numerical computation

Our algorithm is implemented in `Python 2.7.3` using the following packages:

- `numpy 1.9.1` for arrays, linear algebra and the Fourier transform [JOP+][2],

- `matplotlib 1.4.3` for plotting [Hun07][3],

- `scipy 0.9.0` for a vectorized version of the error function [JOP+].

Figures.   Under every Figure we provide a link to the respective source code. If the runtime is significantly longer than just a few seconds, we provide two separate routines. One routine creates the data shown in the figure, which is potentially slow, and the other routine plots the figure itself, which is typically fast.

Test cases.   Automated test cases for our core routines are implemented in test-cases.py. If the reader wished to play around with the program we suggest example.py as a start.

---

[2] For the most part packages `numpy 1.6.1` and `matplotlib 1.1.1rc` are sufficient. The newer versions `numpy 1.9.1` and `matplotlib 1.4.3` are only required for the 3D quiver plot in Figure 1.3.

[3] See footnote 2.
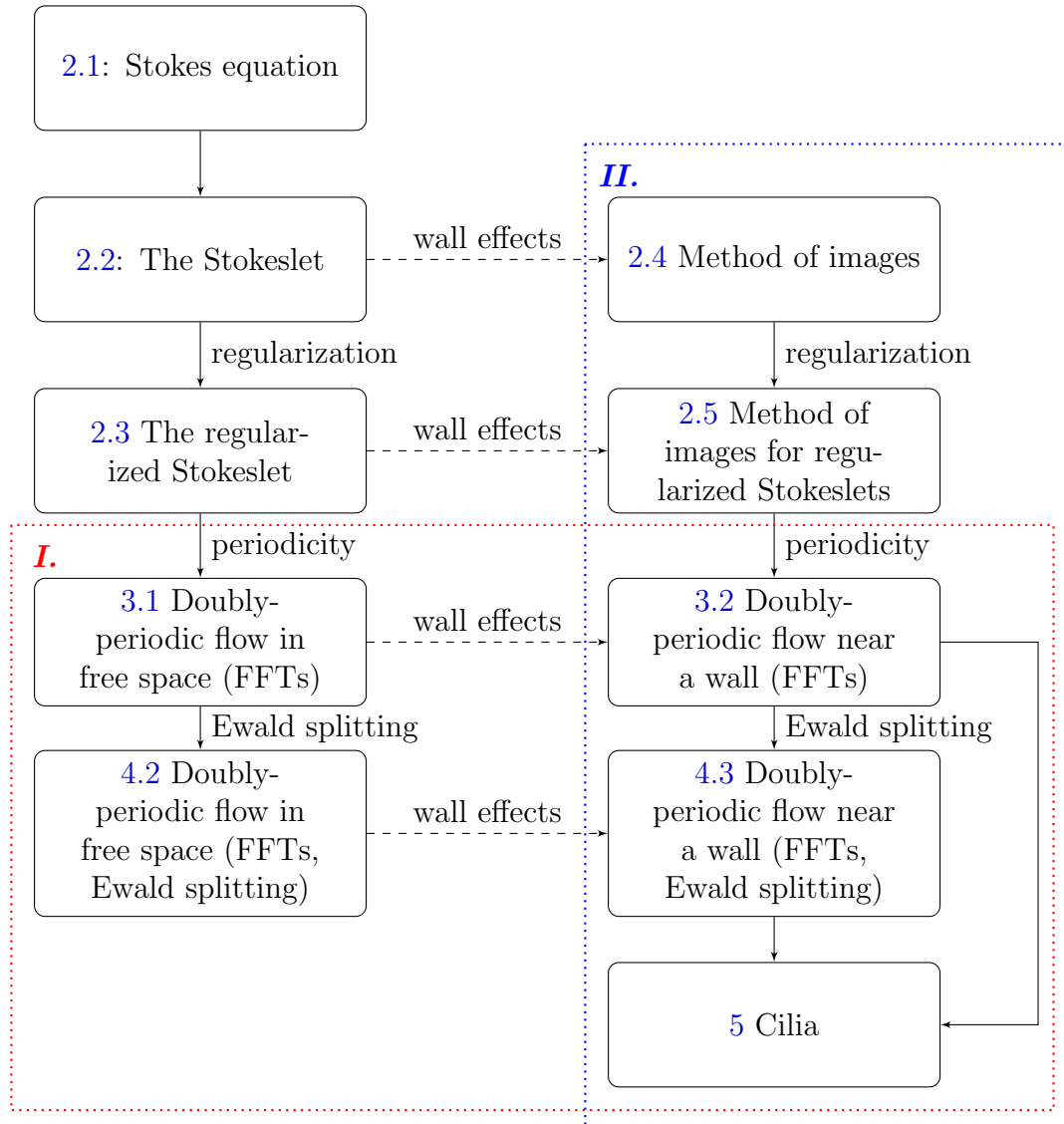
Table 1.2: Interdependence of chapters. *I.* - planar periodicity. *II.* - wall effects.

Chapter 2

Nonperiodic Stokes flow in 3D

2.1 Stokes equation

Life on the micro level is nicely described in a beautiful paper by Purcell [Pur77].

Our goal is to numerically compute the flow field generated by carpets of motile cilia. Mathematically speaking we seek a function $\mathbf{u}$ that for every point $\mathbf{x}$ in the domain of interest gives the velocity vector $\mathbf{u}(\mathbf{x})$ of the moving fluid (see Figure 1.2, right). In order to compute the velocity field we need to know how the cilia move the fluid, that is we need to know the force $\mathbf{F}(\mathbf{x})$ that the cilia exert onto the fluid. The force distribution over the surface of the cilia will give us enough information to compute the velocity field everywhere. In short:

$$\mathbf{F}(\mathbf{x})\bigg|_{\text{cilia}} \overset{\text{algorithm}}{\to} \mathbf{u}(\mathbf{x})\bigg|_{\text{everywhere}}.$$

Since cilia are microscopic organisms[1], it is crucial for our understanding of the governing equations that we familiarize ourselves with the physical environment on a

---

[1] The length scales are about 10-20μm for water-propelling cilia and about 5-6μm for mucus-propelling cilia [FB86].
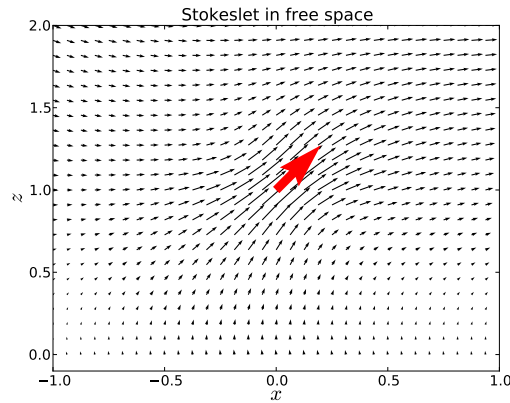
(a) free boundary in x, y and z.
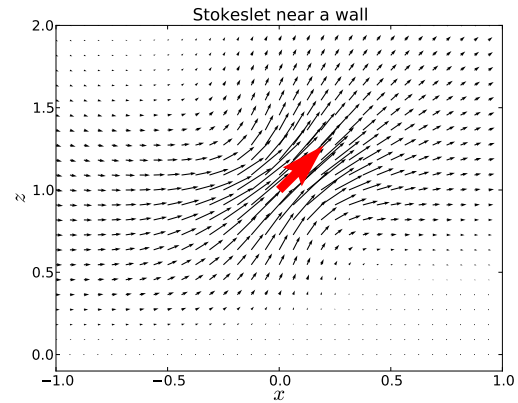
(b) free boundary in x and y, wall at $z = 0$.
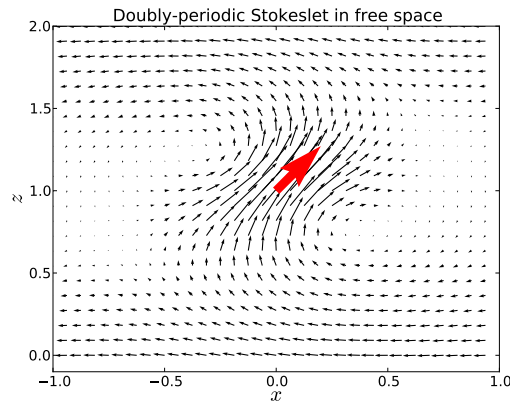
(c) periodic in x and y with period 2, free bound-ary in z.
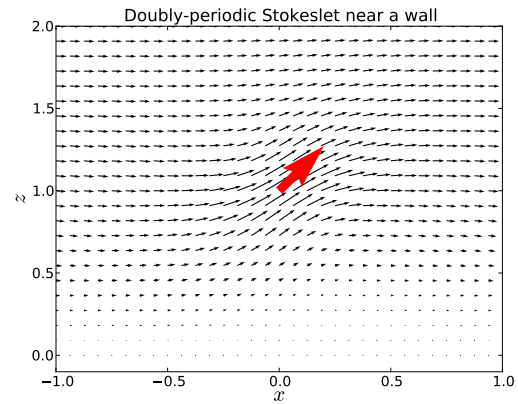
(d) periodic in x and y with period 2, wall at $z = 0$.

Figure 2.1: Flow fields due to a regularized ($\varepsilon = 0.2$) point force $\mathbf{f}_0 = (1, 0, 1)$ centered at $\mathbf{x}_0 = (1, 0, 1)$ under different boundary conditions. The flow fields are shown at the cross section $y = 0$. (c): For the doubly-periodic Stokeslet with no boundary in z the infinite Stokeslet double sum does not converge and only the FFT method gives a finite solution. That solution, however, exhibits some non-intuitive vertical flows near the top and bottom border of the computational domain. (d): For the doubly-periodic Stokeslet near a wall the infinite Stokeslet double sum *does* converge and agrees with the FFT solution. *Source:* stokeslets.py.

micro-level. One might be tempted to think that the fluid environment of a micro-organism is just a scaled-down version of the fluid environment of a similar but larger organism. However, this assumption is *false* because the different forces that are involved do *not* scale down equivalently. For example, consider a spherical drop of water with radius r placed on a flat, impermeable surface surrounded by air. The two competing forces acting on the drop are the gravitational force and surface tension. For a large drop of water, say a bucket load, surface tension is significantly weaker than the gravitational force and as a result the drop will diffuse immediately. As we let the size of the drop tend to zero, the gravitational force scales along with mass and volume as r^3 while surface tension scales along with surface area as r^2. As a result, for a small enough radius r surface tension dominates gravitational forces. Indeed, small drops of water (e.g. raindrops) do *not* diffuse but maintain their size and shape.

For a micro-organism this means that, vaguely speaking, tiny length scales imply tiny mass which implies tiny inertial forces. Therefore, in a micro-fluidic environment viscous forces dominate inertial forces and the resulting flows are called *creeping* or *laminar*. The moral of the story is that the correct macro-scale analog of a micro-organism moving in, say, water is a larger version of the same organism moving in a more viscous fluid like, for instance, honey or glycerin.

The relationship between a force $\mathbf{F}$ and the fluid velocity $\mathbf{u}$ in a highly viscous fluid, and for that matter most micro-fluids, is described by the *Stokes equation* [Bat67, CM00]

$$0 = -\nabla p + \mu \Delta \mathbf{u} + \mathbf{F}, \tag{2.1}$$

together with the *incompressibility condition*

$$0 = \nabla \cdot \mathbf{u}.$$

The parameter μ describes the viscosity of the fluid and is assumed constant. Besides the fluid velocity $\mathbf{u}$ there is a second unknown, the scalar pressure p. When solving Stokes equation we can use the incompressibility condition to decouple the two variables velocity and pressure. As a result, in the following we can focus on the linear relationship between force and velocity. Stokes equation can be obtained by eliminating the inertial terms from the Navier-Stokes equation using dimensional analysis [Poz96, Section 1.1].

At first glance it may seem peculiar that Stokes equation does not depend on time but rather the flow field at any given time is determined by the force configuration at that particular time only. However, this observation is consistent with the lack of inertia, or lack of memory, which means that no kinetic energy from earlier times can be stored in the fluid. As a result the fluid velocity adapts to a change in force instantaneously. Also, since inertia is absent from the flow, so are chaos and turbulence. This fact greatly simplifies mathematical treatment compared to the more complex Navier-Stokes equations and manifests itself in the linear, instantaneous relationship between force and velocity.

2.2 Free-space solution of Stokes equation - The Stokeslet

For some further reading we suggest the classical text from Batchelor [Bat67].

Instead of assuming a continuous force distribution we now represent force as a sum of finitely many point forces, that is

$$\mathbf{F}\left(\mathbf{x}\right) = \sum_{k=1}^{N} \mathbf{f}_k \delta \left(\mathbf{x} - \mathbf{x}_k\right),$$

where $\delta\left(\mathbf{x} - \mathbf{x}_k\right)$ is the Dirac delta function centered at $\mathbf{x}_k$. Because of the linearity of Stokes equation the velocity field due to this force is given by the superposition of the velocity fields due to each individual point force. Without loss of generality we can, therefore, focus on solving

$$0 = -\nabla p + \mu \Delta \mathbf{u} + \mathbf{f}_0 \delta\left(\mathbf{x} - \mathbf{x}_0\right), \tag{2.2}$$

$$0 = \nabla \cdot \mathbf{u}.$$

The fundamental solution to the singularly forced Stokes equation is known as *Stokeslet* or *Oseen tensor* and will be derived in the following. Taking the divergence of Eq. (2.2) and using the incompressibility condition gives

$$0 = -\Delta p + \mathbf{f}_0 \cdot \nabla \delta\left(\tilde{\mathbf{x}}\right),$$

where $\tilde{\mathbf{x}} = \mathbf{x} - \mathbf{x}_0$. The pressure p can, therefore, be written in terms of the *Green's function* G as

$$p = \mathbf{f}_0 \cdot \nabla G\left(\tilde{\mathbf{x}}\right),$$

where G is the fundamental solution to Laplace's equation

$$\Delta G\left(\mathbf{x}\right) = \delta\left(\mathbf{x}\right). \tag{2.3}$$

The function G is unique if we further demand that G goes to 0 as $\mathbf{x}$ goes to infinity, which implies $G = -1/4\pi\left|\mathbf{x}\right|$ (see appendix A.1). This boundary condition is in accordance with our intuition that the effects of a force acting on a fluid should not be felt far away from where the force acts. Plugging p back into Eq. (2.2) we can eliminate pressure to yield

$$0 = -\nabla\left(\mathbf{f}_0 \cdot \nabla G\left(\tilde{\mathbf{x}}\right)\right) + \mu \Delta \mathbf{u} + \mathbf{f}_0 \delta\left(\tilde{\mathbf{x}}\right).$$

In order to find an expression for the fluid velocity we have to solve

$$\Delta \mathbf{u} = \frac{1}{\mu} \left((\mathbf{f}_0 \cdot \nabla) \nabla G(\tilde{\mathbf{x}}) - \mathbf{f}_0 \delta(\tilde{\mathbf{x}}) \right).$$

Defining another Green's function $B = -|\mathbf{x}|/8\pi$ (see appendix A.1) that satisfies

$$\Delta B(\mathbf{x}) = G(\mathbf{x}), \qquad (2.4)$$

we find the Stokeslet

$$\mu \mathbf{u}(\mathbf{x}) = \mathbf{St}_{\mathbf{f}_0}(\tilde{\mathbf{x}})$$
$$= \left((\mathbf{f}_0 \cdot \nabla) \nabla - \mathbf{f}_0 \Delta \right) B(r), \qquad (2.5)$$

where $r = |\tilde{\mathbf{x}}|$. The Stokeslet gives the incompressible[2] velocity field at a point $\mathbf{x}$ due to a point forces of strength $\mathbf{f}_0$ centered at $\mathbf{x}_0$. The flow field associated with a Stokeslet is depicted in Figure 2.1(a). An equivalent formulation is given by (see appendix A.2)

$$\mathbf{St}_{\mathbf{f}_0}(\tilde{\mathbf{x}}) = H_1(r)\mathbf{f}_0 + H_2(r)(\mathbf{f}_0 \cdot \tilde{\mathbf{x}})\tilde{\mathbf{x}}, \qquad (2.6)$$

where

$$H_1(r) = \frac{B'(r)}{r} - G(r) = \frac{1}{8\pi r}, \qquad (2.7)$$
$$H_2(r) = \frac{1}{r}\left(\frac{B'(r)}{r}\right)' = \frac{1}{8\pi r^3}. \qquad (2.8)$$

2.2.1   Summary of the singular Stokeslet

---

[2] In fact, the divergence of Eq. (2.5) is zero for any function B away from the singularity.

> **The Stokeslet**
>
> In Stokes flow the fluid velocity $\mathbf{u}$ at a point $\mathbf{x}$ due to a *singular* point force with strength $\mathbf{f}_0$ centered at $\mathbf{x}_0$ is given by
>
> $$\mu\mathbf{u}\left(\mathbf{x}\right) = H_1(r)\mathbf{f}_0 + H_2(r)\left(\mathbf{f}_0 \cdot \tilde{\mathbf{x}}\right)\tilde{\mathbf{x}},$$
>
> where $\tilde{\mathbf{x}} = \mathbf{x} - \mathbf{x}_0$, $r = |\tilde{\mathbf{x}}|$ and
>
> $$H_1(r) = \frac{1}{8\pi r}, \qquad\qquad H_2(r) = \frac{1}{8\pi r^3}.$$

2.3 The method of regularized Stokeslets

The method of regularized Stokeslets was derived by Cortez in 2001 [Cor01].

The assumption made in the previous section that a force can be concentrated at a single point leads to a peculiar result. When the Stokeslet (2.5) is evaluated near the force location $\mathbf{x}_0$ the fluid velocity is of order $1/r$, where r is the distance of the evaluation point $\mathbf{x}$ to $\mathbf{x}_0$. The Stokeslet itself is singular at $r = 0$ meaning that the fluid velocity would be infinite right where the force acts. In order to remedy the situation we spread the point force over a small region instead of concentrating it at a single point [Cor01] (see Figure 2.2). Mathematically this is equivalent to replacing the delta function in Stokes Eq. (2.2) with a smooth function Φ_ε that approximates the delta function in the distributional sense. Such a function Φ_ε we call *blob function* or just *blob* because of its typical shape (see Figure 2.3) The regularization parameter controls the width of the blob so that Φ_ε converges to the Dirac delta function in the distributional sense as $\varepsilon \to 0$.
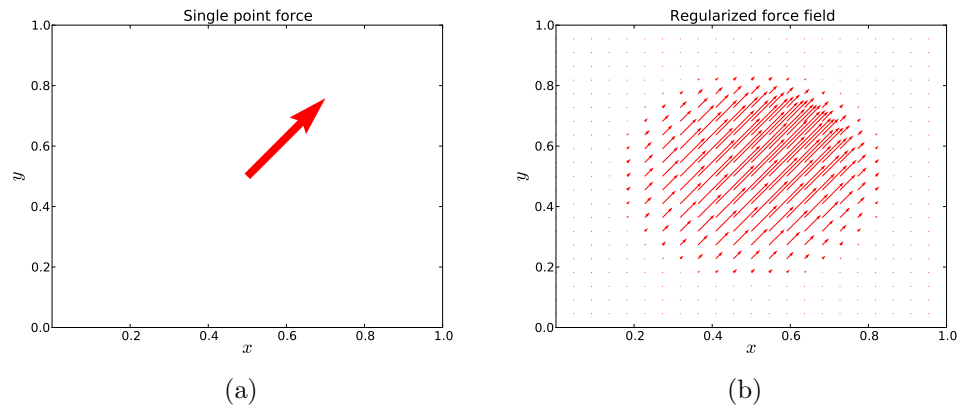
Figure 2.2: (a) The single point force gives rise to the singular Stokeslet in Eq. (2.5). (b) The regularized force field (here $\varepsilon = 0.25$) gives rise to the regularized Stokeslet in Eq. (2.11). *Source:* spread_force.py.
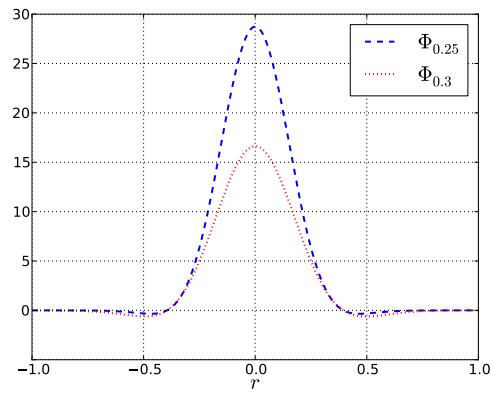
Figure 2.3: A sample blob function Φ_ε for different regularization parameters. The blob is smooth for any $\varepsilon > 0$ but converges to the Dirac delta distribution as $\varepsilon \to 0$. Depicted is the Gaussian blob (2.15) but all blobs share the same characteristic shape, hence the name. *Source:* blobs.py.

The regularized Stokes equation is

$$0 = -\nabla p + \mu \Delta \mathbf{u} + \mathbf{f}_0 \Phi_\varepsilon (\hat{\mathbf{x}}),$$

$$0 = \nabla \cdot \mathbf{u}.$$

Replacing the delta function in Laplace Eqs. (2.3)-(2.4) with a blob Φ_ε gives rise to smooth functions G_{Φ_ε} and B_{Φ_ε} that satisfy

$$\Delta G_{\Phi_\varepsilon}(r) = \Phi_\varepsilon(r), \tag{2.9}$$

$$\Delta B_{\Phi_\varepsilon}(r) = G_{\Phi_\varepsilon}(r). \tag{2.10}$$

The two equations can be solved for the *regularized Green's function's* G_{Φ_ε} and B_{Φ_ε} analytically by rewriting the Laplacian in spherical coordinates, just as we did in the singular case (see Appendix A.1). Replacing the singular Green's function B in Stokeslet Eq. (2.5) with the analytic solution for B_{Φ_ε} gives the *regularized Stokeslet* [Cor01]

$$\mathbf{St}_{\mathbf{f}_0}^{\Phi_\varepsilon} (\tilde{\mathbf{x}}) = ((\mathbf{f}_0 \cdot \nabla) \nabla - \mathbf{f}_0 \Delta) B_{\Phi_\varepsilon} (\hat{\mathbf{x}}) \tag{2.11}$$

$$= H_1^{\Phi_\varepsilon}(r)\mathbf{f}_0 + H_2^{\Phi_\varepsilon}(r) (\mathbf{f}_0 \cdot \tilde{\mathbf{x}}) \tilde{\mathbf{x}}, \tag{2.12}$$

where

$$H_1^{\Phi_\varepsilon}(r) = \frac{B'_{\Phi_\varepsilon}(r)}{r} - G_{\Phi_\varepsilon}(r), \tag{2.13}$$

$$H_2^{\Phi_\varepsilon}(r) = \frac{1}{r} \left(\frac{B'_{\Phi_\varepsilon}(r)}{r} \right)'. \tag{2.14}$$

are the regularized versions of the functions H_1 and H_2 given in Eqs. (2.7)-(2.8). The functions $H_1^{\Phi_\varepsilon}$ and $H_2^{\Phi_\varepsilon}$ approximate their singular counterparts H_1 and H_2 away from the force location while staying bounded throughout the whole domain
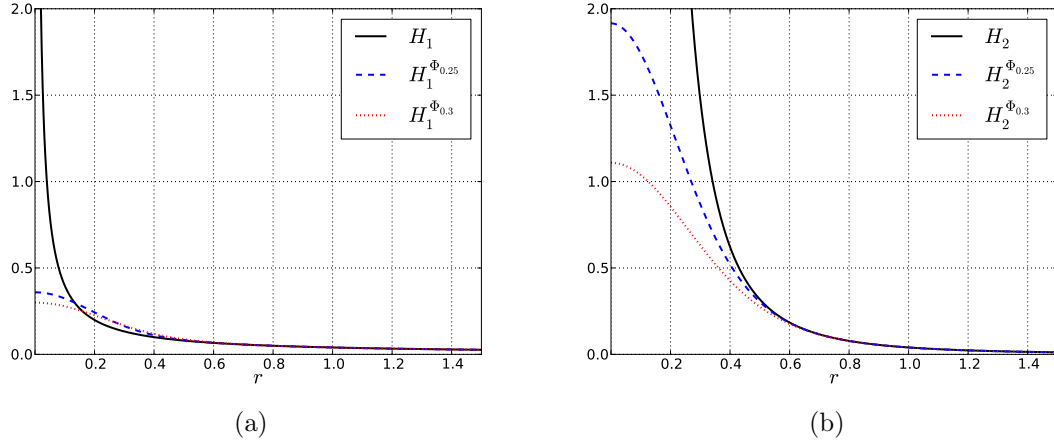
Figure 2.4: The regularized functions $H_1^{\Phi_\varepsilon}$ and $H_2^{\Phi_\varepsilon}$ approximate the singular H_1 and H_2 away from the force location at $r = 0$ but stay smooth throughout the domain. The corresponding blob is defined in Eq. 2.15 *Source:* H1H2.py.

(see Figure 2.4). We note that any attempts to regularize the functions H_1 and H_2 directly are faced with difficulties. For instance, the regularized versions

$$H_1(r) = \frac{1}{8\pi(r + \varepsilon)}, \qquad\qquad H_2(r) = \frac{1}{8\pi(r + \varepsilon)^3},$$

lead to a velocity field that has divergence of order ε^2. The regularized Stokeslet on the other hand is divergence free for any blob function.

2.3.1 The regularized Stokeslet for a particular blob

Throughout this thesis we use the Gaussian blob function

$$\Phi_\varepsilon(r) = \frac{1}{\pi^{\frac{3}{2}}\varepsilon^3} \left(\frac{5}{2} - \frac{r^2}{\varepsilon^2} \right) \exp\left(-\frac{r^2}{\varepsilon^2} \right), \qquad\qquad (2.15)$$

which has been previously used by other authors [HOdPG07, KG12]. Our choice is motivated by two reasons.

(a) Blob Eq. (2.15) has good decay properties, that is the corresponding regularized Stokeslet approximates the singular Stokeslet well away from the force location.

(b) The Fourier transform in x and y of blob Eq. (2.15) is easy to compute analytically, which is important for the computation of doubly-periodic flows.

About (a): Naively one could be tempted to think that the rate at which the regularized Stokeslet converges to the singular Stokeslet for $r \to \infty$ is directly related to the decay rate of the blob. However, this is *not* true. In fact, even for a compactly supported blob that is exactly equal to zero outside of its support, the convergence rate of the regularized Stokeslet can still be comparatively slow. The convergence rate of the regularized Stokeslet is fast if the first two moments of the blob are zero, where the kth *moment* is defined as

$$M_{|k|} = 4\pi \int_0^\infty r^{k+2} \Phi_\varepsilon(r) \, dr.$$

The reasons for this fact are beyond the scope of this thesis, so we limit ourselves to listing the implications the above statement has for blob (2.15). For blob (2.15) the first three moments (i.e. $k = 1, 2, 3$) are equal to 0^3, which means that the regularization error of the numerical approximation is of order $\mathcal{O}(\varepsilon^4)$ [CFM05] and the velocity due to $B - B_{\Phi_\varepsilon}$ decays exponentially [LBCL13].

About (b): For us blob (2.15) has the additional advantage that its Fourier transform in x and y is easy to compute analytically. This will be important when we compute the doubly-periodic regularized velocity field in section 3.1.4.

The corresponding regularized Green's functions can be obtained form writing Laplace equation in spherical coordinates as we did in the singular case[4], which gives

$$G_{\Phi_\varepsilon}(r) = -\frac{1}{4\pi^{\frac{3}{2}}\varepsilon} \exp\left(-\frac{r^2}{\varepsilon^2}\right) - \frac{1}{4\pi r} \operatorname{erf}\left(\frac{r}{\varepsilon}\right), \tag{2.16}$$

$$B_{\Phi_\varepsilon}(r) = -\frac{\frac{1}{2}\varepsilon}{4\pi^{\frac{3}{2}}} \exp\left(-\frac{r^2}{\varepsilon^2}\right) - \frac{r}{8\pi} \operatorname{erf}\left(\frac{r}{\varepsilon}\right). \tag{2.17}$$

---

[3] Trivially all odd moments are equal to zero for any radially symmetric blob.
[4] *see* Mathematica notebook GreensFunctionsRealSpace.nb (also GreensFunctionsRealSpace.pdf)

The regularized Stokeslet is readily obtained from plugging into Eqs. (2.13)-(2.14).

2.3.2   Summary of the regularized Stokeslet

> **The method of regularized Stokeslets**
>
> In Stokes flow the fluid velocity $\mathbf{u}$ at a point $\mathbf{x}$ due to a *regularized* point force with strength $\mathbf{f}_0$ centered at $\mathbf{x}_0$ is given by
>
> $$\mu \mathbf{u}\left(\mathbf{x}\right) = H_1^{\Phi_\varepsilon}(r)\mathbf{f}_0 + H_2^{\Phi_\varepsilon}(r)\left(\mathbf{f}_0 \cdot \tilde{\mathbf{x}}\right)\tilde{\mathbf{x}},$$
>
> where $\tilde{\mathbf{x}} = \mathbf{x} - \mathbf{x}_0$, $r = |\tilde{\mathbf{x}}|$. When the point force is regularized with blob Φ_ε from Eq. (2.15) we have
>
> $$H_1^{\Phi_\varepsilon}(r) = \frac{1}{4\pi^{\frac{3}{2}}\varepsilon}\exp\left(-\frac{r^2}{\varepsilon^2}\right) + \frac{1}{8\pi r}\operatorname{erf}\left(\frac{r}{\varepsilon}\right),$$
>
> $$H_2^{\Phi_\varepsilon}(r) = \frac{-1}{4\pi^{\frac{3}{2}}\varepsilon r^2}\exp\left(-\frac{r^2}{\varepsilon^2}\right) + \frac{1}{8\pi r^3}\operatorname{erf}\left(\frac{r}{\varepsilon}\right).$$
>
> Even though the expressions for $H_1^{\Phi_\varepsilon}$ and $H_2^{\Phi_\varepsilon}$ are regular at $r = 0$, in order to avoid round-off errors when $r \ll \varepsilon$ it is advisable in this case to use the Taylor series expansions
>
> $$H_1^{\Phi_\varepsilon}(r) = \frac{1}{\varepsilon\pi^{\frac{3}{2}}}\left(\frac{1}{2} - \frac{1}{3}\cdot\frac{r^2}{\varepsilon^2} + \frac{3}{20}\frac{r^4}{\varepsilon^4} + \mathcal{O}\left(\frac{r^6}{\varepsilon^6}\right)\right),$$
>
> $$H_2^{\Phi_\varepsilon}(r) = \frac{1}{\varepsilon^3\pi^{\frac{3}{2}}}\left(\frac{1}{6} - \frac{1}{10}\frac{r^2}{\varepsilon^2} + \frac{1}{28}\frac{r^4}{\varepsilon^4} + \mathcal{O}\left(\frac{r^6}{\varepsilon^6}\right)\right).$$

2.4   Stokes flow near a planar wall - The method of images

The method of images was derived by Blake in 1971 [Bla71a].

We now want so solve Stokes Eq. (2.1) for a singular point force in the presence of an infinite planar wall. Without loss of generality we will assume that the wall is

located at $z = 0$. In practice the planar wall can be thought of as an approximation to a cell surface or channel wall. Since cilia always attach to some boundary, modeling wall effects will be crucial for our model of cilia. At the interface between the solid surface and the surrounding fluid we enforce the so-called *no-slip condition* [Bat67, section 3.3], which states that there can't be any discontinuities, or jumps, in the velocity. In other words, the fluid velocity has to decay to zero near the wall, that is $\mathbf{u}|_{z=0} = \mathbf{0}$.

One way to satisfy boundary conditions for a general linear boundary value problem is to start with a solution to the inhomogeneous problem and add to it the right homogeneous solution so that the superposition of inhomogeneous and homogeneous solution satisfies the boundary condition. In our case, the fluid velocity can be written as the superposition a Stokeslet centered at $\mathbf{x}_0 = (x_0, y_0, z_0)$ and some image elements, namely a Stokeslet, a *doublet* and a *dipole*, centered at the image point $\mathbf{x}_0^* = (x_0, y_0, -z_0)$. The doublet and the dipole are obtained form differentiating the Stokeslet and therefore solve Stokes equation as well. Since the singularity of each image elements lies *outside* of the computational domain, the image elements solve the homogeneous Stokes equation with zero force *inside* the computational domain (see also Figure 2.5). Therefore the superposition of the Stokeslet and the images elements is a solution to Stokes equation with a single point force centered at $\mathbf{x}_0$. More precisely, the fluid velocity can be written as [Bla71a]

$$\mu \mathbf{u}(\mathbf{x}) = \mathbf{St}_{\mathbf{f}_0}(\tilde{\mathbf{x}}) - \mathbf{St}_{\mathbf{f}_0}(\tilde{\mathbf{x}}^*) - 2h\mathbf{Do}_{\mathbf{q},\mathbf{e}_3}(\tilde{\mathbf{x}}^*) - h^2\mathbf{Dp}_{\mathbf{q}}(\tilde{\mathbf{x}}^*), \qquad (2.18)$$

where $\tilde{\mathbf{x}} = \mathbf{x} - \mathbf{x}_0$, $\tilde{\mathbf{x}}^* = \mathbf{x} - \mathbf{x}_0^*$, $h = z_0$ and $\mathbf{St}_{\mathbf{f}_0}$ is the Stokeslet defined in Eq. (2.6). Formulas for the doublet $\mathbf{Do}_{\mathbf{q},\mathbf{e}_3}$ and the dipole $\mathbf{Dp}_{\mathbf{q}}$ are derived in the following two subsections.
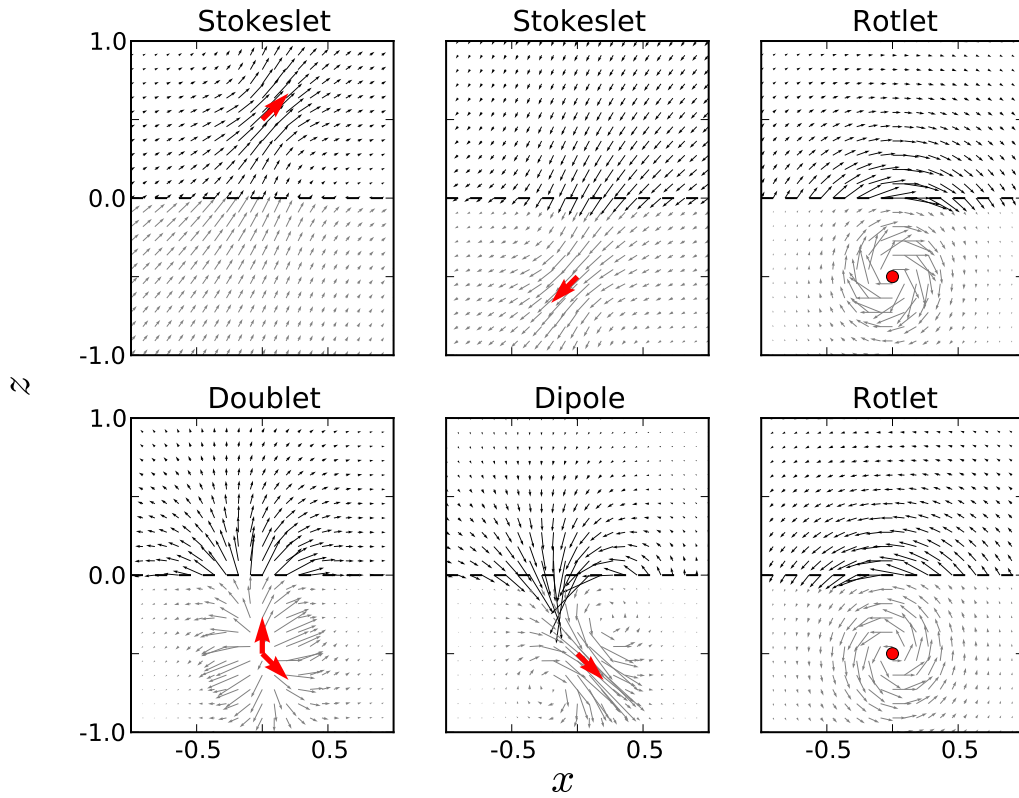
Figure 2.5: Only the Stokeslet (upper left) has a singularity in the domain of interest ($z > 0$). All the other image elements solve the homogeneous Stokes equation with zero force for $z > 0$. In the singular case the two rotlets cancel and the image system consists only of Stokeslet, doublet and dipole. In the regularized case all six elements are needed to cancel the velocity at $z = 0$. We note that the force vector corresponding to the two rotlets is perpendicular to the x, z-plane. *Source:* images.py.

2.4.1 The doublet

The *doublet* is defined as the directional derivative of the Stokeslet defined in Eq. (2.6)

$$\mathbf{Do}_{\mathbf{q},\mathbf{e}_3}\left(\tilde{\mathbf{x}}\right) = \nabla\left(\mathbf{St}_{\mathbf{q}}\left(\tilde{\mathbf{x}}\right)\cdot\mathbf{e}_3\right)$$

$$= \frac{H_1'(r)}{r}\left(\mathbf{q}\cdot\mathbf{e}_3\right)\tilde{\mathbf{x}} + \frac{H_2'(r)}{r}\left(\mathbf{q}\cdot\tilde{\mathbf{x}}\right)\left(\tilde{\mathbf{x}}\cdot\mathbf{e}_3\right)\tilde{\mathbf{x}} + H_2(r)\left(\left(\tilde{\mathbf{x}}\cdot\mathbf{e}_3\right)\mathbf{q} + \left(\mathbf{q}\cdot\tilde{\mathbf{x}}\right)\mathbf{e}_3\right),$$

$$(2.19)$$

where

$$\frac{H_1'(r)}{r} = \frac{-1}{8\pi r^3},$$
$$H_2(r) = \frac{1}{8\pi r^3},$$
$$\frac{H_2'(r)}{r} = \frac{-3}{8\pi r^5},$$

follow directly from Eqs. (2.7)-(2.8). The doublet is also referred to as *Stokeslet doublet*, *point-force doublet* and *point-force dipole* [Poz97, Sections 6.4, 6.5]. The flow field due to a doublet is shown in Figure 2.5.

2.4.2 The dipole

We define the *potential dipole*, or just *dipole*, as the negative Laplacian of the Stokeslet defined in Eq. (2.5)

$$\mathbf{Dp}_{\mathbf{q}}\left(\tilde{\mathbf{x}}\right) = -\Delta\mathbf{St}_{\mathbf{q}}\left(\tilde{\mathbf{x}}\right)$$

$$= -\left(\left(\mathbf{q}\cdot\nabla\right)\nabla - \mathbf{q}\Delta\right)G(r)$$

$$= D_1(r)\mathbf{q} + D_2(r)\left(\mathbf{q}\cdot\tilde{\mathbf{x}}\right)\tilde{\mathbf{x}},$$

$$(2.20)$$

where

$$D_1(r) = -\frac{G'(r)}{r} = \frac{-1}{4\pi r^3},$$
$$D_2(r) = -\frac{1}{r}\left(\frac{G'(r)}{r}\right)' = \frac{3}{4\pi r^5},$$

follow directly from Eqs. (2.7)-(2.8) and the definitions of the Green's functions G and B. The flow field due to a dipole is shown in Figure 2.5. Alternatively the dipole can be derived from a *point source* of strength m [Poz92, Section 7.2]

$$\mathbf{So}_m\left(\tilde{\mathbf{x}}\right) = \frac{m\tilde{\mathbf{x}}}{4\pi r^3},$$

which gives the velocity field defined by the equation

$$0 = -\nabla p + \mu\Delta\mathbf{u},$$

$$m\cdot\delta\left(\mathbf{x} - \mathbf{x}_0\right) = \nabla\cdot\mathbf{u},$$

where again δ is the Dirac delta function. Then the dipole is the directional derivative of a point source with unit strength in direction $\mathbf{q}$. In order to understand the physical intuition behind this definition consider two point sources of opposite strength, that is a point sink and a point source each with strength m, located at two nearby points $\mathbf{x}_0$ and $\mathbf{x}_1$. The dipole then gives the flow field obtained from letting $\mathbf{x}_0 - \mathbf{x}_1 \to 0$ while setting $\mathbf{q} = m\left(\mathbf{x}_0 - \mathbf{x}_1\right)$ [Poz97, Section 2.1].

2.4.3   Summary of the method of images

The method of images

In Stokes flow the fluid velocity $\mathbf{u}$ at a point $\mathbf{x}$

- that is due to a *singular* point force with strength $\mathbf{f}_0$ centered at $\mathbf{x}_0$,

- that satisfies $\mathbf{u}(\mathbf{x})|_{z=0} = \mathbf{0}$ at a planar wall,

is given by

$$\mu\mathbf{u}(\mathbf{x}) = \mathbf{St}_{\mathbf{f}_0}(\tilde{\mathbf{x}}) - \mathbf{St}_{\mathbf{f}_0}(\tilde{\mathbf{x}}^*) - 2h\mathbf{Do}_{\mathbf{q},\mathbf{e}_3}(\tilde{\mathbf{x}}^*) - h^2\mathbf{Dp}_{\mathbf{q}}(\tilde{\mathbf{x}}^*),$$

where

$$\mathbf{St}_{\mathbf{f}_0}(\tilde{\mathbf{x}}) = H_1(r)\mathbf{f}_0 + H_2(r)\left(\mathbf{f}_0 \cdot \tilde{\mathbf{x}}\right)\tilde{\mathbf{x}},$$

$$\mathbf{Do}_{\mathbf{q},\mathbf{e}_3}(\tilde{\mathbf{x}}^*) = \frac{H_1'(r^*)}{r^*}\left(\mathbf{q} \cdot \mathbf{e}_3\right)\tilde{\mathbf{x}}^* + \frac{H_2'(r^*)}{r^*}\left(\mathbf{q} \cdot \tilde{\mathbf{x}}^*\right)\left(\tilde{\mathbf{x}}^* \cdot \mathbf{e}_3\right)\tilde{\mathbf{x}}^*$$
$$+ H_2(r^*)\left(\left(\tilde{\mathbf{x}}^* \cdot \mathbf{e}_3\right)\mathbf{q} + \left(\mathbf{q} \cdot \tilde{\mathbf{x}}^*\right)\mathbf{e}_3\right),$$

$$\mathbf{Dp}_{\mathbf{q}}(\tilde{\mathbf{x}}^*) = D_1(r^*)\mathbf{q} + D_2(r^*)\left(\mathbf{q} \cdot \tilde{\mathbf{x}}^*\right)\tilde{\mathbf{x}}^*,$$

where

$$\mathbf{x}_0 = (x_0, y_0, z_0), \qquad \tilde{\mathbf{x}} = \mathbf{x} - \mathbf{x_0}, \qquad r = |\tilde{\mathbf{x}}|,$$
$$\mathbf{x}_0^* = (x_0, y_0, -z_0), \qquad \tilde{\mathbf{x}}^* = \mathbf{x} - \mathbf{x_0^*}, \qquad r^* = |\tilde{\mathbf{x}}^*|,$$
$$h = z_0, \qquad \mathbf{e}_3 = (0, 0, 1), \qquad \mathbf{f} = (f_1, f_2, f_3),$$
$$\mathbf{q} = (-f_1, -f_2, f_3),$$

and

$*(r)$	n	b_0
$H_1(r)$	0	1
$H_1(r)/r$	2	-1
$H_2(r)$	2	1
$H_1(r)/r$	4	-3
$D_1(r)$	2	-2
$D_2(r)$	4	6

$$*(r) = \frac{b_0}{8\pi r^{n+1}}.$$

2.5 The method of images for regularized Stokeslets

The method of images for regularized Stokeslets was first derived by Ainley et. al. in 2008 for one particular blob [ADE$^+$08] and the general method was described by Cortez and Varela in 2015 [CV15].

Now we turn our attention to a regularized point force $\mathbf{f}_0$ centered at $\mathbf{x}_0$ that acts near a wall $z = 0$ where the fluid velocity satisfies the no-slip condition $\mathbf{u}|_{z=0} = \mathbf{0}$. The fluid velocity is given by the method of images for regularized Stokeslets [CV15]

$$
\mu \mathbf{u}\left(\mathbf{x}\right) = \mathbf{St}_{\mathbf{f}_0}^{\Phi_\varepsilon^s}\left(\tilde{\mathbf{x}}\right) - \mathbf{St}_{\mathbf{f}_0}^{\Phi_\varepsilon^s}\left(\tilde{\mathbf{x}}^*\right) - 2h\mathbf{Do}_{\mathbf{q},\mathbf{e}_3}^{\Phi_\varepsilon^s}\left(\tilde{\mathbf{x}}^*\right) - h^2\mathbf{Dp}_{\mathbf{q}}^{\Phi_\varepsilon^d}\left(\tilde{\mathbf{x}}^*\right)
$$
$$
+ 2h\left(\mathbf{Ro}_{\mathbf{L}}^{\Phi_\varepsilon^s}\left(\tilde{\mathbf{x}}^*\right) - \mathbf{Ro}_{\mathbf{L}}^{\Phi_\varepsilon^d}\left(\tilde{\mathbf{x}}^*\right)\right), \tag{2.21}
$$

where $\mathbf{x}_0 = (x_0, y_0, z_0)$, $\mathbf{x}_0^* = (x_0, y_0, -z_0)$, $\tilde{\mathbf{x}}^* = \mathbf{x} - \mathbf{x}_0^*$ and $h = z_0$. The regularized image system is the natural regularization of the singular image system defined in Eq. (2.18) where the underlying singular Green's functions G and B are replaced by their regularized counterparts. We have to make the following two adaptations.

(a) In addition to the regularized version of the three image elements from the singular case (a Stokeslet, a doublet and a dipole), the regularized image system additionally consists of two regularized rotlets $\mathbf{Ro}_{\mathbf{L}}^{\Phi_\varepsilon^s}$ and $\mathbf{Ro}_{\mathbf{L}}^{\Phi_\varepsilon^d}$. Both regularized rotlets combined are of order ε^2, where ε is the regularization parameter, which explains their absence in the singular case $\varepsilon = 0$.

(b) In order to cancel the fluid velocity at $z = 0$, two different blobs Φ_ε^s and Φ_ε^d are needed. For a given blob Φ_ε^s the *companion blob* Φ_ε^d is computed from [CV15]

$$
\Phi_\varepsilon^d\left(r\right) = \frac{2}{r^5}\int_0^r t^4\Phi_\varepsilon^s\left(t\right)dt.
$$

The superscript s and d are reminders that we use the first blob to regularize the Stokeslet and the companion blob to regularize the dipole. Since both blobs converge to the Dirac delta distribution as $\varepsilon \to 0$, there is no need for this distinction in the singular case.

The regularized image elements are derived in the following subsections.

2.5.1 The regularized doublet

The *regularized doublet* is defined as the directional derivative of the regularized Stokeslet from Eq. (2.12)

$$
\begin{aligned}
&\mathbf{Do}_{\mathbf{q},\mathbf{e}_3}^{\Phi_\varepsilon}(\tilde{\mathbf{x}}) \\
&= \nabla \left(\mathbf{St}_{\mathbf{q}}^{\Phi_\varepsilon}(\tilde{\mathbf{x}}) \cdot \mathbf{e}_3 \right) \hspace{5cm} (2.22) \\
&= \frac{\left(H_1^{\Phi_\varepsilon}(r) \right)'}{r} \left(\mathbf{q} \cdot \mathbf{e}_3 \right) \tilde{\mathbf{x}} + \frac{\left(H_2^{\Phi_\varepsilon}(r) \right)'}{r} \left(\mathbf{q} \cdot \tilde{\mathbf{x}} \right) \left(\tilde{\mathbf{x}} \cdot \mathbf{e}_3 \right) \tilde{\mathbf{x}} + H_2^{\Phi_\varepsilon}(r) \left(\left(\tilde{\mathbf{x}} \cdot \mathbf{e}_3 \right) \mathbf{q} + \left(\mathbf{q} \cdot \tilde{\mathbf{x}} \right) \mathbf{e}_3 \right),
\end{aligned}
$$

where $H_1^{\Phi_\varepsilon}$ and $H_2^{\Phi_\varepsilon}$ are defined as in Eqs. (2.13)-(2.14). Note that this definition is the natural analog to the derivation of the singular doublet in section 2.4.1.

2.5.2 The regularized dipole

We define the *regularized dipole* as the negative Laplacian of the regularized Stokeslet Eq. (2.11)

$$
\begin{aligned}
\mathbf{Dp}_{\mathbf{q}}^{\Phi_\varepsilon}(\tilde{\mathbf{x}}) &= -\Delta \mathbf{St}_{\mathbf{q}}^{\Phi_\varepsilon}(\tilde{\mathbf{x}}) \\
&= - \left((\mathbf{f}_0 \cdot \nabla) \nabla - \mathbf{f}_0 \Delta \right) G_{\Phi_\varepsilon}(r) \\
&= D_1^{\Phi_\varepsilon}(r)\mathbf{q} + D_2^{\Phi_\varepsilon}(r) \left(\mathbf{q} \cdot \tilde{\mathbf{x}} \right) \tilde{\mathbf{x}}, \hspace{2cm} (2.23)
\end{aligned}
$$

where

$$D_1^{\Phi_\varepsilon}(r) = -\left(\frac{G'_{\Phi_\varepsilon}(r)}{r} - \Phi^\varepsilon(r)\right)$$

$$D_2^{\Phi_\varepsilon}(r) = -\frac{1}{r}\left(\frac{G'_{\Phi_\varepsilon}(r)}{r}\right)',$$

follow directly from Eqs. (2.13)-(2.14) and the definitions of the regularized Green's functions G_{Φ_ε} and B_{Φ_ε} in Eqs. (2.9)-(2.10). Note that this definition is the natural analog to the derivation of the singular dipole in section 2.4.2.

2.5.3 The regularized rotlet

The singular *rotlet* or *couplet* is defined as

$$\begin{aligned}
\mathbf{Ro_L}(\tilde{\mathbf{x}}) &= \mathbf{L} \times \nabla G(r) \\
&= \frac{G'(r)}{r}(\mathbf{L} \times \tilde{\mathbf{x}}) \\
&= \frac{-1}{4\pi r^3}(\mathbf{L} \times \tilde{\mathbf{x}}).
\end{aligned}$$

The velocity field describes a rotation about the vector $\mathbf{L}$ (see also Figure 2.5). Alternatively the rotlet can be derived from the antisymmetric part of the doublet Eq. (2.19) [Poz97, Section 6.5]. The *regularized rotlet* is given by

$$\mathbf{Ro_L^{\Phi_\varepsilon}} = \mathbf{L} \times \nabla G_{\Phi_\varepsilon}(r) = \frac{G'_{\Phi_\varepsilon}(r)}{r}(\mathbf{L} \times \tilde{\mathbf{x}}), \tag{2.24}$$

where G_{Φ_ε} is defined by Eq. (2.9).

2.5.4 The image system for a particular blob

For the Stokeslet we use the Gaussian blob function from Eq. (2.15)

$$\Phi_\varepsilon^s(r) = \frac{1}{\pi^{\frac{3}{2}}\varepsilon^3}\left(\frac{5}{2} - \frac{r^2}{\varepsilon^2}\right)\exp\left(-\frac{r^2}{\varepsilon^2}\right),$$

whose associated Green's functions $G_{\Phi_\varepsilon^s}$ and $B_{\Phi_\varepsilon^s}$ are defined in Eqs. (2.16)-(2.17). The corresponding companion blob and its associated Green function can be computed from formulas given in [CV15][5]:

$$\Phi_\varepsilon^d(r) = \frac{2}{r^5}\int_0^r t^4\Phi_\varepsilon^s(t)\,dt = \frac{1}{\pi^{\frac{3}{2}}\varepsilon^3}\exp\left(-\frac{r^2}{\varepsilon^2}\right), \qquad (2.25)$$

$$G_{\Phi_\varepsilon^d}(r) = \frac{2}{r^3}\int_0^r t^2 G_{\Phi_\varepsilon^s}(t)\,dt = -\frac{1}{4\pi r}\operatorname{erf}\left(\frac{r}{\varepsilon}\right).$$

The function $B_{\Phi_\varepsilon^d}$ is not needed since the companion blob is used only to compute the corresponding regularized dipole and regularized rotlet which only depend on the function $G_{\Phi_\varepsilon^d}$. Therefore, the fact that as a positive function Φ_ε^d has nonzero second moment, which implies slow convergence of $B_{\Phi_\varepsilon^d}$ to B as $\varepsilon \to 0$, is of no concern to us. The convergence $G_{\Phi_\varepsilon^d} \to G$ is Gaussian since the total integral of the companion blob is one.

2.5.5 Summary of the method of images for regularized Stokeslets

The method of images for regularized Stokeslets

In Stokes flow the fluid velocity $\mathbf{u}$ at a point $\mathbf{x}$

- that is due to a *regularized* point force with strength $\mathbf{f}_0$ centered at $\mathbf{x}_0$,

---

[5] *see* Mathematica notebook GreensFunctionsRealSpace.nb (also GreensFunctionsRealSpace.pdf)

The method of images for regularized Stokeslets (Continued)

- that satisfies $\mathbf{u}(\mathbf{x})|_{z=0} = \mathbf{0}$ at a planar wall,

is given by

$$\mu\mathbf{u}\left(\mathbf{x}\right) = \mathbf{St}_{\mathbf{f}_0}^{\Phi_\varepsilon^s}\left(\tilde{\mathbf{x}}\right) - \mathbf{St}_{\mathbf{f}_0}^{\Phi_\varepsilon^s}\left(\tilde{\mathbf{x}}^*\right) - 2h\mathbf{Do}_{\mathbf{q},\mathbf{e}_3}^{\Phi_\varepsilon^s}\left(\tilde{\mathbf{x}}^*\right) - h^2\mathbf{Dp}_{\mathbf{q}}^{\Phi_\varepsilon^d}\left(\tilde{\mathbf{x}}^*\right)$$
$$+ 2h\left(\mathbf{Ro}_{\mathbf{L}}^{\Phi_\varepsilon^s}\left(\tilde{\mathbf{x}}^*\right) - \mathbf{Ro}_{\mathbf{L}}^{\Phi_\varepsilon^d}\left(\tilde{\mathbf{x}}^*\right)\right),$$

where

$$\mathbf{St}_{\mathbf{f}_0}^{\Phi_\varepsilon}\left(\tilde{\mathbf{x}}\right) = H_1^{\Phi_\varepsilon}(r)\mathbf{f}_0 + H_2^{\Phi_\varepsilon}(r)\left(\mathbf{f}_0 \cdot \tilde{\mathbf{x}}\right)\tilde{\mathbf{x}},$$

$$\mathbf{Do}_{\mathbf{q},\mathbf{e}_3}^{\Phi_\varepsilon}\left(\tilde{\mathbf{x}}^*\right) = \frac{H_1^{\Phi_\varepsilon'}(r^*)}{r^*}\left(\mathbf{q} \cdot \mathbf{e}_3\right)\tilde{\mathbf{x}}^* + \frac{H_2^{\Phi_\varepsilon'}(r^*)}{r^*}\left(\mathbf{q} \cdot \tilde{\mathbf{x}}^*\right)\left(\tilde{\mathbf{x}}^* \cdot \mathbf{e}_3\right)\tilde{\mathbf{x}}^*$$
$$+ H_2^{\Phi_\varepsilon}(r^*)\left(\left(\tilde{\mathbf{x}}^* \cdot \mathbf{e}_3\right)\mathbf{q} + \left(\mathbf{q} \cdot \tilde{\mathbf{x}}^*\right)\mathbf{e}_3\right),$$

$$\mathbf{Dp}_{\mathbf{q}}^{\Phi_\varepsilon}\left(\tilde{\mathbf{x}}^*\right) = D_1^{\Phi_\varepsilon}(r^*)\mathbf{q} + D_2^{\Phi_\varepsilon}(r^*)\left(\mathbf{q} \cdot \tilde{\mathbf{x}}^*\right)\tilde{\mathbf{x}}^*,$$

$$\mathbf{Ro}_{\mathbf{L}}^{\Phi_\varepsilon} = \frac{G'_{\Phi_\varepsilon}(r^*)}{r^*}\left(\mathbf{L} \times \tilde{\mathbf{x}}^*\right),$$

and

$$\mathbf{x}_0 = (x_0, y_0, z_0), \qquad \tilde{\mathbf{x}} = \mathbf{x} - \mathbf{x}_0, \qquad r = |\tilde{\mathbf{x}}|,$$
$$\mathbf{x}_0^* = (x_0, y_0, -z_0), \qquad \tilde{\mathbf{x}}^* = \mathbf{x} - \mathbf{x}_0^*, \qquad r^* = |\tilde{\mathbf{x}}^*|,$$
$$h = z_0, \qquad \mathbf{e}_3 = (0, 0, 1), \qquad \mathbf{f} = (f_1, f_2, f_3),$$
$$\mathbf{q} = (-f_1, -f_2, f_3), \qquad \mathbf{L} = (f_2, -f_1, 0).$$

When the point force is regularized with blob Φ_ε^s from Eq. (2.15), which gives rise to the companion blob Φ_ε^d from Eq. (2.25), we have

	n	regular expression			Taylor series		
		a_0	a_2	b_0	c_0	c_2	c_4
$H_1^{\Phi_\varepsilon^s}(r)$	0	1	0	1	$\frac{1}{2}$	$-\frac{1}{3}$	$\frac{3}{20}$
$H_1^{\Phi_\varepsilon^s'}(r)/r$	2	1	-2	-1	$-\frac{2}{3}$	$\frac{3}{5}$	$-\frac{2}{7}$
$H_2^{\Phi_\varepsilon^s}(r)$	2	-1	0	1	$\frac{1}{6}$	$-\frac{1}{10}$	$\frac{1}{28}$
$H_2^{\Phi_\varepsilon^s'}(r)/r$	4	3	2	-3	$-\frac{1}{5}$	$\frac{1}{7}$	$-\frac{1}{18}$
$D_1^{\Phi_\varepsilon^d}(r)$	2	2	4	-2	$\frac{2}{3}$	$-\frac{4}{5}$	$\frac{3}{7}$
$D_2^{\Phi_\varepsilon^d}(r)$	4	-6	-4	6	$\frac{2}{5}$	$-\frac{2}{7}$	$\frac{1}{9}$
$G'_{\Phi_\varepsilon^s}(r)/r$	2	-2	2	2	$\frac{5}{6}$	$-\frac{7}{10}$	$\frac{9}{28}$
$G'_{\Phi_\varepsilon^d}(r)/r$	2	-2	0	2	$\frac{1}{3}$	$-\frac{1}{5}$	$\frac{1}{14}$

The method of images for regularized Stokeslets (Continued)

$$\text{regular expression} = \frac{1}{4\pi^{\frac{3}{2}}\varepsilon r^n}\left(a_0 + a_2\frac{r^2}{\varepsilon^2}\right)\exp\left(-\frac{r^2}{\varepsilon^2}\right) + \frac{b_0}{8\pi r^{n+1}}\,\text{erf}\left(\frac{r}{\varepsilon}\right),$$

$$\text{Taylor series} = \frac{1}{\varepsilon^{n+1}\pi^{\frac{3}{2}}}\left(c_0 + c_2\frac{r^2}{\varepsilon^2} + c_4\frac{r^4}{\varepsilon^4} + \mathcal{O}\left(\frac{r^6}{\varepsilon^6}\right)\right).$$

Even though all expressions are regular at $r = 0$, in order to avoid round-off errors when $r \ll \varepsilon$ it is advisable in this case to use the Taylor series expansions.

Chapter 3

Doubly-periodic Stokes flow in 3D using FFTs

3.1 Doubly-periodic flow in free space

The method presented in this section is published in [CH14].

3.1.1 An overview

In the previous chapter we considered a single point force $\mathbf{f}_0$ in free space, that is in an infinite pool of fluid. The fluid velocity in this case was given by the so-called free space Stokeslet, which we derived as follows.

FS1. (*analytical*) Find the fundamental solution, called Green's function, B of the biharmonic equation.

FS2. (*analytical*) Take the appropriate derivatives of B to find the Stokeslet.

We emphasize that steps **FS1** and **FS2** are used when *deriving* the Stokeslet. Once an analytic expression of the Stokeslet is found, we simply *evaluate* the Stokeslet

wherever we wish to compute the fluid velocity.

We now consider a doubly infinite array of identical copies of the force $\mathbf{f}_0$ distributed periodically in x and y with periods L_x and L_y. A naive approach to obtain the fluid velocity, which however will turn out impractical, is to sum up the free space Stokeslets corresponding to each of the force copies. The resulting infinite double sum is investigated in Theorem 3.1.3, where it is shown that the double sum diverges in general. Conditional convergence is guaranteed if and only if we enforce a so-called *zero net force* condition

$$\sum_{k=1}^{K} \mathbf{f}_k = 0,$$

where we now consider multiple forces $\mathbf{f}_k$, where $k = 1, ..., K$, that are also distributed periodically in x and y with periods L_x and L_y. Nevertheless, as is also shown in Theorem 3.1.3 the convergence is too slow for feasible numerical evaluation.

In our method we take a different approach. Consider a single force $\mathbf{f}_0$ inside the infinite square cylinder $\Omega = [0, L_x] \times [0, L_y] \times \mathbb{R}$. We compute the fluid velocity only inside Ω but we impose periodic boundary conditions in x and y. Deriving the doubly-periodic Stokeslet is analogous to deriving the free space Stokeslet. We perform steps **FS1** and **FS2** in Fourier space with respect to the variables x and y, which gives the Fourier space Stokeslet. Translating the Fourier space Stokeslet back into real space gives the doubly-periodic Stokeslet.

DP1. (*analytical*) Find the fundamental solution, called Green's function, $\hat{B}$ of the biharmonic equation in Fourier space.

DP2. (*analytical*) Take the appropriate derivatives of $\hat{B}$ to find the Fourier space Stokeslet.

DP3. (*numerical*) Find the doubly-periodic Stokeslet by evaluating the Fourier space

Stokeslet on a grid and compute an inverse fast Fourier transform (FFT)[1]

Similar to the free space case we can do steps **DP1** and **DP2** analytically, which means that these steps are only needed when deriving an exact analytic expression of the Fourier space Stokeslet. Unfortunately we are not able to compute the inverse Fourier transform of the Fourier space Stokeslet analytically, which would give us an exact expression for the doubly-periodic Stokeslet. Instead we evaluate the Fourier space Stokeslet on a grid and take an inverse FFT. Computing the inverse FFT incurs the only extra computational costs in addition to just evaluating the Stokeslet. For more details see also Table 3.1.

3.1.2   Fourier transform and FFT - Some definitions

We define the Fourier transform and inverse fast Fourier transform (FFT).

Definition 3.1.1. For an integrable function $g(\mathbf{x})$ we define the two-dimensional *Fourier transform* in x and y as

$$\hat{g}(k, m; z) = \int_{-\infty}^{\infty} \int_{-\infty}^{\infty} g(x, y, z) \exp\left(-2\pi i \left(\frac{kx}{L_x} + \frac{my}{L_y}\right)\right) dx dy.$$

When this equation is used to compute the Fourier transform of a function on an $N_x \times N_y$ grid of wave numbers, the values of g on a grid are found using the *inverse FFT*

$$g(p\Delta x, q\Delta y, z) = \frac{1}{L_x L_y} \sum_{k=0}^{N_x-1} \sum_{m=0}^{N_y-1} \hat{g}(k, m, z) \exp\left(2\pi i \cdot \left(\frac{kp}{N_x} + \frac{mq}{N_y}\right)\right), \qquad (3.1)$$

for $p = 0, 1, \ldots, N_x - 1$, $q = 0, 1, \ldots, N_y - 1$, $\Delta x = L_x/N_x$ and $\Delta y = L_y/N_y$.

---

[1] Like many other authors we use the terms discrete Fourier transform (DFT) and fast Fourier transform (FFT) interchangeably.

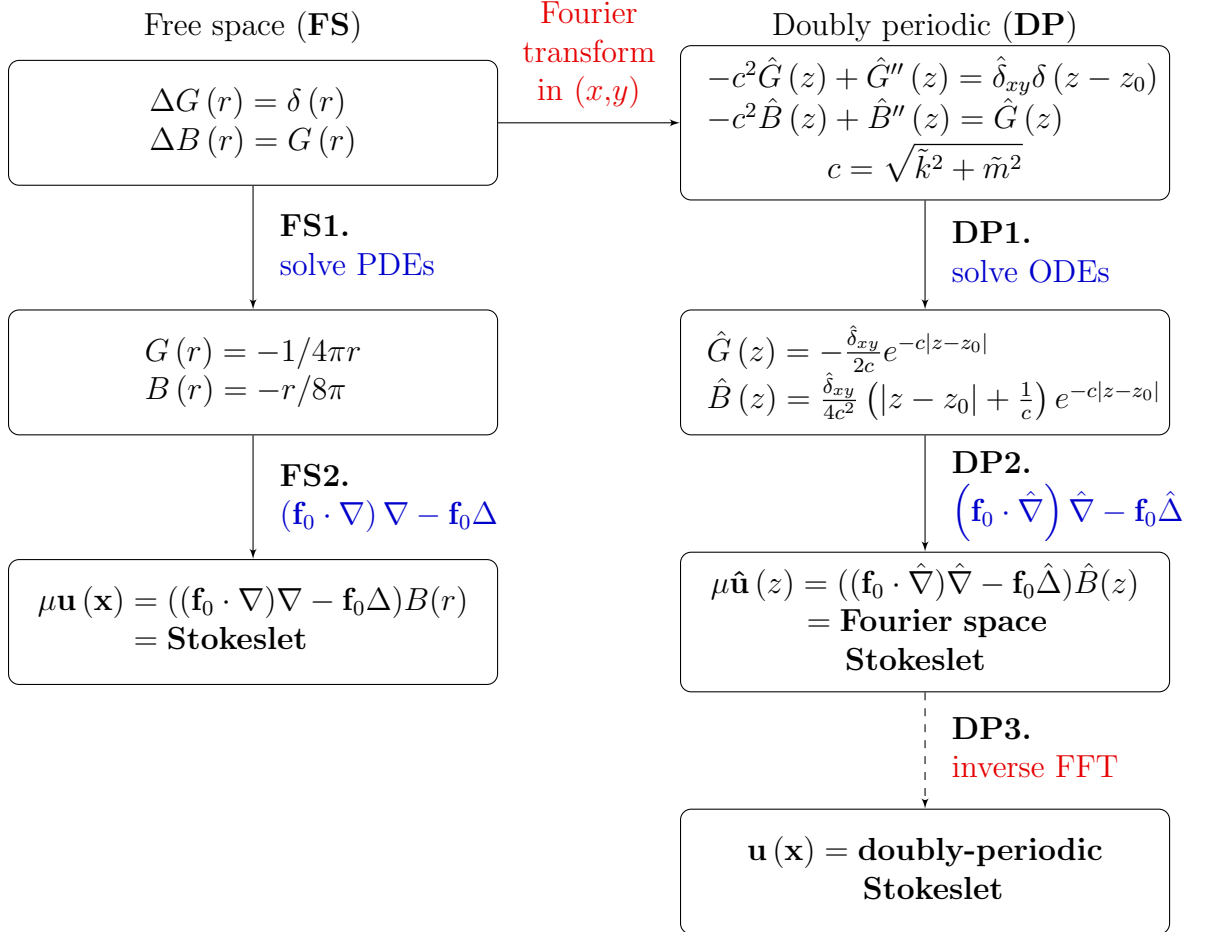Table 3.1: Schematic for how to find the fluid velocity due to a singular point force $\mathbf{f}_0$ centered at $\mathbf{x}_0 = (x_0, y_0, z_0)$, where δ is the Dirac delta function and $r = |\mathbf{x} - \mathbf{x}_0|$. The terminology referring to the Fourier space expressions is defined in Definitions 3.1.1 and 3.1.2. A solid line represents analytical computation and a dashed line represents numerical computation.

Definition 3.1.2. We define the *Fourier space gradient*

$$\hat{\nabla} := \left(i\tilde{k}, i\tilde{m}, \frac{\partial}{\partial z} \right)^T, \tag{3.2}$$

and the *Fourier space Laplacian*

$$\hat{\Delta} := \left(-\tilde{k}^2 - \tilde{m}^2 + \frac{\partial^2}{\partial z^2} \right), \tag{3.3}$$

where $\tilde{k} = 2\pi k/L_x$ and $\tilde{m} = 2\pi m/L_y$,

3.1.3   The doubly-periodic regularized Stokeslet

Consider a single regularized[2] point force $\mathbf{f}_0$ centered at $\mathbf{x}_0 = (x_0, y_0, z_0)$ inside the infinite square cylinder $\Omega = [0, L_x] \times [0, L_y] \times \mathbb{R}$ with periodic boundary conditions in x and y. Using the Fourier space Laplacian (3.3) in the regularized Laplace Eqs. (2.9)-(2.10) yields the system of ordinary differential equations

$$\hat{G}''_{\Phi_\varepsilon}(\tilde{z}) - c^2 \hat{G}_{\Phi_\varepsilon}(\tilde{z}) = \hat{\Phi}_\varepsilon(\tilde{z}), \tag{3.4}$$

$$\hat{B}''_{\Phi_\varepsilon}(\tilde{z}) - c^2 \hat{B}_{\Phi_\varepsilon}(\tilde{z}) = \hat{G}_{\Phi_\varepsilon}(\tilde{z}), \tag{3.5}$$

where $\tilde{z} = z - z_0$, $c = \sqrt{\tilde{k}^2 + \tilde{m}^2}$, and where the integers k and m range from 0 to a maximum positive integer. We have omitted the dependence of the functions on $(\tilde{k}, \tilde{m})$ for notational simplicity and the indicated derivatives are with respect to $\tilde{z}$. The goal is to solve the regularized Fourier space Laplace Eqs. (3.4)-(3.5) exactly for the regularized Fourier space Green's function $\hat{B}_{\Phi_\varepsilon}(\tilde{z})$. In practice this is done using a computer algebra system. The regularized Fourier space Stokeslet can then be determined from the Fourier space analog of the regularized real space

---

[2] We only consider the regularized case since our method relies on computing an inverse FFT, which becomes inaccurate when there are singularities in the solution.

Stokeslet (2.11), which is

$$\hat{\mathbf{St}}_{\mathbf{f_0}}^{\Phi_\varepsilon}(k,m;\tilde{z}) = \left(\left(\mathbf{f_0} \cdot \hat{\nabla}\right)\hat{\nabla} - \mathbf{f_0}\hat{\Delta}\right)\hat{B}_{\Phi_\varepsilon}$$

$$= \begin{pmatrix} (-f_1\tilde{k}^2 - f_2\tilde{k}\tilde{m})\hat{B}_{\Phi_\varepsilon} + if_3\tilde{k}\hat{B}'_{\Phi_\varepsilon} - f_1\hat{G}_{\Phi_\varepsilon} \\ (-f_1\tilde{k}\tilde{m} - f_2\tilde{m}^2)\hat{B}_{\Phi_\varepsilon} + if_3\tilde{m}\hat{B}'_{\Phi_\varepsilon} - f_2\hat{G}_{\Phi_\varepsilon} \\ f_3\left(\tilde{k}^2 + \tilde{m}^2\right)\hat{B}_{\Phi_\varepsilon} + i(f_1\tilde{k} + f_2\tilde{m})\hat{B}'_{\Phi_\varepsilon} \end{pmatrix}, \qquad (3.6)$$

where $\mathbf{f_0} = (f_1, f_2, f_3)$. Up to here, all computations can be done analytically. In particular, the divergence of the regularized Fourier space Stokeslet (3.6) is zero exactly. To complete the evaluation of the velocity field, we fix $\tilde{z}$, evaluate $\hat{\mathbf{St}}_{\mathbf{f_0}}^{\Phi_\varepsilon}(k,m;\tilde{z})$ on a grid of wave numbers, and take the inverse FFT (see Figure 3.1). This yields a doubly-periodic velocity field on a two-dimensional grid for the given fixed value of $\tilde{z}$. We emphasize that since all analytic expressions have been found in Fourier space, there is no need to interpolate the forces onto a grid. The only interpolation required is to evaluate the fluid velocity at any point that might not fall onto the grid. Since the velocity is smooth, no special interpolation procedure is needed.

3.1.4 The doubly-periodic regularized Stokeslet for a particular blob

We show how to find the regularized Fourier space Green's function that solve the Fourier space Laplace Eqs. (3.4)-(3.5) for the Gaussian blob Φ_ε defined in Eq. (2.15). The Fourier transform in (x, y) of the blob is given by

$$\hat{\Phi}_\varepsilon(\tilde{z}) = \hat{\delta}_{x_0 y_0}^\varepsilon \left[\frac{1}{4\sqrt{\pi}}\left(\frac{6}{\varepsilon} + \varepsilon c^2\right) - \frac{\tilde{z}^2}{\sqrt{\pi}\varepsilon^3}\right]\exp\left(-\frac{\tilde{z}^2}{\varepsilon^2}\right), \qquad (3.7)$$

where the factor $\hat{\delta}_{x_0 y_0}^\varepsilon = \exp(-\frac{1}{4}\varepsilon^2 c^2)\exp(-\frac{2\pi i}{L}(kx_0 + my_0))$ contains the dependence on x_0 and y_0. Note that the computation of the Fourier transform is facilitated by

the fact that the blob allows us to separate the x and y variables from the z variable. This property is one of the two reasons we choose this particular Gaussian blob, the other reason being its good decay properties (see Section 2.3.1). Although the wave number pair (k, m) is a parameter in the differential equations, the solutions are all of the same type except when $(k, m) = (0, 0)$, or equivalently $c = 0$. We will treat the latter case separately. Our computations are supported by a computer algebra system[3].

For the case $c \neq 0$, we find the Green's functions

$$\hat{G}_{\Phi_\varepsilon}(\tilde{z}) = -\frac{\hat{\delta}^\varepsilon_{x_0 y_0}}{4c} \exp\left(\frac{\varepsilon^2 c^2}{4}\right) \left[\exp\left(-c\tilde{z}\right) \operatorname{erfc}\left(\frac{c\varepsilon}{2} - \frac{\tilde{z}}{\varepsilon}\right)\right.$$
$$\left. + \exp\left(c\tilde{z}\right) \operatorname{erfc}\left(\frac{c\varepsilon}{2} + \frac{\tilde{z}}{\varepsilon}\right)\right] - \frac{\hat{\delta}^\varepsilon_{x_0 y_0}\varepsilon}{4\sqrt{\pi}} \exp\left(-\frac{\tilde{z}^2}{\varepsilon^2}\right), \tag{3.8}$$

$$\hat{B}_{\Phi_\varepsilon}(\tilde{z}) = \frac{\hat{\delta}^\varepsilon_{x_0 y_0}}{8c^3} \exp\left(\frac{c^2\varepsilon^2}{4}\right) \left[(1 + c\tilde{z}) \exp\left(-c\tilde{z}\right) \operatorname{erfc}\left(\frac{c\varepsilon}{2} - \frac{\tilde{z}}{\varepsilon}\right)\right.$$
$$\left. + (1 - c\tilde{z}) \exp\left(c\tilde{z}\right) \operatorname{erfc}\left(\frac{c\varepsilon}{2} + \frac{\tilde{z}}{\varepsilon}\right)\right] + \frac{\hat{\delta}^\varepsilon_{x_0 y_0}\varepsilon}{4\sqrt{\pi}c^2} \exp\left(-\frac{\tilde{z}^2}{\varepsilon^2}\right), \tag{3.9}$$

$$\hat{B}'_{\Phi_\varepsilon}(\tilde{z}) = -\frac{\hat{\delta}^\varepsilon_{x_0 y_0}}{8c} \exp\left(\frac{c^2\varepsilon^2}{4}\right) \left[\tilde{z} \exp\left(-c\tilde{z}\right) \operatorname{erfc}\left(\frac{c\varepsilon}{2} - \frac{\tilde{z}}{\varepsilon}\right)\right.$$
$$\left. + \tilde{z} \exp\left(c\tilde{z}\right) \operatorname{erfc}\left(\frac{c\varepsilon}{2} + \frac{\tilde{z}}{\varepsilon}\right)\right]. \tag{3.10}$$

The constants of integrations are chosen so that $\hat{G}_{\Phi_\varepsilon}$ and $\hat{B}_{\Phi_\varepsilon}$ approach 0 as $|z| \to \infty$. Otherwise at least one of the functions $\hat{G}_{\Phi_\varepsilon}$ or $\hat{B}_{\Phi_\varepsilon}$ would grow exponentially in z and this growth would also translate into the velocity. It is straightforward to verify that sending $\varepsilon \to 0$ produces the singular Fourier space Green's functions

$$\hat{G}(\tilde{z}) = -\frac{\hat{\delta}_{x_0 y_0}}{2c} \exp\left(-c\,|\tilde{z}|\right), \tag{3.11}$$

$$\hat{B}(\tilde{z}) = \frac{\hat{\delta}_{x_0 y_0}}{4c^2} \left(|\tilde{z}| + \frac{1}{c}\right) \exp\left(-c\,|\tilde{z}|\right), \tag{3.12}$$

[3] *see* Mathematica notebook GreensFunctionsFourierSpace.nb (also GreensFunctionsFourierSpace.pdf)

which solve the singular versions of the Fourier space Laplace Eqs. (3.4)-(3.5) (see Appendix A.3 for a direct derivation of Eqs. (3.11)-(3.12)).

For the case $c = 0$, the Fourier space Stokeslet (3.6) simplifies to

$$
\hat{\mathbf{St}}_{\mathbf{f}_0}^{\Phi_\varepsilon} (0, 0; \tilde{z}) = \begin{pmatrix} -f_1 \\ -f_2 \\ 0 \end{pmatrix} \hat{G}_{0,\Phi_\varepsilon} (\tilde{z}),
\tag{3.13}
$$

where $\hat{G}_{0,\Phi_\varepsilon}$ is the solution to the Fourier space Laplace Eq. (3.4) with Gaussian blob (3.7) when $c = 0$

$$
\hat{G}''_{0,\Phi_\varepsilon} (\tilde{z}) = \left[\frac{3}{2\sqrt{\pi}\varepsilon} - \frac{z^2}{\sqrt{\pi}\varepsilon^3} \right] \exp\left(-\frac{z^2}{\varepsilon^2} \right).
$$

The solution is given by

$$
\hat{G}_{0,\Phi_\varepsilon} (\tilde{z}) = \frac{1}{4} \left[\frac{\varepsilon}{\sqrt{\pi}} \exp\left(-\frac{\tilde{z}^2}{\varepsilon^2} \right) + 2\tilde{z} \operatorname{erf}\left(\frac{\tilde{z}}{\varepsilon} \right) \right].
\tag{3.14}
$$

Sending $\varepsilon \to 0$ yields

$$
\hat{G}_0 (\tilde{z}) = \frac{|\tilde{z}|}{2},
\tag{3.15}
$$

which solves the singular version of the Fourier space Laplace Eq. (3.4) when $c = 0$. The function $\hat{B}_{0,\Phi_\varepsilon}$ is not needed in this case. We chose the constants of integration so that $\hat{G}_{0,\Phi_\varepsilon}$ is symmetric about z_0. This choice is backed up by numerical experiments that compare the doubly periodic Stokeslet to an approximation of the Stokeslet double sum (see Section 3.1.7). It is important to note that it is impossible to choose the constants of integration in a way that would make the zero wave number term decay at infinity. As a result, the fluid velocity due to a single point force grows linearly as $z \to \infty$.
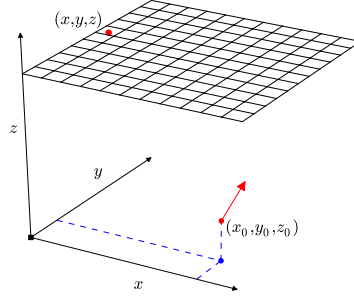
3.1.5 Summary of the method

Figure 3.1: Schematic for the computation of the doubly-periodic velocity field at a point $\mathbf{x} = (x, y, z)$ using FFTs. If the velocity is needed only at $\mathbf{x}$, using periodicity the grid can be shifted to include $\mathbf{x}$ and no interpolation is needed. *Source:* schematic_computation.py.

The doubly-periodic Stokeslet using FFTs

Consider a *regularized* point force with strength $\mathbf{f}_0$ centered at $\mathbf{x}_0$ and distributed periodically in x and y with periods L_x and L_y. The doubly-periodic fluid velocity $\mathbf{u}$ can be found by performing the following algorithm. The algorithm finds $\mathbf{u}$ on an (x, y) grid for fixed z (see also Figure 3.1). The fluid velocity can be interpolated to an arbitrary point $\mathbf{x}$ if needed.

1. For fixed z evaluate $\hat{\mathbf{u}}$ on a grid of wave numbers (k, m).

   - For $(k, m) \neq \mathbf{0}$ the velocity is computed from Eq. (3.6), where the corresponding Green's functions are defined in Eqs. (3.8)-(3.10).

   - For $(k, m) = \mathbf{0}$ the velocity is computed from Eq. (3.13), where the corresponding Green's function is defined in Eq. (3.14).

2. Find $\mathbf{u}$ on the grid by taking an inverse FFT according to Eq. (3.1).

The algorithm gives good results if $\varepsilon \geq 4\Delta x$, where ε is the regularization parameter and Δx is the grid size. If the condition is violated, one needs to use Ewald splitting (Section 4.2.3).

3.1.6 A reference solution using a Stokeslet double sum

We consider a doubly infinite force field of periodic copies of the force $\mathbf{f}_0$ centered at $\mathbf{x}_0 + \mathbf{n}$, where $\mathbf{n} = (nL_x, mL_y, 0)$ for $n, m \in \mathbb{Z}$. The fluid velocity can be represented

as an infinite double sum of the corresponding Stokeslets (2.5), that is

$$
\begin{aligned}
\mu \mathbf{u}\left(\mathbf{x}\right) &= \sum_{n,m=-\infty}^{\infty} \left(\left(\mathbf{f}_0 \cdot \nabla\right) \nabla - \mathbf{f}_0 \Delta\right) B\left(\left|\mathbf{x} - \mathbf{x}_0 - \mathbf{n}\right|\right) \\
&= \frac{1}{8\pi} \sum_{n,m=-\infty}^{\infty} \frac{\mathbf{f}_0}{\left|\mathbf{x} - \mathbf{x}_0 - \mathbf{n}\right|} + \frac{\left[\mathbf{f}_0 \cdot \left(\mathbf{x} - \mathbf{x}_0 - \mathbf{n}\right)\right]\left(\mathbf{x} - \mathbf{x}_0 - \mathbf{n}\right)}{\left|\mathbf{x} - \mathbf{x}_0 - \mathbf{n}\right|^3}.
\end{aligned} \tag{3.16}
$$

Note that the double sum does not converge since the summand is harmonic. In the case of multiple point forces $\mathbf{f}_k$ also distributed periodically, the following theorem gives a necessary and sufficient condition for convergence and also makes a statement about the convergence rate.

Theorem 3.1.3. *Consider the infinite rectangular cylinder $\Omega = [0, L_x] \times [0, L_y] \times \mathbb{R}$. Consider K point forces with strengths $\mathbf{f}_k \in \mathbb{R}^3$ at locations $\mathbf{x}_k \in \Omega$. Then for any evaluation point $\mathbf{x} \in \Omega$ the Stokeslet double-sum*

$$
8\pi\mu\mathbf{u}\left(\mathbf{x}\right) = \sum_{n,m=-\infty}^{\infty} \sum_{k=1}^{K} \frac{\mathbf{f}_k}{\left|\mathbf{x} - \mathbf{x}_k - \mathbf{n}\right|} + \frac{\left[\mathbf{f}_k \cdot \left(\mathbf{x} - \mathbf{x}_k - \mathbf{n}\right)\right]\left(\mathbf{x} - \mathbf{x}_k - \mathbf{n}\right)}{\left|\mathbf{x} - \mathbf{x}_k - \mathbf{n}\right|^3}, \tag{3.17}
$$

where $\mathbf{n} = (nL_x, mL_y, 0)$, converges conditionally if and only if the net force is equal to zero, that is

$$
\sum_{k=1}^{K} \mathbf{f}_k = 0.
$$

In the case of convergence, an asymptotic expansion of the tail of (3.17) is given by

$$
\sum_{\max(|n|,|m|)>N} \sum_{k=1}^{K} \frac{\mathbf{f}_k}{\left|\mathbf{x} - \mathbf{x}_k - \mathbf{n}\right|} + \frac{\left[\mathbf{f}_k \cdot \left(\mathbf{x} - \mathbf{x}_k - \mathbf{n}\right)\right]\left(\mathbf{x} - \mathbf{x}_k - \mathbf{n}\right)}{\left|\mathbf{x} - \mathbf{x}_k - \mathbf{n}\right|^3} = \frac{\mathbf{L}(\mathbf{x})}{N} + \mathcal{O}\left(\frac{1}{N^3}\right),
$$

where $\mathbf{L}$ is a polynomial in $\mathbf{x}$ of degree at most 1.

Remark 3.1.4. When the Stokeslet double sum is approximated by a partial sum

up to N, the computational work is proportional to the total number of forces

$$N_{\text{forces}} = (2N+1)^2 K.$$

Therefore, in this case the decay rate of the error of order $\sqrt{N_{\text{forces}}}$.

We present a proof in Appendix B.1. Fortunately for us in practice the zero net force condition is often satisfied. For instance, a free swimmer fully immersed in a fluid always has zero net force [Tay51]. Also, in the presence of a planar wall with no-slip condition, the Stokeslet combined with its image Stokeslet have zero net force. However, in the simple case of just one force distributed periodically in x and y and no boundary in z, the Stokeslet double-sum (3.16) does *not* converge, even though the FFT method gives us a finite velocity field (see Figure 2.1(c)).

The convergence analysis does not change when the Stokeslet is regularized since the regularized Stokeslet approximates the singular Stokeslet for large $|\mathbf{x} - \mathbf{x}_k|$. We find

$$\mu \mathbf{u}\left(\mathbf{x}\right) = \sum_{n,m=-\infty}^{\infty} \sum_{k=1}^{K} \left(\left(\mathbf{f}_k \cdot \nabla\right) \nabla - \mathbf{f}_k \Delta\right) B_{\Phi_\varepsilon}\left(|\mathbf{x} - \mathbf{x}_k - \mathbf{n}|\right)$$

$$= \sum_{n,m=-N}^{N} \sum_{k=1}^{K} \left(\left(\mathbf{f}_k \cdot \nabla\right) \nabla - \mathbf{f}_k \Delta\right) B_{\Phi_\varepsilon}\left(|\mathbf{x} - \mathbf{x}_k - \mathbf{n}|\right) \tag{3.18a}$$

$$+ \frac{1}{8\pi} \sum_{\max\{|n|,|m|\}>N} \sum_{k=1}^{K} \frac{\mathbf{f}_k}{|\mathbf{x} - \mathbf{x}_k - \mathbf{n}|} + \frac{\left[\mathbf{f}_k \cdot \left(\mathbf{x} - \mathbf{x}_k - \mathbf{n}\right)\right]\left(\mathbf{x} - \mathbf{x}_k - \mathbf{n}\right)}{|\mathbf{x} - \mathbf{x}_k - \mathbf{n}|^3}$$

$$\tag{3.18b}$$

$$+ \sum_{\max\{|n|,|m|\}>N} \sum_{k=1}^{K} \left(\left(\mathbf{f}_k \cdot \nabla\right) \nabla - \mathbf{f}_k \Delta\right)\left(B_{\Phi_\varepsilon} - B\right)\left(|\mathbf{x} - \mathbf{x}_k - \mathbf{n}|\right). \tag{3.18c}$$

Using the Gaussian blob (2.15), the partial sum (3.18a) we can compute exactly using the regularized Stokeslet derived in Section 2.3.2. The error term (3.18b) is investigated in Theorem 3.1.3 and decays of order 0.5 in the total number of forces
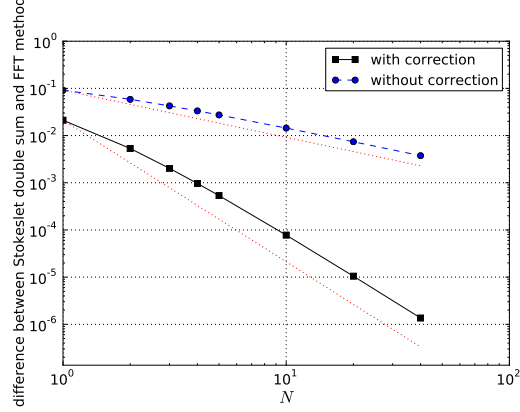
Figure 3.2: Maximum difference between the FFT method and the partial Stokeslet double sum summed from $-N$ to N. Here Correction means that the leading order term of the error is computed exactly and subtracted (*see* Theorem 3.1.3). The two dotted lines correspond to the decay rates $1/N$ and $1/N^3$. Since for the reference solution computational work scales like N^2, in terms of computational complexity the reference solution converges to the FFT solution of order 0.5 without correction and of order 1.5 with correction. The results are shown for 10 random forces with zero net force inside the cube $[0,1]^3$ and the solutions are computed on a grid of size $64 \times 64 \times 64$. *Source:* ncopies_R_dat.py (data), ncopies_R_fig.py (figure).

(see Remark 3.1.4). We can approximate the error term up to order 1.5 by using the exact expression for $\mathbf{L}$ derived in Appendix B.2. The last term (3.18c) is negligible because for a blob function $\Phi_\varepsilon(r)$ with zero second moment, the velocity due to $B_{\Phi_\varepsilon} - B$ decays like a Gaussian [LBCL13]. We emphasize that approximating the infinite double sum is significantly slower than using the FFT method and for us serves the only purpose of providing a reference solution for the FFT method.

3.1.7 Numerical validation

We compare the doubly periodic Stokeslet computed using FFTs (*see* Section 3.1.5) to an approximation of the Stokeslet double sum (*see* Section 3.1.6). The velocity field is created by 10 random forces with zero net force[4] and placed at random locations inside the cube $[0,1]^3$. The results are shown in Figure 3.2. As the number of periodic copies is increased the Stokeslet double sum converges to the FFT solution of order 0.5 without correction and order 1.5 with correction in relation to computational work.

---

[4] Recall the Stokeslet double sum converges only for zero net force (*see* Theorem 3.1.3).

3.2 Doubly-periodic flow near a wall

The method presented in this section is published in [HC].

When we derived the doubly periodic Stokeslet in free space we followed the derivation of the free space Stokeslet and just carried out all the computations in Fourier space. Similarly, in order to derive the doubly-periodic Stokeslet near an infinite planar wall we just take the two-dimensional Fourier transform of the method of images described in Eq. (2.18), which gives

$$
\mu \hat{\mathbf{u}}\left(k, m ; z\right)=\hat{\mathbf{St}}_{\mathbf{f}_0}^{\Phi_\varepsilon^s}\left(k, m ; \tilde{z}\right)-\hat{\mathbf{St}}_{\mathbf{f}_0}^{\Phi_\varepsilon^s}\left(k, m ; \tilde{z}^*\right)-2 h \hat{\mathbf{Do}}_{\mathbf{q}, \mathbf{e}_3}^{\Phi_\varepsilon^s}\left(k, m ; \tilde{z}^*\right) \tag{3.19}
$$
$$
-h^2 \hat{\mathbf{Dp}}_{\mathbf{q}}^{\Phi_\varepsilon^d}\left(k, m ; \tilde{z}^*\right)+2 h\left(\hat{\mathbf{Ro}}_{\mathbf{L}}^{\Phi_\varepsilon^s}\left(k, m ; \tilde{z}^*\right)-\hat{\mathbf{Ro}}_{\mathbf{L}}^{\Phi_\varepsilon^d}\left(k, m ; \tilde{z}^*\right)\right),
$$

where $\tilde{z}=z-z_0$ and $\tilde{z}^*=z+z_0$. Evaluating Eq. (3.19) on a grid and taking an inverse FFT gives a doubly-periodic Stokeslet that satisfies a no-slip condition at $z=0$. The derivation of the regularized image elements in Fourier space is also analogous to the free space case. Recall that in free space the regularized doublet (2.22), the regularized dipole (2.23) and the regularized rotlet (2.24) were obtained by differentiating the regularized Stokeslet (2.11) and the regularized Green's function, respectively. Similarly, in Fourier space we obtain the regularized Fourier space doublet, the regularized Fourier space dipole and the regularized Fourier space rotlet by differentiating

the regularized Fourier space Stokeslet (3.6) to give

$$
\mathbf{\hat{Do}}_{\mathbf{q,e_3}}^{\Phi_\varepsilon}(k,m;\tilde{z}) = -\hat{\nabla}\left(\mathbf{\hat{St}_q}(k,m;\tilde{z})\cdot\mathbf{e_3}\right)
$$

$$
= \begin{pmatrix}
(-q_1\tilde{k}^2 - q_2\tilde{k}\tilde{m})\hat{B}'_{\Phi_\varepsilon} + iq_3\tilde{k}\left(\tilde{k}^2+\tilde{m}^2\right)\hat{B}_{\Phi_\varepsilon} + iq_3\tilde{k}\hat{G}'_{\Phi_\varepsilon} \\
(-q_1\tilde{k}\tilde{m} - q_2\tilde{m}^2)\hat{B}'_{\Phi_\varepsilon} + iq_3\tilde{m}\left(\tilde{k}^2+\tilde{m}^2\right)\hat{B}_{\Phi_\varepsilon} + iq_3\tilde{m}\hat{G}'_{\Phi_\varepsilon} \\
i\left(q_1\tilde{k}+q_2\tilde{m}\right)\left(\tilde{k}^2+\tilde{m}^2\right)\hat{B}_{\Phi_\varepsilon} + q_3\left(\tilde{k}^2+\tilde{m}^2\right)\hat{B}'_{\Phi_\varepsilon}
\end{pmatrix},
$$

$$(3.20)$$

$$
\mathbf{\hat{Dp}}_{\mathbf{q}}^{\Phi_\varepsilon}(k,m;\tilde{z}) = -\hat{\Delta}\mathbf{\hat{St}_q}(k,m;\tilde{z})
$$

$$
= \begin{pmatrix}
(q_1\tilde{k}^2 + q_2\tilde{k}\tilde{m})\hat{G}_{\Phi_\varepsilon} - iq_3\tilde{k}\hat{G}'_{\Phi_\varepsilon} + q_1\hat{\Phi}_\varepsilon \\
(q_1\tilde{k}\tilde{m} + q_2\tilde{m}^2)\hat{G}_{\Phi_\varepsilon} - iq_3\tilde{m}\hat{G}'_{\Phi_\varepsilon} + q_2\hat{\Phi}_\varepsilon \\
-q_3\left(\tilde{k}^2+\tilde{m}^2\right)\hat{G}_{\Phi_\varepsilon} - i(q_1\tilde{k}+q_2\tilde{m})\hat{G}'_{\Phi_\varepsilon}
\end{pmatrix},
$$

$$(3.21)$$

$$
\mathbf{\hat{Ro}}_{\mathbf{L}}^{\Phi_\varepsilon}(k,m;\tilde{z}) = \mathbf{L}\times\hat{\nabla}\hat{G}_{\Phi_\varepsilon}
$$

$$
= \begin{pmatrix}
-f_1\hat{G}'_{\Phi_\varepsilon} \\
-f_2\hat{G}'_{\Phi_\varepsilon} \\
i\left(f_1\tilde{k}+f_2\tilde{m}\right)\hat{G}_{\Phi_\varepsilon}
\end{pmatrix},
$$

$$(3.22)$$

where the differential operators $\hat{\nabla}$ and $\hat{\Delta}$ are defined as in Eqs. (3.2)-(3.3).

3.2.1   The doubly-periodic image system for a particular blob

We use the Gaussian blob (2.15) for Φ_ε^s together with its companion blob Φ_ε^d from Eq. (2.25). The Fourier space expressions are

$$
\hat{\Phi}_\varepsilon^s(\tilde{z}) = \hat{\delta}_{x_0y_0}^\varepsilon\left[\frac{1}{4\sqrt{\pi}}\left(\frac{6}{\varepsilon}+\varepsilon c^2\right) - \frac{1}{\sqrt{\pi}\varepsilon^3}\tilde{z}^2\right]\exp\left(-\frac{\tilde{z}^2}{\varepsilon^2}\right),
$$

$$
\hat{\Phi}_\varepsilon^d(\tilde{z}) = \frac{\hat{\delta}_{x_0y_0}^\varepsilon}{\varepsilon\sqrt{\pi}}\exp\left(-\frac{\tilde{z}^2}{\varepsilon^2}\right),
$$

$\hat{*}_{\Phi_\varepsilon}(\tilde{z})$	n	$p_1(\tilde{z})$	$p_2(\tilde{z})$	$q(\tilde{z})$
$\hat{G}_{\Phi_\varepsilon^s}(\tilde{z})$	1	-4	-4	-2
$\hat{G}'_{\Phi_\varepsilon^s}(\tilde{z})$	0	4	-4	$4\frac{\tilde{z}}{\varepsilon}$
$\hat{B}_{\Phi_\varepsilon^s}(\tilde{z})$	3	$2+2c\tilde{z}$	$2-2c\tilde{z}$	$\frac{2}{c^2\varepsilon^2}$
$\hat{B}'_{\Phi_\varepsilon^s}(\tilde{z})$	2	$-2c\tilde{z}$	$-2c\tilde{z}$	0
$\hat{G}_{\Phi_\varepsilon^d}(\tilde{z})$	1	-4	-4	0
$\hat{G}'_{\Phi_\varepsilon^d}(\tilde{z})$	0	4	-4	0

$$\hat{*}_{\Phi_\varepsilon}(\tilde{z}) = \frac{\hat{\delta}^\varepsilon_{x_0 y_0}}{16 c^n} \exp\left(\frac{c^2\varepsilon^2}{4}\right)\left[p_1(\tilde{z})\exp(-c\tilde{z})\operatorname{erfc}\left(\frac{c\varepsilon}{2}-\frac{\tilde{z}}{\varepsilon}\right) + p_2(\tilde{z})\exp(c\tilde{z})\operatorname{erfc}\left(\frac{c\varepsilon}{2}+\frac{\tilde{z}}{\varepsilon}\right)\right]$$
$$+\frac{\hat{\delta}^\varepsilon_{x_0 y_0}\varepsilon^n}{8\sqrt{\pi}}q(\tilde{z})\exp\left(-\frac{\tilde{z}^2}{\varepsilon^2}\right)$$

Table 3.2: Green's functions in Fourier space for $c \neq 0$.

where again the factor $\hat{\delta}^\varepsilon_{x_0 y_0} = \exp(-\frac{1}{4}\varepsilon^2 c^2)\exp(-\frac{2\pi i}{L}(kx_0 + my_0))$ contains the dependence on x_0 and y_0. The Fourier space Laplace equations (3.4)-(3.5) can now be solved analytically for the Fourier space Green's function. We consider the cases $c = 0$ and $c \neq 0$ separately, as we did previously when computing the Fourier space Stokeslet. For $c \neq 0$, the corresponding Green's functions are given in Table 3.2 [5]. We chose the constants of integration so that the Green's functions go to zero as $|z| \to \infty$ since otherwise both the Green's function and the fluid velocity would grow exponentially in z. These boundary conditions also ensure that the Green's functions are symmetric in z about the force location. When $c = 0$ the image elements from Eqs. (3.6), (3.20)-(3.22) simplify to

---

[5] see Footnote 3

$\hat{\ast}_{0,\Phi_\varepsilon}(\tilde{z})$	n	$p(\tilde{z})$	$q(\tilde{z})$
$\hat{G}_{0,\Phi_\varepsilon^s}(\tilde{z})$	1	$\tilde{z}$	$\frac{1}{2}$
$\hat{G}'_{0,\Phi_\varepsilon^s}(\tilde{z})$	0	1	$\frac{\tilde{z}}{\varepsilon}$
$\hat{G}_{0,\Phi_\varepsilon^d}(\tilde{z})$	1	$\tilde{z}$	1
$\hat{G}'_{0,\Phi_\varepsilon^d}(\tilde{z})$	0	1	0

$$\hat{\ast}_{0,\Phi_\varepsilon}(\tilde{z}) = \frac{1}{2}p(\tilde{z})\operatorname{erf}\left(\frac{\tilde{z}}{\varepsilon}\right) + \frac{\varepsilon^n}{2\sqrt{\pi}}q(\tilde{z})\exp\left(-\frac{\tilde{z}^2}{\varepsilon^2}\right)$$

Table 3.3: Green's functions in Fourier space for $c = 0$. The function $\hat{B}_0$ is not needed.

$$\hat{\mathbf{St}}_{\mathbf{f}_0}^{\Phi_\varepsilon}(\tilde{z}) = \begin{pmatrix} -f_1\hat{G}_{0,\Phi_\varepsilon} \\ -f_2\hat{G}_{0,\Phi_\varepsilon} \\ 0 \end{pmatrix}, \tag{3.23}$$

$$\hat{\mathbf{Do}}_{\mathbf{q},\mathbf{e}_3}^{\Phi_\varepsilon}(\tilde{z}) = \mathbf{0}, \tag{3.24}$$

$$\hat{\mathbf{Dp}}_{\mathbf{q}}^{\Phi_\varepsilon}(\tilde{z}) = \begin{pmatrix} q_1\hat{\Phi}_\varepsilon \\ q_2\hat{\Phi}_\varepsilon \\ 0 \end{pmatrix}, \tag{3.25}$$

$$\hat{\mathbf{Ro}}_{\mathbf{L}}^{\Phi_\varepsilon}(\tilde{z}) = \begin{pmatrix} -f_1\hat{G}'_{0,\Phi_\varepsilon} \\ -f_2\hat{G}'_{0,\Phi_\varepsilon} \\ 0 \end{pmatrix}. \tag{3.26}$$

The corresponding Green's functions are obtained from solving the Fourier space Laplace equations (3.4)-(3.5) for $c = 0$ and are given in Table 3.3 [6]. We chose the constants of integration so that $\hat{G}_{\Phi_\varepsilon}$ is symmetric in z, as we did in Section 3.1.4. We note that this choice of constants gives the same fluid velocity in the limit $z \to \infty$ that was obtained in [Bla72] by writing the velocity as an infinite double sum of the Stokeslet and the image system and taking the spatial average in x and y. This result is summarized in the following theorem.

---

[6] *see* Footnote 3

Theorem 3.2.1. *Let* **u** *be the fluid velocity that is due to a point force* $\mathbf{f_0} = (f_1, f_2, f_3)$ *located at* $\mathbf{x} = (x_0, y_0, z_0)$ *and distributed periodically in* x *and* y *with periods* L_x *and* L_y. *Let the* **u** *be zero at the planar wall* $z = 0$. *Then*

$$\lim_{z \to \infty} \mu \mathbf{u}\left(z\right) = \frac{z_0}{L_x L_y} \begin{pmatrix} f_1 \\ f_2 \\ 0 \end{pmatrix}. \tag{3.27}$$

Proof. It is straightforward to show that $\lim_{z \to \infty} \hat{\mathbf{u}}(k, m; z) = \mathbf{0}$ for $(k, m) \neq \mathbf{0}$. Therefore we only need to compute the zero wave number term, which is

$$\mu \hat{\mathbf{u}}\left(0, 0; z\right) = \hat{G}_{0, \Phi_\varepsilon^s}\left(z - z_0\right) \begin{pmatrix} -f_1 \\ -f_2 \\ 0 \end{pmatrix} + \hat{G}_{0, \Phi_\varepsilon^s}\left(z - z_0^*\right) \begin{pmatrix} f_1 \\ f_2 \\ 0 \end{pmatrix} - h^2 \hat{\Phi}_\varepsilon^d \left(z - z_0^*\right) \begin{pmatrix} q_1 \\ q_2 \\ 0 \end{pmatrix}$$

$$+ 2h \left(\hat{G}_{0, \Phi_\varepsilon^s}'\left(z - z_0\right) \begin{pmatrix} -f_1 \\ -f_2 \\ 0 \end{pmatrix} + \hat{G}_{0, \Phi_\varepsilon^d}'\left(z - z_0\right) \begin{pmatrix} f_1 \\ f_2 \\ 0 \end{pmatrix} \right),$$

where

$$\hat{G}_{0,\Phi_\varepsilon^s}(z-z_0)\begin{pmatrix}-f_1\\-f_2\\0\end{pmatrix}+\hat{G}_{0,\Phi_\varepsilon^s}(z-z_0^*)\begin{pmatrix}f_1\\f_2\\0\end{pmatrix}$$

$$=\frac{1}{2}(-z+z_0)\operatorname{erf}\left(\frac{z-z_0}{\varepsilon}\right)+\frac{\varepsilon}{4\sqrt{\pi}}\exp\left(-\frac{(z-z_0)^2}{\varepsilon^2}\right)\begin{pmatrix}f_1\\f_2\\0\end{pmatrix}$$

$$+\frac{1}{2}(z+z_0)\operatorname{erf}\left(\frac{z+z_0}{\varepsilon}\right)+\frac{\varepsilon}{4\sqrt{\pi}}\exp\left(-\frac{(z+z_0)^2}{\varepsilon^2}\right)\begin{pmatrix}f_1\\f_2\\0\end{pmatrix}$$

$$=\left[\frac{z_0}{2}\left(\operatorname{erf}\left(\frac{z+z_0}{\varepsilon}\right)+\operatorname{erf}\left(\frac{z-z_0}{\varepsilon}\right)\right)+\frac{z}{2}\left(\operatorname{erf}\left(\frac{z+z_0}{\varepsilon}\right)-\operatorname{erf}\left(\frac{z-z_0}{\varepsilon}\right)\right)\right.$$

$$\left.+\frac{\varepsilon}{4\sqrt{\pi}}\left(\exp\left(-\frac{(z+z_0)^2}{\varepsilon^2}\right)+\exp\left(-\frac{(z-z_0)^2}{\varepsilon^2}\right)\right)\right]\begin{pmatrix}f_1\\f_2\\0\end{pmatrix},$$

$$-h^2\hat{\Phi}_\varepsilon^d(z-z_0^*)\begin{pmatrix}q_1\\q_2\\0\end{pmatrix}=\frac{-h^2}{\varepsilon\sqrt{\pi}}\exp\left(-\frac{\tilde{z}^2}{\varepsilon^2}\right)\begin{pmatrix}q_1\\q_2\\0\end{pmatrix},$$

and

$$2h \left(\hat{G}'_{0,\Phi^s_\varepsilon}(z - z_0) \begin{pmatrix} -f_1 \\ -f_2 \\ 0 \end{pmatrix} + \hat{G}'_{0,\Phi^d_\varepsilon}(z - z_0) \begin{pmatrix} f_1 \\ f_2 \\ 0 \end{pmatrix} \right)$$

$$= \left[-\frac{1}{2} \operatorname{erf}\left(\frac{z - z_0}{\varepsilon} \right) - \frac{z - z_0}{2\sqrt{\pi}\varepsilon} \exp\left(-\frac{(z - z_0)^2}{\varepsilon^2} \right) + \frac{1}{2} \operatorname{erf}\left(\frac{z + z_0}{\varepsilon} \right) \right] \begin{pmatrix} f_1 \\ f_2 \\ 0 \end{pmatrix}.$$

It directly follows that

$$\lim_{z \to \infty} \mu \hat{\mathbf{u}}(0, 0; z) = z_0 \begin{pmatrix} f_1 \\ f_2 \\ 0 \end{pmatrix}.$$

Taking the inverse FFT as defined in Eq. (3.1) gives Eq. (3.27). $\qquad \square$

3.2.2 Summary of the method

<div style="border:1px solid red">

The doubly-periodic Stokeslet near a planar wall using FFTs

Consider a *regularized* point force with strength $\mathbf{f}_0$ centered at $\mathbf{x}_0$ and distributed periodically in x and y with periods L_x and L_y. The doubly-periodic fluid velocity $\mathbf{u}$ that satisfies the no-slip condition $\mathbf{u}|_{z=0} = \mathbf{0}$ can be found by performing the following algorithm. The algorithm finds $\mathbf{u}$ on an (x, y) grid for fixed z (see also Figure 3.1). The fluid velocity can be interpolated to an arbitrary point $\mathbf{x}$ if needed.

1. Evaluate $\hat{\mathbf{u}}$ on a grid of wave numbers (k, m) using Eq. (3.19).

   - For $(k, m) \neq \mathbf{0}$ the image elements are defined in Eqs. (3.6),(3.20)-(3.22) and the corresponding Green's functions are defined in Table 3.2.

   - For $(k, m) = \mathbf{0}$ the image elements are defined in Eqs. (3.23)-(3.26) and the corresponding Green's functions are defined in Table 3.3.

</div>

z_0	$\varepsilon = 0.0625$	$\varepsilon = 0.3$
0.5	$6.19 \cdot 10^{-17}$	$9.82 \cdot 10^{-17}$
0.1	$1.47 \cdot 10^{-16}$	$2.20 \cdot 10^{-17}$
0.05	$1.65 \cdot 10^{-16}$	$1.82 \cdot 10^{-17}$

Table 3.4: Maximum velocity at the wall $z = 0$ where a no-slip condition of the velocity is enforced. The flow is due to 10 random regularized doubly-periodic forces placed at random locations at height z_0 above the wall. Since the method of regularized images models the no-slip condition exactly, the error is of order machine accuracy independent of the distance of the forces from the wall and the regularization parameter ε. *Source:* flow_at_wall.py.

The doubly-periodic Stokeslet near a planar wall using FFTs (Continued)

2. Find **u** on the grid by taking an inverse FFT according to Eq. (3.1).

The algorithm gives good results if $\varepsilon \geq 4\Delta x$, where ε is the regularization parameter and Δx is the grid size. If the condition is violated, one needs to use Ewald splitting (Section 4.3.3).

3.2.3 Numerical validation

At first we check the no-slip condition. Since the method of images models the no-slip condition exactly, the error at the wall is of order machine accuracy even when the force is close to the wall and a large blob size is used (*see* Table 3.4). We also compute the velocity profile due to a single point force (*see* Figure 3.3). Above the force location the fluid velocity approaches the limit velocity predicted by Eq. (3.27) exponentially fast, which can also be seen from the proof of Theorem 3.2.1 and which is further verified numerically in Figure 3.4.
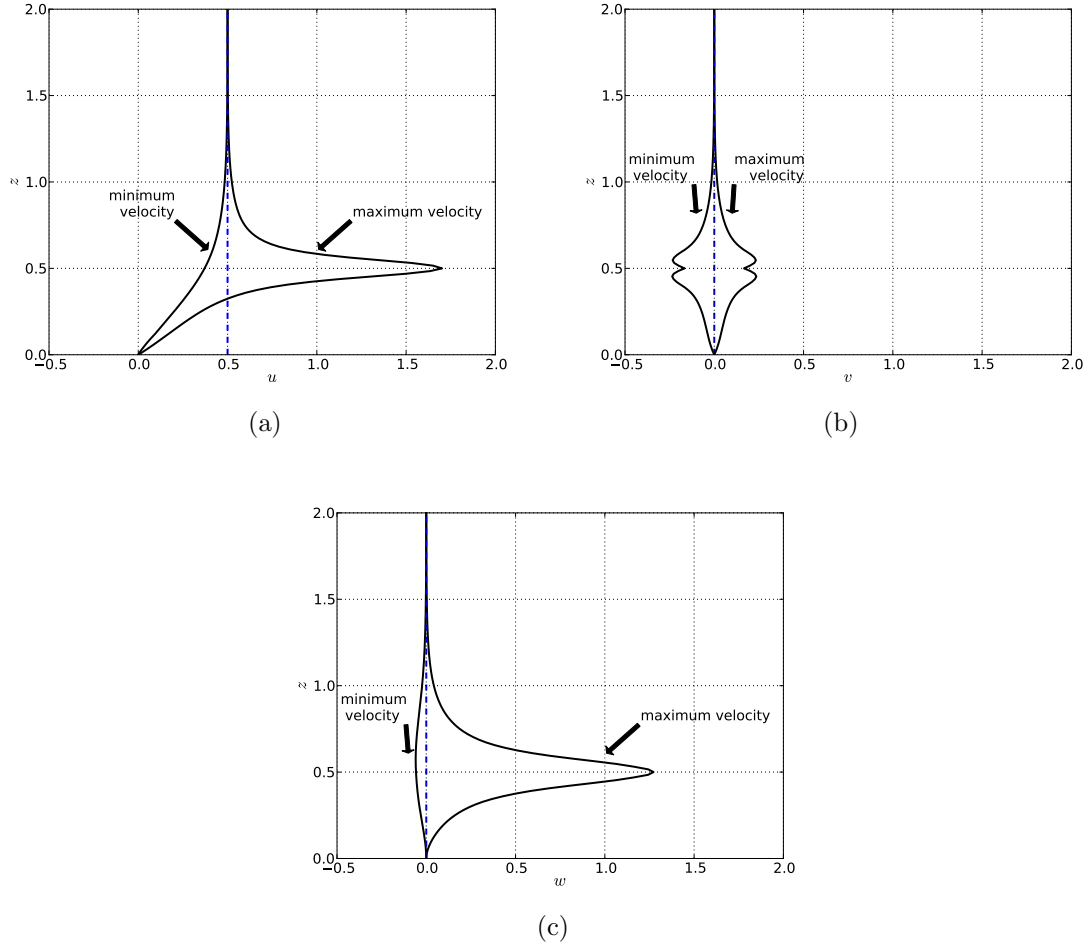
(a)

(b)

(c)

Figure 3.3: A doubly periodic regularized force ($\varepsilon = 0.0625$) of strength $\mathbf{f}_0 = (1, 0, 1)$ is placed at height $z_0 = 0.5$ above a wall at $z = 0$. Shown is the maximal and minimal velocity in (a) the x direction, (b) the y direction and (c) the z direction in relation to the height z above the wall. The period in x and y is $L_x = L_y = 1$. The dashed line gives the exact velocity as $z \to \infty$ based on Eq. (3.27). Here the limit velocity in the y direction is 0 only because there is no contribution of the force in y. In general the limit velocity in x and y is nonzero. *Source:* flow_at_z_layers.py.
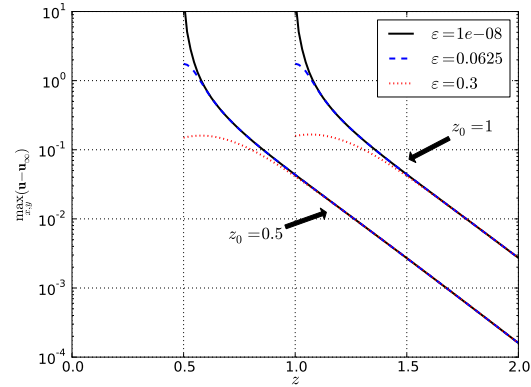

Figure 3.4: Maximum difference between the computed velocity $\mathbf{u}$ and the limit velocity $\mathbf{u}_\infty$ from Eq. (3.27). The set up is the same as in Figure 3.3. The convergence $\mathbf{u} \to \mathbf{u}_\infty$ is exponential as was seen from the proof of Theorem 3.2.1. We note that for small ε the solution was computed using FFTs and Ewald splitting. *Source:* convergence_in_z.py.

Chapter 4

Doubly-periodic Stokes flow in 3D using FFTs and Ewald splitting

In the previous chapter we introduced a numerical method to compute the doubly-periodic velocity field due to a regularized point force in free space and in the presence of an infinite planar wall. The fluid velocity is found by fixing z, evaluating the exact expressions of the velocity field in Fourier space on a grid of wave numbers (k, m), and taking an inverse FFT. This gives the velocity field on a grid of (x, y) values at the height z. Repeating the process at various values of z produces the solution on a three-dimensional grid from which the velocity can be interpolated to other points. It is crucial for our method that the Fourier space expressions are smooth so that the inverse FFT can be computed accurately. Since we regularized the force field, the derived Fourier space expressions are indeed smooth but depending on the FFT grid another condition is needed. In particular, if the regularization parameter ε is too small compared to grid size Δx, the blob Φ_ε is narrow and spiky and cannot be resolved on the grid properly. When this happens, the inverse FFT becomes inaccurate. Increasing ε may not be a viable option if ε should be chosen on the order of some physical parameter. Refining the grid will increase the computational

expense.

Instead, we consider the following Ewald splitting of the Green's function

$$B_{\Phi_\varepsilon}(r) = \underbrace{B(r)\operatorname{erf}\left(\frac{r}{\xi}\right)}_{\text{regular}} + \underbrace{B_{\Phi_\varepsilon}(r) - B(r)\operatorname{erf}\left(\frac{r}{\xi}\right)}_{\text{fast decaying}}.$$

The first term on the right side is smooth enough to be treated in with FFTs as described above if the splitting parameter is chosen so that $\xi \geq 4\Delta x$ (*see* Section 4.2.4). The second term is localized and can be computed directly in physical space where periodicity is accounted for by placing identical copies of the force $\mathbf{f}_0$ in x and y. Because of the fast decay, this term need only be evaluated at points within a cutoff radius of $r_{\text{cutoff}} \approx 8\xi$ of a force (*see* Section 4.2.4).

4.1 Ewald splitting

One approach to solving the doubly-periodic Stokes problem in three dimensions is to sum over the forces exerted in the main domain and to this velocity add the contribution of all the periodic copies of the forces. The resulting infinite double sum was investigated in Theorem 3.1.3, where we showed that direct numerical evaluation is inefficient because of the slow convergence rate. One way to evaluate the sum more efficiently is to separate the velocity formula into a smooth part and a rapidly-decaying part. The smooth part can be approximated well and computed fast in Fourier space while the rapidly-decaying part can be computed efficiently in the physical domain. The decomposition requires the selection of a splitting parameter ξ that balances the work required to approximate the sums (*see* Figure 4.1).

Hasimoto [Has59] was the first to use the splitting into a Fourier space sum and a physical space sum when he computed Stokes flow past periodic arrays of spheres and cylinders. Work by Sierou and Brady [SB01] and Saintillan et al. [SDS05] uses FFTs
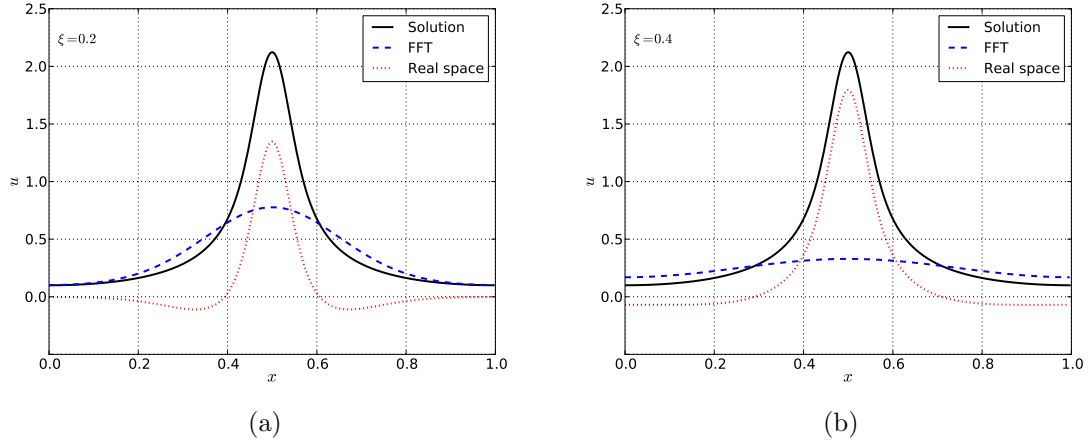
Figure 4.1: Shown is the x-component of the velocity field that is due to a doubly-periodic point force centered at $\mathbf{x}_0 = (0.5, 0, 0)$ and pointing in the x direction. The velocity is evaluated at the line $(x, 0, 0)$ and the period in x is set to $L_x = 1$. (a): The real space solution approximates the velocity near the force location and decays to 0 at the edges of the box. Periodicity is entirely taken care of by the FFT solution, which remains smooth around the force location. (b): If the splitting parameter is increased, the real space solution represent a larger portion of the peak but also decays slower. In this case, since the real space solution is non-zero at the edges of the box, ghost images of periodic copies of the force are needed. The FFT solution, however, has gained additional smoothness. *Source: ewald.py*.

to compute the Fourier space sum in an Ewald splitting for triply-periodic domains. They first interpolate the force field onto a regular mesh, take the FFT of the forces, and then compute the velocities using inverse FFTs. Other fast modern numerical methods for triply-periodic arrays of forces include general geometry Ewald-like methods (GGEM) [HOdPG07] and spectrally accurate methods [LT10]. Methods dealing with planar periodicity are usually derived from methods solving the triply-periodic problem [Poz96, LT11]. There the Fourier space sum is evaluated by computing the Fourier integrals exactly. Bleibel [Ble12] develops a formula for doubly-periodic flows in three dimensions for the special case when all interacting particles are within a single plane parallel to the xy-plane.

In our approach the infinite sum in the Fourier domain is replaced by an FFT on a grid. The Fourier space expressions are smooth since we use the method of regularized Stokeslet to remove the singularity. In some cases the smoothness introduced by the regularized Stokeslet is already sufficient for the Fourier space expressions to be computed accurately and it is not needed to split off a fast-decaying piece for

additional smoothness. Only if the regularization parameter ε, which is required to be small for numerical accuracy, is small compared to the grid size Δx do we need the extra smoothness introduced by the Ewald splitting. In such a case we consider the Ewald splitting

$$B_{\Phi_\varepsilon}(r) = \underbrace{B(r)\operatorname{erf}\left(\frac{r}{\xi}\right)}_{\text{regular}} + \underbrace{B_{\Phi_\varepsilon}(r) - B(r)\operatorname{erf}\left(\frac{r}{\xi}\right)}_{\text{regular and fast decaying}}, \tag{4.1}$$

where $B(r) = -r/8\pi$ is the Green's function corresponding to the singular problem in Eq. (2.4) and B_{Φ_ε} is the regularized Green's function.

The first term on the right side of Eq. (4.1) we compute in Fourier space with FFTs as described in Section 3.1. This procedure requires the splitting parameter ξ to be large enough compared to the grid size in order for the regularization to be resolved on the grid. Note that necessarily $\xi \geq \varepsilon$ since otherwise the splitting would not introduce any regularity additional to the one coming from regularizing the forces. In order to compute the velocity field in Fourier space, similar to Section 3.1 we have to compute the regularized Green's function in Fourier space. The only difference is that in physical space we now start with the Green's function $B_{\Psi_\xi} = B(r)\operatorname{erf}\left(\frac{r}{\xi}\right)$. It turns out that computing the two-dimensional Fourier transform of B_{Ψ_ξ} directly from its definition is not easily done since the term $\operatorname{erf}(r)$ does not allow us to separate the variable z as before. What we do instead is to find twice the Laplacian of B_{Ψ_ξ} to give the corresponding blob function

$$\begin{aligned} \Psi_\xi(r) &= \Delta^2\left(B(r)\operatorname{erf}\left(\frac{r}{\xi}\right)\right) \\ &= \frac{1}{\xi^3 \pi^{\frac{3}{2}}}\left(10 - 11\frac{r^2}{\xi^2} + 2\frac{r^4}{\xi^4}\right)\exp\left(-\frac{r^2}{\xi^2}\right). \end{aligned} \tag{4.2}$$

The blob function Ψ_ξ is quite similar to blob (2.15) and also has the first three moments equal to zero, which is good for accuracy (compare to Section 2.3.1). The

Fourier transform $\Psi_\xi(r)$ is also easy to compute. Once we compute the Fourier transform of Ψ_ξ, we can solve for the corresponding Green's function analytically in Fourier space.

The last two terms on the right side of Eq. (4.1) each converge to the singular Green's function B for $r >> \xi, \varepsilon$ and, as a result, cancel each other. Therefore, the velocity derived from the difference of the two terms is local and can be computed directly as a sum of regularized Stokeslets in physical space. We incorporate periodicity by placing copies of forces in the x and y-direction. In order to keep computational costs to a minimum, we require the two terms to decay fast, demanding ξ to be as small as possible.

There are two opposing requirements for the splitting parameter ξ. On the one hand we need ξ to be large enough to guarantee enough smoothness for the FFT to be accurate. On the other hand we want ξ to be as small as possible in order to ensure fast decay of the terms in real space. This trade-off is similar to the classical approach where the regular term of the Ewald splitting is computed using infinite series in spectral space. In that approach the splitting parameter ξ is a compromise between a large value, which is desired for the spectral sum to converge fast, and a small value, which is desired for the fast-decaying term to converge fast. Results from [Bee86] indicate that the splitting parameter is best chosen on the order of the period L. In the method presented here, since the regular term is computed with FFTs on a grid, the splitting parameter ξ needs to be only slightly larger than the grid size Δx in order to resolve the blob function on the grid. Therefore, in our method, ξ is typically a small multiple of the grid size. This makes the infinite sum in the last terms in Eq. (4.1) (including the periodic copies of the forces) decay extremely fast. Additionally, the last two terms on the right side of Eq. (4.1) together decay like a Gaussian, which is a consequence of the fact that Φ_ε and Ψ_ξ have second moment zero [LBCL13]. The result is that only forces within a cutoff radius of a few ξ need

to be considered, as shown in the section of numerical results.

For our method, the splitting in Eq. (4.1) has two advantages over an Ewald splitting of the type used in [Poz96], which has the form

$$B_{\Phi_\varepsilon}(r) = \underbrace{B_{\Phi_\varepsilon}(r)\operatorname{erf}\left(\frac{r}{\xi}\right)}_{\text{regular}} + \underbrace{B_{\Phi_\varepsilon}(r)\operatorname{erfc}\left(\frac{r}{\xi}\right)}_{\text{regular and fast decaying}} . \tag{4.3}$$

One reason is that the regular piece in (4.1) is independent of the blob function Φ_ε and does not need to be recomputed when a different blob is used. In particular, the regular piece is the same even when no blob is used. However, in that case of course the fast-decaying piece would exhibit a singularity. A more practical reason for why we choose the splitting (4.1) over (4.3) is that the Fourier transform of the regular piece in Eq. (4.3) is difficult to determine analytically, even when Gaussian blobs are used. This is mainly due to our inability to compute the Fourier transform of $\operatorname{erf}(r)$ in (x, y) only. When we ran into the same problem with splitting (4.1), we found a remedy in taking two Laplacians. In fact, Eq. (4.2) eliminates the need to compute the two-dimensional Fourier transform of $\operatorname{erf}(r)$. For splitting (4.3) even this trick does not work and we are therefore unable to proceed with the FFT-method.

4.2 Doubly-periodic flow in free space

The method presented in this section is published in [CH14].

4.2.1 The formulas in Fourier space

The regular term in Eq. (4.1) can be treated with the methods developed in Section 3.1, using the expression for velocity in Eq. (3.6). The only difference is that we use blob (4.2) instead of blob (2.15). To complete the description of this piece, the

expressions for $\hat{G}_{\Psi_\xi}$ and $\hat{B}_{\Psi_\xi}$ need to be derived. Replacing the right-hand side in Eq. (3.4) with the Fourier transform of blob (4.2) gives

$$\hat{G}''_{\Psi_\xi}(\tilde{z}) - c^2 \hat{G}_{\Psi_\xi}(\tilde{z})$$
$$= \frac{\hat{\delta}^\xi_{x_0y_0}}{8\xi^5\sqrt{\pi}} \left[16\tilde{z}^4 - 56\xi^2\tilde{z}^2 - 8\xi^4\left(-3 + c^2\tilde{z}^2\right) + 6\xi^6c^2 + \xi^8c^4\right] \exp\left(-\frac{\tilde{z}^2}{\xi^2}\right),$$

where again $\tilde{z} = z - z_0$, $c = \frac{2\pi}{L}\sqrt{k^2 + m^2}$ and $\hat{\delta}^\xi_{x_0y_0} = \exp(-\frac{1}{4}\xi^2c^2)\exp(-\frac{2\pi i}{L}(kx_0 + my_0))$. This ordinary differential equation can be solved exactly[1] to produce for $c \neq 0$

$$\hat{G}_{\Psi_\xi}(\tilde{z}) = -\frac{\hat{\delta}^\xi_{x_0y_0}}{4c}\exp\left(\frac{\xi^2c^2}{4}\right)\left[\exp\left(-c\tilde{z}\right)\operatorname{erfc}\left(\frac{c\xi}{2} - \frac{\tilde{z}}{\xi}\right) + \exp\left(c\tilde{z}\right)\operatorname{erfc}\left(\frac{c\xi}{2} + \frac{\tilde{z}}{\xi}\right)\right]$$
$$- \frac{\hat{\delta}^\xi_{x_0y_0}}{4\xi\sqrt{\pi}}\left(2\xi^2 + \frac{1}{2}\xi^4c^2 - 2\tilde{z}^2\right)\exp\left(-\frac{\tilde{z}^2}{\xi^2}\right), \tag{4.4}$$

$$\hat{B}_{\Psi_\xi}(\tilde{z}) = \frac{\hat{\delta}^\xi_{x_0y_0}}{8c^3}\exp\left(\frac{c^2\xi^2}{4}\right)$$
$$\cdot \left[(1 + c\tilde{z})\exp\left(-c\tilde{z}\right)\operatorname{erfc}\left(\frac{c\xi}{2} - \frac{\tilde{z}}{\xi}\right) + (1 - c\tilde{z})\exp\left(c\tilde{z}\right)\operatorname{erfc}\left(\frac{c\xi}{2} + \frac{\tilde{z}}{\xi}\right)\right]$$
$$+ \frac{\hat{\delta}^\xi_{x_0y_0}\xi}{4\sqrt{\pi}c^2}\left(1 + \frac{\xi^2c^2}{2}\right)\exp\left(-\frac{\tilde{z}^2}{\xi^2}\right), \tag{4.5}$$

$$\hat{B}'_{\Psi_\xi}(\tilde{z}) = -\frac{\hat{\delta}^\xi_{x_0y_0}}{8c}\exp\left(\frac{c^2\xi^2}{4}\right)$$
$$\cdot \left[\tilde{z}\exp\left(-c\tilde{z}\right)\operatorname{erfc}\left(\frac{c\xi}{2} - \frac{\tilde{z}}{\xi}\right) + \tilde{z}\exp\left(c\tilde{z}\right)\operatorname{erfc}\left(\frac{c\xi}{2} + \frac{\tilde{z}}{\xi}\right)\right]$$
$$- \frac{\hat{\delta}^\xi_{x_0y_0}\xi}{4\sqrt{\pi}}\tilde{z}\exp\left(-\frac{\tilde{z}^2}{\xi^2}\right). \tag{4.6}$$

The constants of integration are again chosen so that $\hat{G}_{\Psi_\xi}(\tilde{z})$ and $\hat{B}_{\Psi_\xi}(\tilde{z})$ approach 0 as $|z| \to \infty$ since otherwise the Green's function and the resulting velocity would grow exponentially in z. It is straightforward to verify that taking the limit $\xi \to 0$ produces the singular formulas (3.11) and (3.12). If $c = 0$, the Green's function takes

---

[1] *see* Mathematica notebook GreensFunctionsFourierSpace.nb (also GreensFunctionsFourierSpace.pdf)

the form

$$\hat{G}_{0,\Psi_\xi}(\tilde{z}) = \frac{\tilde{z}}{2}\,\text{erf}\left(\frac{\tilde{z}}{\xi}\right) + \frac{\tilde{z}^2}{2\sqrt{\pi}\xi}\exp\left(-\frac{\tilde{z}^2}{\xi^2}\right), \tag{4.7}$$

where again we chose the constants of integration so that $\hat{G}_{0,\Psi_\xi}$ is a regularized version of Eq. (3.15). The Green's functions can now be readily plugged into Eqs. (3.6) and (3.13), respectively.

4.2.2 Local sum in physical space

The fast-decaying piece in Eq. (4.1), which can be written as $B_{\Phi_\varepsilon} - B_{\Psi_\xi}$, is treated in infinite space where periodicity is being accounted for by placing periodic copies of the forces in the main domain in the x and y-direction. As mentioned before, it suffices to place only copies of forces that fall within a few multiples of ξ from the boundaries of the main domain in each direction because of the Gaussian decay. In detail, solving the regularized Laplace Eq. (2.9) in spherical coordinates

$$(rG_{\Phi_\varepsilon}(r))'' = r\Phi_\varepsilon(r),$$

where Φ_ε is as in Eq. (2.15), yields the radially symmetric Green's function[2]

$$G_{\Phi_\varepsilon}(r) = -\frac{\text{erf}\left(\frac{r}{\varepsilon}\right)}{4\pi r} - \frac{\exp\left(-\frac{r^2}{\varepsilon^2}\right)}{4\varepsilon\pi^{\frac{3}{2}}}.$$

In the limit $\varepsilon \to 0$, this produces $G(r) = -\frac{1}{4\pi r}$ as expected. Similarly, from Eq. (2.10) we obtain

$$B_{\Phi_\varepsilon}(r) = -\frac{r\,\text{erf}\left(\frac{r}{\varepsilon}\right)}{8\pi} - \frac{\varepsilon\exp\left(-\frac{r^2}{\varepsilon^2}\right)}{8\pi^{\frac{3}{2}}} = \frac{-1}{8\pi}\int \text{erf}\left(\frac{r}{\varepsilon}\right)dr, \tag{4.8}$$

---

[2] *see* Mathematica notebook GreensFunctionsRealSpaceEwald.nb (also GreensFunctionsRealSpaceEwald.pdf)

which as $\varepsilon \to 0$ has the limit

$$B(r) = -\frac{r}{8\pi}. \tag{4.9}$$

Using (4.8) and (4.9), the fast-decaying piece in Eq. (4.1) can be represented as

$$B_{\Phi_\varepsilon}(r) - B(r)\operatorname{erf}\left(\frac{r}{\xi}\right) = \frac{r\operatorname{erf}\left(\frac{r}{\xi}\right) - r\operatorname{erf}\left(\frac{r}{\varepsilon}\right)}{8\pi} - \frac{\varepsilon\exp\left(-\frac{r^2}{\varepsilon^2}\right)}{8\pi^{\frac{3}{2}}}.$$

The velocity field produced by this combination is

$$\mu\mathbf{u}(\mathbf{x}) = ((\mathbf{f}_0 \cdot \nabla)\nabla - \mathbf{f}_0\Delta)\left(B_{\Phi_\varepsilon}(r) - B(r)\operatorname{erf}\left(\frac{r}{\xi}\right)\right)$$

$$= H_1^{\Phi_\varepsilon - \Psi_\xi}(r)\mathbf{f}_0 + H_2^{\Phi_\varepsilon - \Psi_\xi}(r)(\mathbf{f}_0 \cdot \tilde{\mathbf{x}})\tilde{\mathbf{x}}, \tag{4.10}$$

where $\tilde{\mathbf{x}} = \mathbf{x} - \mathbf{x_0}$ and

$$H_1^{\Phi_\varepsilon - \Psi_\xi}(r) = \frac{1}{8\pi^{\frac{3}{2}}}\left[\left(-\frac{6}{\xi} + \frac{4r^2}{\xi^3}\right)\exp\left(-\frac{r^2}{\xi^2}\right) + \frac{2}{\varepsilon}\exp\left(-\frac{r^2}{\varepsilon^2}\right)\right]$$
$$- \frac{1}{8\pi r}\left[\operatorname{erf}\left(\frac{r}{\xi}\right) - \operatorname{erf}\left(\frac{r}{\varepsilon}\right)\right],$$

$$H_2^{\Phi_\varepsilon - \Psi_\xi}(r) = \frac{1}{8\pi^{\frac{3}{2}}r^2}\left[\left(\frac{2}{\xi} - \frac{4r^2}{\xi^3}\right)\exp\left(-\frac{r^2}{\xi^2}\right) - \frac{2}{\varepsilon}\exp\left(-\frac{r^2}{\varepsilon^2}\right)\right]$$
$$- \frac{1}{8\pi r^3}\left[\operatorname{erf}\left(\frac{r}{\xi}\right) - \operatorname{erf}\left(\frac{r}{\varepsilon}\right)\right].$$

4.2.3   Summary of the method

The doubly-periodic Stokeslet using FFTs and Ewald splitting

Consider a *regularized* point force with strength $\mathbf{f}_0$ centered at $\mathbf{x}_0$ and distributed periodically in x and y with periods L_x and L_y. The doubly-periodic fluid velocity $\mathbf{u}$ can be found by performing the following algorithm. The algorithm finds $\mathbf{u}$ on an (x, y) grid for fixed z (see also Figure 3.1). The fluid velocity can be interpolated to an arbitrary point $\mathbf{x}$ if needed.

1. Evaluate the regular part of the velocity field $\hat{\mathbf{u}}_{\text{reg}}$ on a grid of wave

> ### The doubly-periodic Stokeslet using FFTs and Ewald splitting (Continued)
>
> numbers (k, m).
>
> - For $(k, m) \neq \mathbf{0}$ the velocity is computed from Eq. (3.6) with Φ_ε replaced by Ψ_ξ, where the corresponding Green's functions are defined in Eqs. (4.4)-(4.6).
> - For $(k, m) = \mathbf{0}$ the velocity is computed from Eq. (3.13) with Φ_ε replaced by Ψ_ξ, where the corresponding Green's functions is defined in Eq. (4.7).
>
> Then find $\mathbf{u}_{\mathrm{reg}}$ on the grid by taking an inverse FFT according to Eq. (3.1).
>
> 2. Find the local part of the velocity field $\mathbf{u}_{\mathrm{loc}}$ by computing Eq. (4.10). In order to find the velocity at a grid point, only forces within radius $r_{\mathrm{cutoff}} = 8\xi$ need to be considered but it may be necessary to place periodic copies of $\mathbf{f}_0$ in x and y.
>
> 3. Compute $\mathbf{u} = \mathbf{u}_{\mathrm{loc}} + \mathbf{u}_{\mathrm{reg}}$.
>
> *Note:* If $\varepsilon \geq 4\Delta x$, splitting is not needed and the method from Section 3.1.5 should be used instead.

4.2.4   Numerical validation

Ewald splitting versus no splitting.   We place 10 random forces with zero net force at random locations inside the cube $[0, 1]^3$ and analyze the results produced with and without splitting. We first compute the relative difference between the method implemented without splitting and the method using Ewald splitting for a range of values of ε. For the Ewald splitting implementation, the parameter ξ was fixed to $\xi = 8\Delta x$. This experiment reveals the values of ε for which the Ewald splitting is necessary. The results are in Figure 4.2, which shows that the computations agree to within machine precision when $\varepsilon \geq 4\Delta x$ or so. Since the splitting parameter ξ plays the role of a regularization parameter, the result also shows that we can choose ξ as small as $\xi = 4\Delta x$ in general, and this provides sufficient smoothness for the FFT
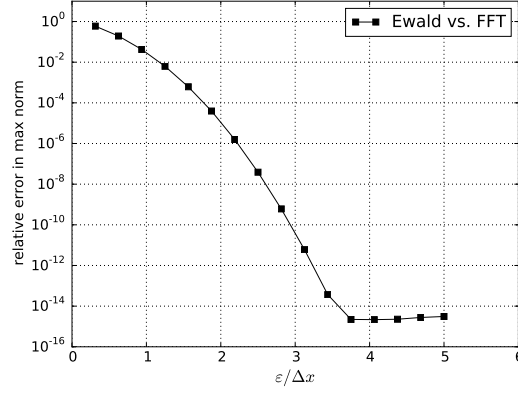
Figure 4.2: Relative maximum error of the unsplit method compared to the split method ($\xi = 8\Delta x$) on a $64 \times 64 \times 64$ grid (i.e. $\Delta x = \frac{1}{64}$). The flow field was generated by 10 random forces at random locations inside the cube $[0, 1]^3$. The two methods are within machine accuracy when $\varepsilon \geq 4\Delta x$, indicating that splitting is not needed when ε is large compared to Δx. *Source:* FFT_Ewald.py.

computation to be spectrally accurate.

Figure 4.2 also shows that when ε is small compared to the grid size Δx, the method without splitting gives solutions that disagree with the Ewald splitting implementation. As ε decreases, the blobs become narrower to the point that they cannot be represented well on the grid, resulting in larger errors. This is verified in Figure 4.3 where the two implementations are compared with the reference solution separately. We see that when ε is large enough, both implementations agree. When ε is small relative to Δx, the errors of the method without splitting are large, while the errors of the method with Ewald splitting remain small. We emphasize that the reference solution is only accurate to within 10^{-6} when the series (3.17) is truncated at $M = 40$. This is why the errors in Figure 4.3 saturate around that value.

Decay of the local sum in an Ewald splitting. In an Ewald splitting, we incorporate periodicity of the local piece in physical space by placing copies of the forces in the main domain in the x and y direction. Since the local piece has fast decay, it contributes to the velocity field only within a certain cutoff radius r_{cutoff}. In order to determine the size of that cutoff radius, we place 10 random forces with zero net force at random locations inside the cube $[0, 1]^3$. We compute the solution
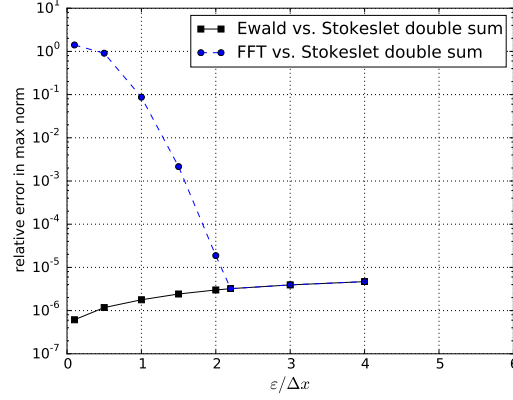
Figure 4.3: Relative maximum error of the velocity field without splitting and with Ewald splitting ($\xi = 4\Delta x$) on a $64 \times 64 \times 10$ grid (i.e. $\Delta x = \frac{1}{64}$). The flow field was generated by 10 random forces with zero net force at random locations inside the cube $[0,1]^3$. For the reference solution we truncated series (3.17) at $M = 40$ yielding an accuracy of about 10^{-6}. *Source:* FFT_Ewald_Real_dat.py (data), FFT_Ewald_Real_fig.py (figure).

cutoff radius	relative error in max norm	
	$\|\mathbf{u}_{\text{split}} - \mathbf{u}_{\text{reference}}\|_\infty$	$\|\mathbf{u}_{\text{split}} - \mathbf{u}_{\text{unsplit}}\|_\infty$
ξ	1.90×10^{-1}	1.90×10^{-1}
2ξ	8.13×10^{-2}	8.13×10^{-2}
4ξ	4.76×10^{-6}	3.05×10^{-6}
6ξ	4.68×10^{-6}	2.34×10^{-14}
8ξ	4.68×10^{-6}	3.64×10^{-15}

Table 4.1: Performance of the split method where the local piece is computed using periodic copies of forces that lie within the cutoff radius of the evaluation point. The parameters used were $\varepsilon = 4\Delta x$ and $\xi = 6\Delta x$. The results are compared to the reference solution (Stokeslet double sum) and the solution produced by only using FFTs. For the reference solution we truncated series (3.17) at $M = 40$ yielding an accuracy of about 10^{-6}. *Source:* local_decay.py.

using the Ewald splitting implementation for different values of r_{cutoff} and compare it to the reference solution. The results from Table 4.1 show that $r_{\text{cutoff}} = 4\xi$ is enough to give us the same accuracy as the reference solution. However, since the accuracy of the reference solution is only about 10^{-6}, we chose the value of the regularization parameter to be $\varepsilon = 4\Delta x$ which is large enough for the FFT method alone (without Ewald splitting) to give accurate results. The last column of Table 4.1 shows the difference between the methods with and without splitting. We find that the two methods agree to within machine precision already for $r_{\text{cutoff}} = 8\xi$.

4.3 Doubly-periodic flow near a wall

The method presented in this section is published in [HC].

We now combine the Ewald splitting from the previous section with the method of images to model the no-slip condition at $z = 0$. Since the image elements are computed directly from the Green's function we computed already, the process is straightforward.

4.3.1 The regular piece

We treat $B(r) \operatorname{erf}\left(\frac{r}{\xi}\right)$ from Eq. (4.1) as a new regularized Green's function corresponding to the new blob (4.2), that is

$$\Psi_\xi^s(r) = \Delta^2 \left(B(r) \operatorname{erf}\left(\frac{r}{\xi}\right)\right) = \frac{1}{\xi^3 \pi^{\frac{3}{2}}} \left(10 - 11\frac{r^2}{\xi^2} + 2\frac{r^4}{\xi^4}\right) \exp\left(-\frac{r^2}{\xi^2}\right).$$

The companion blob is given by

$$\Psi_\xi^d(r) = \frac{1}{\xi^3 \pi^{\frac{3}{2}}} \left(4 - 2\frac{r^2}{\xi^2}\right) \exp\left(-\frac{r^2}{\xi^2}\right).$$

We can now compute the periodic velocity field from Eq. (3.19), with blobs Φ_ε^s and Φ_ε^d replaced by Ψ_ε^s and Ψ_ε^d. We find

$$\hat{\Psi}_\xi^s(\tilde{z}) = \frac{\hat{\delta}_{x_0 y_0}^\xi}{8\xi^5 \sqrt{\pi}} \left[16\tilde{z}^4 - 56\xi^2 \tilde{z}^2 - 8\xi^4\left(-3 + c^2 \tilde{z}^2\right) + 6\xi^6 c^2 + \xi^8 c^4\right] \exp\left(-\frac{\tilde{z}^2}{\xi^2}\right)$$

$$\hat{\Psi}_\xi^d(\tilde{z}) = \frac{\hat{\delta}_{x_0 y_0}^\xi}{2\xi^3 \sqrt{\pi}} \left[-4\tilde{z}^2 + 4\xi^2 + \xi^4 c^2\right] \exp\left(-\frac{\tilde{z}^2}{\xi^2}\right),$$

$\hat{*}_{\Psi_\xi}(\tilde z)$	n	$p_1(\tilde z)$	$p_2(\tilde z)$	$q(\tilde z)$
$\hat{G}_{\Psi_\xi^s}(\tilde z)$	1	-4	-4	$-4 - c^2\xi^2 + 4\frac{\tilde z^2}{\xi^2}$
$\hat{G}'_{\Psi_\xi^s}(\tilde z)$	0	4	-4	$(16 + 2c^2\xi^2)\frac{\tilde z}{\xi} - 8\frac{\tilde z^3}{\xi^3}$
$\hat{B}_{\Psi_\xi^s}(\tilde z)$	3	$2 + 2c\tilde z$	$2 - 2c\tilde z$	$1 + \frac{2}{c^2\xi^2}$
$\hat{B}'_{\Psi_\xi^s}(\tilde z)$	2	$-2c\tilde z$	$-2c\tilde z$	$-2\frac{\tilde z}{\xi}$
$\hat{G}_{\Psi_\xi^d}(\tilde z)$	1	-4	-4	-4
$\hat{G}'_{\Psi_\xi^d}(\tilde z)$	0	4	-4	$8\frac{\tilde z}{\xi}$

$$\hat{*}_{\Psi_\xi}(\tilde z) = \frac{\hat\delta^\xi_{x_0 y_0}}{16 c^n}\exp\left(\frac{c^2\xi^2}{4}\right)\left[p_1(\tilde z)\exp(-c\tilde z)\operatorname{erfc}\left(\frac{c\xi}{2} - \frac{\tilde z}{\xi}\right) + p_2(\tilde z)\exp(c\tilde z)\operatorname{erfc}\left(\frac{c\xi}{2} + \frac{\tilde z}{\xi}\right)\right]$$
$$+ \frac{\hat\delta^\xi_{x_0 y_0}\xi^n}{8\sqrt{\pi}} q(\tilde z)\exp\left(-\frac{\tilde z^2}{\xi^2}\right)$$

Table 4.2: Green's functions in Fourier space for the regular piece when $c \neq 0$.

$\hat{*}_{0,\Psi_\xi}(\tilde z)$	n	$p(\tilde z)$	$q(\tilde z)$
$\hat{G}_{0,\Psi_\xi^s}(\tilde z)$	1	$\tilde z$	$\frac{\tilde z^2}{\xi^2}$
$\hat{G}'_{0,\Psi_\xi^s}(\tilde z)$	0	1	$4\frac{\tilde z}{\xi} - 2\frac{\tilde z^3}{\xi^3}$
$\hat{G}_{0,\Psi_\xi^d}(\tilde z)$	1	$\tilde z$	0
$\hat{G}'_{0,\Psi_\xi^d}(\tilde z)$	0	1	$2\frac{\tilde z}{\xi}$

$$\hat{*}_{0,\Psi_\xi}(\tilde z) = \frac{1}{2}p(\tilde z)\operatorname{erf}\left(\frac{\tilde z}{\xi}\right) + \frac{\xi^n}{2\sqrt{\pi}}q(\tilde z)\exp\left(-\frac{\tilde z^2}{\xi^2}\right)$$

Table 4.3: Green's functions in Fourier space for the regular piece when $c = 0$.

where $\hat\delta^\xi_{x_0 y_0} = \exp(-\frac{1}{4}\xi^2 c^2)\exp(-\frac{2\pi i}{L}(kx_0 + my_0))$. The corresponding Green's functions are given in Tables 4.2 and 4.3 [3] and the velocity computation follows the procedure described in Section 3.2.

4.3.2 The fast-decaying piece

The fast-decaying piece is computed in infinite space where periodicity is accounted for by placing periodic copies of the force $\mathbf{f}_0$ in the x and y direction. When evaluating contributions form the Stokeslet term, one only needs to consider forces within a cutoff radius of 8ξ from the evaluation point (*see* Section 4.2.4). The same cutoff radius can be used for all the other image elements since they decay at least as fast as the

---

[3] *see* Footnote 1

Stokeslet. We can think of the fast-decaying piece as belonging to the difference two blobs

$$\Upsilon^s_{\varepsilon,\xi}(r) = \Phi^s_\varepsilon(r) - \Psi^s_\xi(r)$$
$$= \frac{1}{\pi^{\frac{3}{2}}\varepsilon^3}\left(\frac{5}{2} - \frac{r^2}{\varepsilon^2}\right)\exp\left(-\frac{r^2}{\varepsilon^2}\right) - \frac{1}{\pi^{\frac{3}{2}}\xi^3}\left(10 - 11\frac{r^2}{\xi^2} + 2\frac{r^4}{\xi^4}\right)\exp\left(-\frac{r^2}{\xi^2}\right),$$

which has companion blob

$$\Upsilon^d_{\varepsilon,\xi}(r) = \Phi^d_\varepsilon(r) - \Psi^d_\xi(r) = \frac{1}{\pi^{\frac{3}{2}}\varepsilon^3}\exp\left(-\frac{r^2}{\varepsilon^2}\right) - \frac{1}{\pi^{\frac{3}{2}}\xi^3}\left(4 - 2\frac{r^2}{\xi^2}\right)\exp\left(-\frac{r^2}{\xi^2}\right).$$

Writing the Laplace operator in spherical coordinates (*see* Section 4.2.2) we can solve Eqs. (2.9)-(2.10) with Φ_ε replaced by $\Upsilon^s_{\varepsilon,\xi}$ and $\Upsilon^d_{\varepsilon,\xi}$. The corresponding Green's functions are[4]

$$G_{\Upsilon^s_{\varepsilon,\xi}}(r) = -\frac{1}{4\pi^{\frac{3}{2}}\varepsilon}\exp\left(-\frac{r^2}{\varepsilon^2}\right) + \frac{1}{4\pi^{\frac{3}{2}}\xi}\left(4 - 2\frac{r^2}{\xi^2}\right)\exp\left(-\frac{r^2}{\xi^2}\right) - \frac{1}{4\pi r}\left(\mathrm{erf}\left(\frac{r}{\varepsilon}\right) - \mathrm{erf}\left(\frac{r}{\xi}\right)\right),$$

$$B_{\Upsilon^s_{\varepsilon,\xi}}(r) = -\frac{\varepsilon}{8\pi^{\frac{3}{2}}}\exp\left(-\frac{r^2}{\varepsilon^2}\right) - \frac{r}{8\pi}\left(\mathrm{erf}\left(\frac{r}{\varepsilon}\right) - \mathrm{erf}\left(\frac{r}{\xi}\right)\right),$$

$$G_{\Upsilon^d_{\varepsilon,\xi}}(r) = \frac{1}{2\pi^{\frac{3}{2}}\xi}\exp\left(-\frac{r^2}{\xi^2}\right) - \frac{1}{4\pi r}\left(\mathrm{erf}\left(\frac{r}{\varepsilon}\right) - \mathrm{erf}\left(\frac{r}{\xi}\right)\right),$$

$$B_{\Upsilon^d_{\varepsilon,\xi}}(r) = -\frac{\varepsilon}{8\pi^{\frac{3}{2}}}\exp\left(-\frac{r^2}{\varepsilon^2}\right) + \frac{\xi}{8\pi^{\frac{3}{2}}}\exp\left(-\frac{r^2}{\xi^2}\right)$$
$$+ \frac{1}{16\pi}\left(\left(\frac{\varepsilon^2}{r} + 2r\right)\mathrm{erf}\left(\frac{r}{\varepsilon}\right) - \left(\frac{\xi^2}{r} - 2r\right)\mathrm{erf}\left(\frac{r}{\xi}\right)\right),$$

where we chose the constants of integration so that the Green's functions decay to zero at infinity. The remaining derived functions are given in Table 4.4. The local piece is now computed using Eq. (2.18) with Φ^s_ε and Φ^d_ε replaced by $\Upsilon^s_{\varepsilon,\xi}$ and $\Upsilon^d_{\varepsilon,\xi}$, respectively.

---

[4] *see* Footnote 2

$*\Upsilon_{\varepsilon,\xi}(r)$	n	a_0	a_2	b_0	b_2	b_4	c_0
$H_{1,\Upsilon^s_{\varepsilon,\xi}}(r)$	0	1	0	-3	2	0	1
$H'_{1,\Upsilon^s_{\varepsilon,\xi}}(r)$	1	1	-2	-1	10	-4	-1
$H_{2,\Upsilon^s_{\varepsilon,\xi}}(r)$	2	-1	0	1	-2	0	1
$H'_{2,\Upsilon^s_{\varepsilon,\xi}}(r)$	3	3	2	-3	-2	4	-3
$D_{1,\Upsilon^d_{\varepsilon,\xi}}(r)$	2	2	4	-2	-12	8	-2
$D_{2,\Upsilon^d_{\varepsilon,\xi}}(r)$	4	-6	-4	6	4	-8	6
$G'_{\Upsilon^s_{\varepsilon,\xi}}(r)$	1	-2	2	2	-12	4	2
$G'_{\Upsilon^d_{\varepsilon,\xi}}(r)$	1	-2	0	2	-4	0	2

$$*\Upsilon_{\varepsilon,\xi}(r) = \frac{1}{4\pi^{\frac{3}{2}}r^n}\left[\frac{1}{\varepsilon}\left(a_0 + a_2\frac{r^2}{\varepsilon^2}\right)\exp\left(-\frac{r^2}{\varepsilon^2}\right) + \frac{1}{\xi}\left(b_0 + b_2\frac{r^2}{\xi^2} + b_4\frac{r^4}{\xi^4}\right)\exp\left(-\frac{r^2}{\xi^2}\right)\right]$$
$$+ \frac{c_0}{4\pi r^{n+1}}\left[\mathrm{erf}\left(\frac{r}{\varepsilon}\right) - \mathrm{erf}\left(\frac{r}{\xi}\right)\right]$$

Table 4.4: Derived functions in real space for the local piece.

4.3.3   Summary of the method

The doubly-periodic Stokeslet near a planar wall using FFTs and Ewald splitting

Consider a *regularized* point force with strength $\mathbf{f}_0$ centered at $\mathbf{x}_0$ and distributed periodically in x and y with periods L_x and L_y. The doubly-periodic fluid velocity $\mathbf{u}$ that satisfies the no-slip condition $\mathbf{u}|_{z=0} = \mathbf{0}$ can be found by performing the following algorithm. The algorithm finds $\mathbf{u}$ on an (x,y) grid for fixed z (see also Figure 3.1). The fluid velocity can be interpolated to an arbitrary point $\mathbf{x}$ if needed.

1. Evaluate the regular part of the velocity field $\hat{\mathbf{u}}_{\mathrm{reg}}$ on a grid of wave numbers (k,m) using Eq. (3.19) with Φ^s_ε and Φ^d_ε replaced by Ψ^s_ξ and Ψ^d_ξ, where $\xi = 4\Delta x$.

   - For $(k,m) \neq \mathbf{0}$ the image elements are defined in Eqs. (3.6), (3.20)-(3.22) and the corresponding Green's functions are defined in Table 4.2.

   - For $(k,m) = \mathbf{0}$ the image elements are defined in Eqs. (3.23)-(3.26) and the corresponding Green's functions are defined in Table 4.3.

   Then find $\mathbf{u}_{\mathrm{reg}}$ on the grid by taking an inverse FFT according to Eq. (3.1).

2. Find the local part of the velocity field $\mathbf{u}_{\mathrm{loc}}$ by computing Eq. (2.21) with Φ^s_ε and Φ^d_ε replaced by $\Upsilon^s_{\varepsilon,\xi}$ and $\Upsilon^d_{\varepsilon,\xi}$. The image elements are given

> ### The doubly-periodic Stokeslet near a planar wall using FFTs and Ewald splitting (Continued)
>
> in Eqs. (2.12), (2.22), (2.23) and (2.24) and the corresponding Green's functions are defined in Table 4.4. In order to find the velocity at a grid point, only forces within radius $r_{\text{cutoff}} = 8\xi$ need to be considered but it may be necessary to place periodic copies of $\mathbf{f}_0$ in x and y.
>
> 3. Compute $\mathbf{u} = \mathbf{u}_{\text{loc}} + \mathbf{u}_{\text{reg}}$.
>
> *Note:* If $\varepsilon \geq 4\Delta x$, splitting is not needed and the method from Section 3.2.2 should be used instead.

Chapter 5

Arrays of nodal cilia

The results presented in this chapter are published in [HC].

We use our numerical method described in the previous two chapters to model carpets of nodal cilia. A *nodal cilium* describes a conical rotation that is defined by the half-cone angle ψ and the tilt angle θ, which we define as the angle by which the centerline of the cone is rotated about the x-axis (see Figure 5.1). The conical motion creates fluid mixing below the tip of the cilium and fluid advection above the cilium [dTO13] for nonzero tilt angle. The fluid advection is in the direction of the cilium motion when the cilium is the most upright as the cilium drags less fluid with it the closer it is to the wall. If the tilt angle is zero, the motion of the cilium does not have a preferred direction and therefore no net fluid transport occurs in Stokes flow. In nature nodal cilia are responsible for left-right asymmetry in vertebrae development [MN06]. Our focus, however, is on artificial nodal cilia, which were proven experimentally to create fluid mixing [CCLH13] and transport [VPK+10, SFE+10, WGW+13, WGW+14] when actuated by an external magnetic field. Synthetic cilia following different beat patterns have been shown experimentally to create fluid transport as well. Chen et al. experimented with different trajectories including circular rotation, linear back
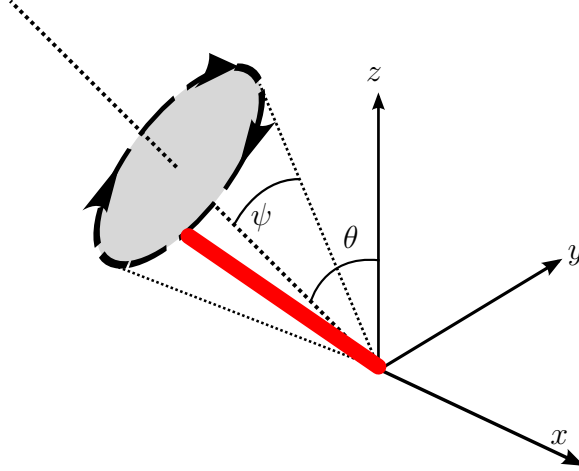
Figure 5.1: Schematic of a nodal cilium. The described motion creates a net flow above the cilium in the direction of the positive x-axis.

and forward motion and a setting where the tip of the cilium describes a figure eight [CCLH13]. Keißner and Brücker tested a mechanical actuation mechanism, where stiff cilia are placed on a flexible surface that is deformed from underneath by a moving ball chain [KB12]. In this case the fluid transport is due to the viscous coupling of neighboring cilia. Hussong et al. used rectangular shaped cilia that perform a planar effective stroke in a rotating magnet field and whose recovery stroke is forced by the cilia curling up due to their stiffness [HSB$^+$11].

The motivation for focusing on two-dimensional periodicity is to avoid the computational cost associated with computing large numbers of individual cilia. Instead we use only a few cilia, for instance comprising one metachronal wave length, and place them inside a doubly-periodic box. This allows us to accurately resolve the flow close to the cilium while at the same time incorporating large-scale effects of the ciliary carpet. An early approach to model large-scale effects of ciliary carpets is Blake's envelope model, that views the tips of densely packed cilia as a continuum (envelope) [Bla71b]. This model was not intended to resolve the region below the cilia tips, which is, for instance, crucial for fluid mixing. Liron and Mochon average the velocity field in one spatial direction [LM75], which allows for better resolution

than the envelope model although the flow field is not fully three dimensional. Some methods model ciliary arrays by computing large numbers of individual cilia. The fluid flow is then analyzed in the middle section of the computational domain in order to avoid edge effects. Smith et al. [SGB07, SBG08] and Ding et al. [DNMNK14] represent cilia by a Stokeslet distribution where the point forces exerted by the cilium are found from a prescribed cilium shape. In this approach the forces are the solution of a linear system, the size of which is proportional to the total number of cilia and the number of point forces per cilium. The system can, therefore, be quite large especially for two-dimensional arrays. Gueron et al. assume more flexible beat patterns that change based on multi-cilia interactions and internal mechanisms of cilia and compute one and two-dimensional arrays of cilia [GLGLB97, GLG99, GLG98]. They note, however, that some wavelike patterns that require more rows could not be computed due to the prohibitive computational cost [GLG98].

5.1 Numerical results

We represent the exerted force along the cilium by N_{forces} equally spaced point forces. Defining the half-cone angle ψ and the tilt angle θ as in Figure 5.1, the parametric equation of the motion of a nodal cilium is given by

$$
\mathbf{x}(s,t) = \begin{pmatrix} 1 & 0 & 0 \\ 0 & \cos(\theta) & \sin(\theta) \\ 0 & -\sin(\theta) & \cos(\theta) \end{pmatrix} \begin{pmatrix} \cos(\frac{2\pi t}{T})\sin(\psi)s \\ \sin(\frac{2\pi t}{T})\sin(\psi)s \\ \cos(\psi)s \end{pmatrix},
$$

where $(s,t) \in [0,\mathcal{L}] \times [0,T]$, where $\mathcal{L}$ is the length of the cilium and T is the time for one full rotation. In our model we assume that the cilia are straight and that no deformation occurs. The velocity of the cilium can be obtained by simply differentiating the parametric equation. Since the relationship between velocity and force

is linear under Stokes equation, we can set up a linear system whose solution gives the correct forces from the prescribed cilium velocities. The computed point forces can then be used to find the fluid velocity at arbitrary points in the computational domain.

For all experiments we fix $\mu = 1$, $\mathcal{L} = 1$ and $T = 1$, and use grid spacing $\Delta x = \Delta y = 1/64$ and time step $\Delta t = 1/64$. The regularization parameter ε is chosen on the order of the thickness of the cilium [CN12]. We use $\varepsilon = 0.05$, which reproduces the slenderness ratio of magnetic artificial cilia of about 5-20 [VPK+10, WGW+13]. This choice was also made in [DNMNK14] for pulmonary cilia. For a given choice of ε, the cilium discretization must be chosen so that no fluid crosses the cilium as it moves, which can happen if the point forces on the cilium are too far apart. At the force locations the cilium velocity is enforced exactly so we compute by how much the computed velocity along the cilium deviates from the exact velocity between the point forces. For a nodal cilium with $\theta = 0°$ and $\psi = 30°$ we find the maximal leakage is $4.9 \cdot 10^{-2}$ for $N_{\text{forces}} = 16$, $2.5 \cdot 10^{-3}$ for $N_{\text{forces}} = 32$ and $3.3 \cdot 10^{-6}$ for $N_{\text{forces}} = 64$. Subsequently we use $N_{\text{forces}} = 64$.

5.1.1 Fluid flow at different heights

At first we compute one cilium in a doubly-periodic box with $\theta = 20°$ and $\psi = 20°$. We track massless tracer particles placed at different initial heights and denote by $\mathbf{x}(t)$ the position of a tracer particle at time t. For every tracer particle we compute the net flow $(\mathbf{x}(T) - \mathbf{x}(0))/T$, which is the effective advection per rotation. Figure 5.2 shows that below the tip of the cilium there is considerable net flow in all directions, which is an indication of fluid mixing. Above the tip of the cilium we observe a nearly uniform nonzero net flow (compare also to [OV11]) in x that is consistent with the

net flow based on Eq. (3.27)

$$\mathbf{u}_{\text{net}} = \frac{1}{\mu L_x L_y T} \int_{t=0}^{T} \sum_{k=1}^{N_{\text{forces}}} z_0^k(t) \begin{pmatrix} f_1^k(t) \\ f_2^k(t) \\ 0. \end{pmatrix} dt, \tag{5.1}$$

where $z_0^k(t)$ is the z-component of the kth force, which has strength $(f_1^k(t), f_2^k(t), 0)$. In this example we find $\mathbf{u}_{\text{net}} = (4.06 \cdot 10^{-2}, 3.47 \cdot 10^{-18}, 0)$. There is no net flow above the cilium in y because the cilium motion is symmetric in y. The fluid velocity at the wall is on the order of machine accuracy in all spatial directions. We note that the introduction of a top wall can lead to more complex flow patterns where there is a flow in the opposite direction near the top wall [SFE+10].

5.1.2 Optimal advection angles

Next we are interested in the optimal tilt and half-cone angle for fluid advection. Theoretical results based on resistive force theory along with numerical results for arrays of cilia suggest that the optimal angles are $\theta + \psi \sim 90°$ and $\theta \sim 35°$ [SBG08, DS09]. Even though in the referenced model, cilia were arranged not in a rectangular but in a triangular shape, we were able to produce similar results by using only one cilium in a doubly-periodic box (see Figure 5.3). The figure shows that the net flow increases as $\theta + \psi$ approaches 90° and is largest when $\psi \approx 55°$. Our results are also consistent with experimental results also referenced in [SBG08].

5.1.3 Effects of cilia density

We explore how cilia density influences fluid advection. We place one cilium in a doubly-periodic quadratic box and vary the size of the box keeping $L_x = L_y$ (see Figure 5.4(a)). The net flow increases as density increases, which may be intuitively

(a)

(b)

(c)
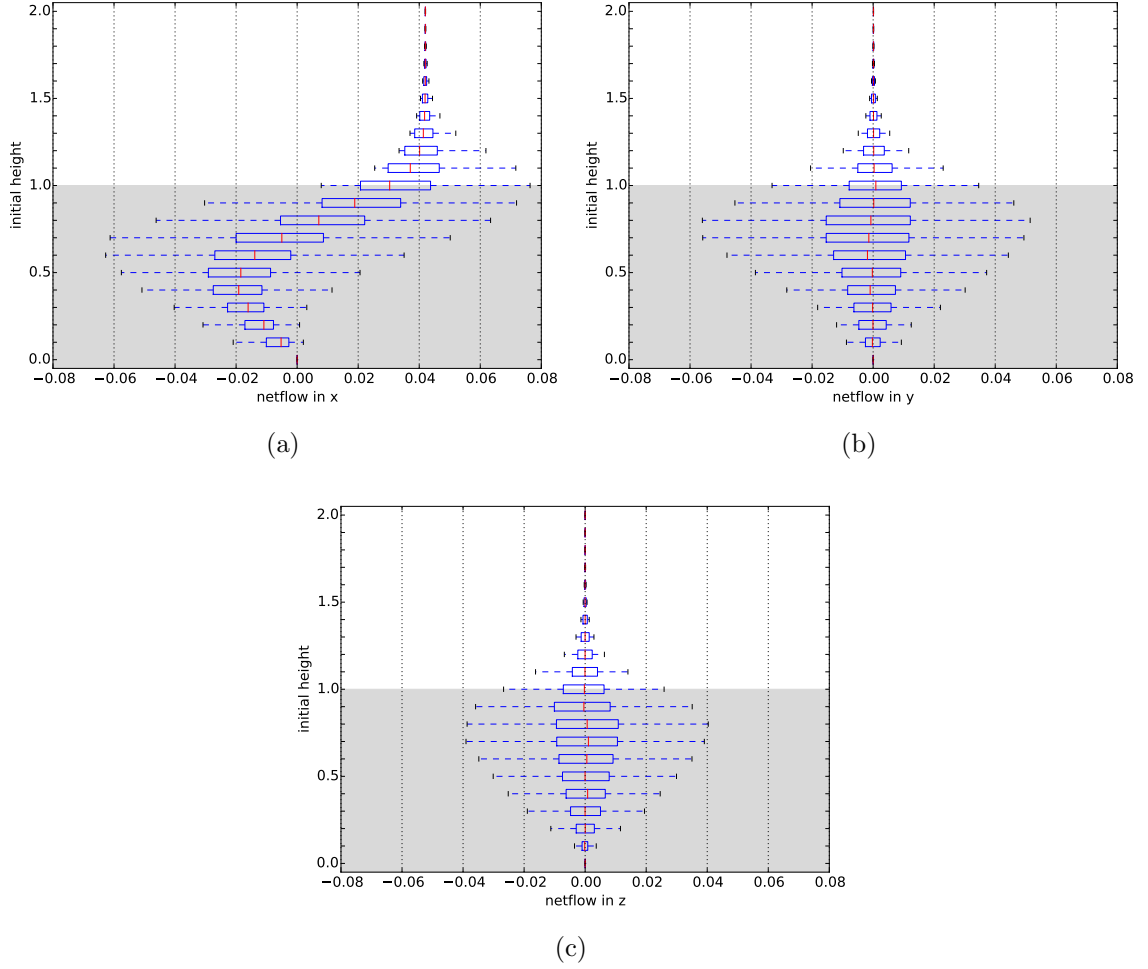
Figure 5.2: Displacement of tracer particles placed uniformly at different initial heights after one rotation of the nodal cilium ($\theta = 20°$, $\psi = 20°$, $\mathcal{L} = 1$, $L_x = 1.0$, $L_y = 1.0$). In the box plots, the box marks the inner quartile range and the whiskers extend to the most extreme data point within 1.5 times the inner quartile range. There is net flow in all directions below the tip of the cilium (gray region) indicative of mixing and there is a net flow in x above the tip of the cilium consistent with $\mathbf{u}_{\text{net}}$ computed form Eq. (5.1). *Source:* nodal_velo_at_z_layers.py.
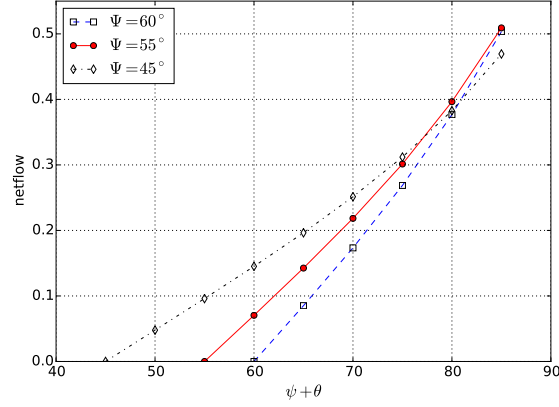
Figure 5.3: Net flow after one rotation of the cilium as computed from Eq. (5.1) for varying tilt angle θ and half-cone angle ψ ($\mathcal{L} = 1$, $L_x = 1.0$, $L_y = 1.0$). We required $\psi + \theta < 85°$ for numerical accuracy. Resistive force theory suggests optimal advection for $\theta + \psi \sim 90°$ and $\theta \sim 35°$ [SBG08]. *Source:* nodal_optimal_angle_dat.py (data), nodal_optimal_angle_fig.py (figure).

expected or inferred from the coefficient in Eq. (5.1). However, the relationship between net flow and $1/(L_x L_y)$ is not linear; the net flow approaches a maximum value. This is because the force term in Eq. (5.1), which is the force required to maintain a prescribed velocity, decreases significantly with an increase in cilia density (Figure 5.4(b)).
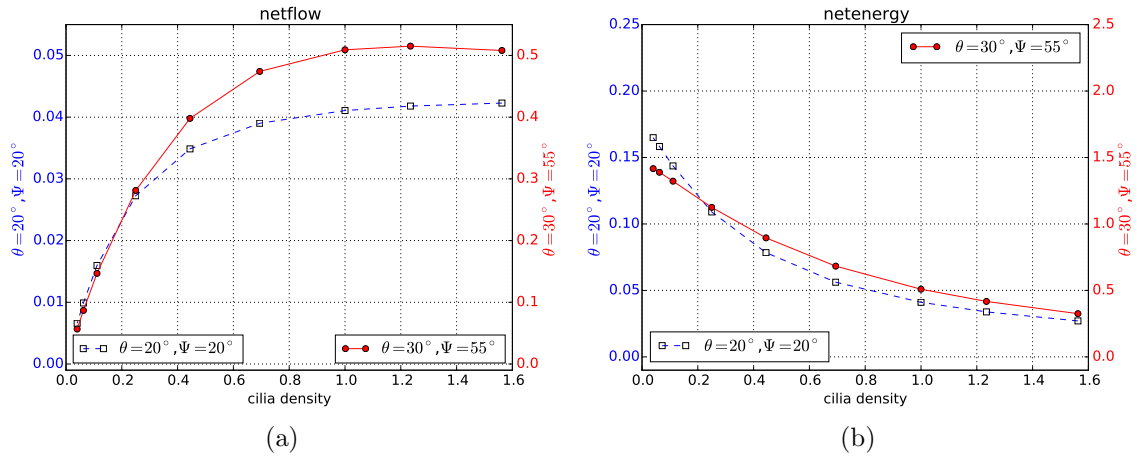
Figure 5.4: Net flow $\mathbf{u}_{\mathrm{net}}$ and net energy $\mu L_x L_y \mathbf{u}_{\mathrm{net}}$ for varying cilia density, which is defined as the number of cilia per unit area. In practice we model one cilium per quadratic box $L_x = L_y$ ($\mathcal{L} = 1$) so that, for instance, the periodic box $[0,2] \times [0,2]$ corresponds to a density of 0.25. The net flow increases with increasing density as the coefficient in Eq. (5.1) suggests but the decrease in net energy shows that the forces in Eq. (5.1) change significantly based on density as well. *Source:* nodal_vary_density_dat.py (data), nodal_vary_density_fig.py (figure).

Chapter 6

Conclusions

We have presented a method for computing doubly-periodic Stokes flow driven by regularized forces in three dimensions. In the non-periodic direction we enforce a no-slip condition at an infinite planar wall or assume a free boundary. As most computations are done analytically, in practice one only needs to evaluate the given expressions of the velocity field on a regular two-dimensional grid and compute an inverse FFT. As we use regularized forces, there are no singularities in the flow.

Ewald splitting is not needed when the regularization parameter ε is large enough compared to the grid size Δx. If Ewald splitting is used in the case where ε is small compared to Δx, there are two advantages. One advantage is that the spectral sum is replaced by an FFT on a grid, which guarantees fast computation. Another advantage is that the FFT allows for the splitting parameter to be chosen as small as $\xi = 4\Delta x$. This makes the sum in physical space converge extremely fast. Therefore, even if the total number of forces N is large, the local velocity contribution to a particular grid point need only include the forces in a relatively small neighborhood (within a few ξ) of the grid point.

We have also shown how our method can be used to compute the flow created by carpets of nodal cilia, where only the shapes of the cilia are provided. Further we

have derived an exact expression for the velocity sufficiently high above the tips of the cilia.

6.1   Future work

The following list contains some possible extensions of our work.

- *Brinkman flow.* Fluid flow in porous media can be described by Brinkman's equation [CCLV10]

$$\alpha^2 \mathbf{u} = -\nabla p + \frac{1}{\phi} \Delta \mathbf{u} + \mathbf{F},$$

  where again p is pressure, $\mathbf{u}$ is the fluid velocity and $\mathbf{F}$ is force. The parameters α and ϕ are dimensionless and range between 0 and 1. Setting $\alpha = 0$ we recover Stokes equation, which models the flow in a medium with large pores and high permeability. Similar to our treatment of Stokes equation we can rewrite Brinkman's equation in Fourier space, which yields a system of ODEs fairly similar to the one corresponding to Stokes equation. Solving that system for the doubly-periodic velocity field should be analogous.

- *Inner cilia mechanisms.* In our method we solve for the forces exerted by the cilia from a prescribed motion, which in the case of stiff nodal cilia is known exactly. The exact shapes of biological cilia are more complex and the result of inner cilia mechanisms and multi-ciliary interactions. The latter aspect is of particular importance in the emergence of metachrony [EG13]. It would be straightforward to couple our fluid solver with a method that finds the force along the cilium from inner ciliary mechanisms [LL10] and to incorporate a feedback mechanisms accounting for multi-ciliary interactions.

- *Non-Newtonian fluids.* One of the most important functions of biological cilia

is the transport of mucus in the human lungs and sinuses [MN06, FB86]. As mucus is a non-Newtonian fluid, in this context it is crucial to extend our model to include viscoelastic properties of the mucus layer [WCF14].

Appendix A

Singular Green's functions

A.1   Derivation of the singular Green's function in free space

Our goal is to find the fundamental solution or Green's function G to Laplace's equation

$$\Delta G\left(\mathbf{x}\right) = \delta\left(\mathbf{x} - \mathbf{x}_0\right),$$

where δ is the Dirac delta function. We further demand that G decays to 0 at infinity. We present a proof based on lecture notes from a class taught by Xuefeng Wang[1] for the three-dimensional case. Since the delta function is radially symmetric, we seek a radially symmetric solution $G(r)$, where $r = |\mathbf{x} - \mathbf{x}_0|$. For $r > 0$, writing Laplace's equation in spherical coordinates

$$\Delta G = \frac{1}{r^2}\frac{\partial}{\partial r}\left(r^2\frac{\partial}{\partial r}\right)G(r) = 0,$$

---

[1] Xuefeng Wang, MATH 7530-Partial Differential Equations, Fall 2011, Tulane University.

we find $G(r) = C/r$. In order to determine the constant C we use the regularized Green's function $G_\varepsilon(r) := C/\sqrt{r^2 + \varepsilon^2}$ to give

$$\int_{\mathbb{R}^3} \Delta G_\varepsilon(\mathbf{x}) d\mathbf{x} = -3C \int_{|\boldsymbol{\sigma}|=1} \int_0^\infty \frac{\varepsilon^2}{(r^2 + \varepsilon^2)^{\frac{5}{2}}} \cdot r^2 dr d\boldsymbol{\sigma}$$

$$= -3C \left| \partial B_1(0) \right| \int_0^{\frac{\pi}{2}} \frac{\tan^2(\alpha) \left(1 + \tan^2(\alpha)\right)}{\left(1 + \tan^2(\alpha)\right)^{\frac{5}{2}}} d\alpha$$

$$= -12\pi C \int_0^{\frac{\pi}{2}} \sin^2(\alpha) \cos(\alpha) d\alpha$$

$$= -4\pi C,$$

where we used the substitution $r = \varepsilon \tan(\alpha)$. The quantity $\left| \partial B_1(0) \right|$ is the surface area of the unit ball in three dimensions. Letting $\varepsilon \to 0$ gives

$$1 = -4\pi C,$$

and ultimately $G(r) = -1/4\pi r$. We note that without specifying boundary conditions for the Green's function G is unique only up to a harmonic function but requiring $G \to 0$ as $r \to \infty$ ensures uniqueness. It is now an easy exercise to show that

$$\Delta B(r) = \frac{1}{r^2} \frac{\partial}{\partial r} \left(r^2 \frac{\partial}{\partial r} \right) B(r) = G(r),$$

implies $B(r) = -r/8\pi$, where we have set the constants of integration to 0.

A.2 A different representation of the Stokeslet

Using *Einstein summation notation*[2] and defining $r = |\tilde{\mathbf{x}}|$ we find

$$
\begin{aligned}
\mathbf{St}_{\mathbf{f}_0}(\tilde{\mathbf{x}}) &= (\mathbf{f}_0 \cdot \nabla) \nabla B(r) - \mathbf{f}_0 G(r) \\
&= \left(\frac{\partial}{\partial x_j} \frac{\partial}{\partial x_i} B(r) - G(r)\delta_{ij} \right) f_j \\
&= \left(\frac{\partial}{\partial x_j} \frac{B'(r)}{r} \tilde{x}_i - G(r)\delta_{ij} \right) f_j \\
&= \left(\left(\frac{B(r)'}{r} - G(r) \right) \delta_{ij} + \frac{1}{r} \left(\frac{B'(r)}{r} \right)' \tilde{x}_i \tilde{x}_j \right) f_j. \\
&= \left(\frac{B(r)'}{r} - G(r) \right) \mathbf{f}_0 + \frac{1}{r} \left(\frac{B'(r)}{r} \right)' (\mathbf{f}_0 \cdot \tilde{\mathbf{x}}) \tilde{\mathbf{x}}.
\end{aligned}
$$

A.3 Derivation of the singular Green's function in Fourier space

We want to solve the boundary value problem

$$
\hat{G}''(z) - c^2 \hat{G}(z) = \hat{\delta}_{x_0 y_0} \delta(z - z_0)
$$

$$
\lim_{z \to \pm\infty} \hat{G}(z) = 0,
$$

where the function $\hat{G}$ is at least twice continuously differentiable on $(-\infty, z_0) \cup (z_0, \infty)$. Two linearly independent solutions to the homogeneous equation

$$
\hat{G}''(z) - c^2 \hat{G}(z) = 0,
$$

that also satisfy the boundary condition at infinity are given by

$$u_1(z) = \begin{cases} e^{cz} & z < z_0 \\ 0 & z > z_0, \end{cases} \qquad u_2(z) = \begin{cases} 0 & z < z_0 \\ e^{-cz} & z > z_0. \end{cases}$$

In the method *variation of parameters* we seek a solution $\hat{G}(z) = A_1(z)u_1(z) + A_2(z)u_2(z)$ to the inhomogeneous equation, where $A_1'(z)u_1(z) + A_2'(z)u_2(z) = 0$. This gives rise to the system

$$\underbrace{\begin{pmatrix} u_1(z) & u_2(z) \\ u_1'(z) & u_2'(z) \end{pmatrix}}_{W} \begin{pmatrix} A_1'(z) \\ A_2'(z) \end{pmatrix} = \begin{pmatrix} 0 \\ \hat{\delta}_{x_0 y_0} \delta(z - z_0) \end{pmatrix},$$

where W is the so-called *Wronskian*. It follows that

$$A_1'(z) = -\frac{\hat{\delta}_{x_0 y_0}}{\det(W)} u_2(z) \delta(z - z_0),$$

$$A_2'(z) = \frac{\hat{\delta}_{x_0 y_0}}{\det(W)} u_1(z) \delta(z - z_0),$$

where $\det(W) = -2c$. Thus the functions $A_1(z)$ and $A_2(z)$ are Heaviside step functions with the appropriate jump, that is

$$A_1(z) = -\frac{\hat{\delta}_{x_0 y_0}}{2c} \begin{cases} e^{-cz_0} & z < z_0 \\ 0 & z > z_0, \end{cases}$$

$$A_2(z) = -\frac{\hat{\delta}_{x_0 y_0}}{2c} \begin{cases} 0 & z < z_0 \\ e^{cz_0} & z > z_0. \end{cases}$$

Therefore

$$\hat{G}(z) = A_1(z)u_1(z) + A_2(z)u_2(z) = -\frac{\hat{\delta}_{x_0 y_0}}{2c} e^{-c|z - z_0|}.$$

The function $\hat{B}$ can be obtained analogously.

Appendix B

The Stokeslet double sum

B.1 Convergence of the Stokeslet double sum

Proof of Theorem 3.1.3. Without loss of generality we assume $L_x = L_y = 1$. The infinite Stokeslet double sum is defined as the limit of the partial sums

$$\sum_{n,m=-\infty}^{\infty} \sum_{k=1}^{K} \frac{\mathbf{f}_k}{|\mathbf{x} - \mathbf{x}_k - \mathbf{n}|} + \frac{[\mathbf{f}_k \cdot (\mathbf{x} - \mathbf{x}_k - \mathbf{n})] (\mathbf{x} - \mathbf{x}_k - \mathbf{n})}{|\mathbf{x} - \mathbf{x}_k - \mathbf{n}|^3}$$

$$= \lim_{N \to \infty} \left(\underbrace{\sum_{m=-N}^{N} \sum_{n=-N}^{N} \sum_{k=1}^{K} \frac{\mathbf{f}_k}{|\mathbf{x} - \mathbf{x}_k - \mathbf{n}|}}_{S_A} + \underbrace{\sum_{m=-N}^{N} \sum_{n=-N}^{N} \sum_{k=1}^{K} \frac{[\mathbf{f}_k \cdot (\mathbf{x} - \mathbf{x}_k - \mathbf{n})] (\mathbf{x} - \mathbf{x}_k - \mathbf{n})}{|\mathbf{x} - \mathbf{x}_k - \mathbf{n}|^3}}_{S_B} \right),$$

(B.1)

where $\mathbf{n} = (n, m, 0)$. We define the normalized vector $\hat{\mathbf{n}} = \mathbf{n}/|\mathbf{n}|$.

(i) *Expansion of S_A.* Expanding the denominator we can write

$$|(\mathbf{x} - \mathbf{x}_k) - \mathbf{n}|^2 = [(\mathbf{x} - \mathbf{x}_k) - \mathbf{n}] \cdot [(\mathbf{x} - \mathbf{x}_k) - \mathbf{n}]$$

$$= \underbrace{|\mathbf{x} - \mathbf{x}_k|^2}_{=:D_k} \underbrace{-2 [(\mathbf{x} - \mathbf{x}_k) \cdot \hat{\mathbf{n}}]}_{=:E_{k,\hat{\mathbf{n}}}} |\mathbf{n}| + |\mathbf{n}|^2.$$

Using an asymptotic expansion of the summand in powers of $|\mathbf{n}|$ at ∞ gives

$$
\begin{aligned}
S_A &= \sum_{m=-N}^{N} \sum_{n=-N}^{N} \sum_{k=1}^{K} \frac{\mathbf{f}_k}{\left(D_k + E_{k,\hat{\mathbf{n}}} |\mathbf{n}| + |\mathbf{n}|^2\right)^{\frac{1}{2}}} \\
&= \sum_{m=-N}^{N} \sum_{n=-N}^{N} \sum_{k=1}^{K} \mathbf{f}_k \left(\frac{1}{|\mathbf{n}|} + \frac{-E_{k,\hat{\mathbf{n}}}}{2 |\mathbf{n}|^2} + \frac{-4D_k + 3E_{k,\hat{\mathbf{n}}}^2}{8 |\mathbf{n}|^3} + \frac{12 D_k E_{k,\hat{\mathbf{n}}}}{16 |\mathbf{n}|^4} + \mathcal{O}\left(\frac{1}{|\mathbf{n}|^5} \right) \right) \\
&= \sum_{m=-N}^{N} \sum_{n=-N}^{N} \sum_{k=1}^{K} \mathbf{f}_k \left(\frac{1}{|\mathbf{n}|} + \frac{-4D_k + 3E_{k,\hat{\mathbf{n}}}^2}{8 |\mathbf{n}|^3} + \mathcal{O}\left(\frac{1}{|\mathbf{n}|^5} \right) \right),
\end{aligned}
\tag{B.2}
$$

where we have used that

$$
0 = \sum_{m=-N}^{N} \sum_{n=-N}^{N} \frac{-E_{k,\hat{\mathbf{n}}}}{2 |\mathbf{n}|^2}
$$

$$
0 = \sum_{m=-N}^{N} \sum_{n=-N}^{N} \frac{12 D_k E_{k,\hat{\mathbf{n}}}}{16 |\mathbf{n}|^4},
$$

because of symmetry.

(ii) *Expansion of S_B.* We find

$$
\begin{aligned}
\left[\mathbf{f}_k \cdot \left((\mathbf{x} - \mathbf{x}_k) - \mathbf{n}\right)\right] \left((\mathbf{x} - \mathbf{x}_k) - \mathbf{n}\right) &= \left[\mathbf{f}_k \cdot (\mathbf{x} - \mathbf{x}_k) - \mathbf{f}_k \cdot \mathbf{n}\right] \left[(\mathbf{x} - \mathbf{x}_k) - \mathbf{n}\right] \\
&= \underbrace{\left[\mathbf{f}_k \cdot (\mathbf{x} - \mathbf{x}_k)\right] (\mathbf{x} - \mathbf{x}_k)}_{=: \mathbf{A}_k} \\
&\quad \underbrace{- \left(\left[\mathbf{f}_k \cdot (\mathbf{x} - \mathbf{x}_k)\right] \hat{\mathbf{n}} + \left[\mathbf{f}_k \cdot \hat{\mathbf{n}}\right] (\mathbf{x} - \mathbf{x}_k)\right)}_{=: \mathbf{B}_{k,\hat{\mathbf{n}}}} |\mathbf{n}| \\
&\quad + \underbrace{\left[\mathbf{f}_k \cdot \hat{\mathbf{n}}\right] \hat{\mathbf{n}}}_{=: \mathbf{C}_{k,\hat{\mathbf{n}}}} |\mathbf{n}|^2.
\end{aligned}
$$

Again using an asymptotic expansion of the summand in powers of $|\mathbf{n}|$ at ∞

gives

$$
\begin{aligned}
S_B &= \sum_{m=-N}^{N} \sum_{n=-N}^{N} \sum_{k=1}^{K} \frac{\mathbf{A}_k + \mathbf{B}_{k,\hat{\mathbf{n}}} |\mathbf{n}| + \mathbf{C}_{k,\hat{\mathbf{n}}} |\mathbf{n}|^2}{\left(D_k + E_{k,\hat{\mathbf{n}}} |\mathbf{n}| + |\mathbf{n}|^2\right)^{\frac{3}{2}}} \\
&= \sum_{m=-N}^{N} \sum_{n=-N}^{N} \sum_{k=1}^{K} \left(\frac{\mathbf{C}_{k,\hat{\mathbf{n}}}}{|\mathbf{n}|} + \frac{2\mathbf{B}_{k,\hat{\mathbf{n}}} - 3E_{k,\hat{\mathbf{n}}}\mathbf{C}_{k,\hat{\mathbf{n}}}}{2 |\mathbf{n}|^2} \right. \\
&\qquad + \frac{8\mathbf{A}_k - 12D_k\mathbf{C}_{k,\hat{\mathbf{n}}} - 12E_{k,\hat{\mathbf{n}}}\mathbf{B}_{k,\hat{\mathbf{n}}} + 15E_{k,\hat{\mathbf{n}}}^2\mathbf{C}_{k,\hat{\mathbf{n}}}}{8 |\mathbf{n}|^3} \\
&\qquad + \frac{-24D_k\mathbf{B}_{k,\hat{\mathbf{n}}} - 24E_{k,\hat{\mathbf{n}}}\mathbf{A}_k + 60D_kE_{k,\hat{\mathbf{n}}}\mathbf{C}_{k,\hat{\mathbf{n}}} + 30E_{k,\hat{\mathbf{n}}}^2\mathbf{B}_{k,\hat{\mathbf{n}}} - 35E_{k,\hat{\mathbf{n}}}^3\mathbf{C}_{k,\hat{\mathbf{n}}}}{16 |\mathbf{n}|^4} \\
&\qquad \left. + \mathcal{O}\left(\frac{1}{|\mathbf{n}|^5}\right) \right) \\
&= \sum_{m=-N}^{N} \sum_{n=-N}^{N} \sum_{k=1}^{K} \left(\frac{\mathbf{C}_{k,\hat{\mathbf{n}}}}{|\mathbf{n}|} + \frac{8\mathbf{A}_k - 12D_k\mathbf{C}_{k,\hat{\mathbf{n}}} - 12E_{k,\hat{\mathbf{n}}}\mathbf{B}_{k,\hat{\mathbf{n}}} + 15E_{k,\hat{\mathbf{n}}}^2\mathbf{C}_{k,\hat{\mathbf{n}}}}{8 |\mathbf{n}|^3} + \mathcal{O}\left(\frac{1}{|\mathbf{n}|^5}\right) \right),
\end{aligned}
\tag{B.3}
$$

where we have used that

$$
0 = \sum_{m=-N}^{N} \sum_{n=-N}^{N} \frac{2\mathbf{B}_{k,\hat{\mathbf{n}}} - 3E_{k,\hat{\mathbf{n}}}\mathbf{C}_{k,\hat{\mathbf{n}}}}{2 |\mathbf{n}|^2}
$$

$$
0 = \sum_{m=-N}^{N} \sum_{n=-N}^{N} \frac{-24D_k\mathbf{B}_{k,\hat{\mathbf{n}}} - 24E_{k,\hat{\mathbf{n}}}\mathbf{A}_k + 60D_kE_{k,\hat{\mathbf{n}}}\mathbf{C}_{k,\hat{\mathbf{n}}} + 30E_{k,\hat{\mathbf{n}}}^2\mathbf{B}_{k,\hat{\mathbf{n}}} - 35E_{k,\hat{\mathbf{n}}}^3\mathbf{C}_{k,\hat{\mathbf{n}}}}{16 |\mathbf{n}|^4},
$$

because of symmetry[1]. The leading order term can be written as

$$\sum_{m=-N}^{N}\sum_{n=-N}^{N}\sum_{k=1}^{K}\frac{\mathbf{C}_{k,\hat{\mathbf{n}}}}{|\mathbf{n}|} = \sum_{m=-N}^{N}\sum_{n=-N}^{N}\sum_{k=1}^{K}\frac{1}{|\mathbf{n}|}\left[\mathbf{f}_k\cdot\hat{\mathbf{n}}\right]\hat{\mathbf{n}}$$

$$= \sum_{m=-N}^{N}\sum_{n=-N}^{N}\sum_{k=1}^{K}\frac{1}{|\mathbf{n}|^3}\left[\begin{pmatrix}f_k^{(1)}\\f_k^{(2)}\\f_k^{(3)}\end{pmatrix}\cdot\begin{pmatrix}n\\m\\0\end{pmatrix}\right]\begin{pmatrix}n\\m\\0\end{pmatrix}$$

$$= \sum_{m=-N}^{N}\sum_{n=-N}^{N}\sum_{k=1}^{K}\frac{1}{|\mathbf{n}|^3}\begin{pmatrix}f_k^{(1)}n^2 + f_k^{(2)}nm\\f_k^{(2)}m^2 + f_k^{(1)}nm\\0\end{pmatrix}$$

$$= \sum_{m=-N}^{N}\sum_{n=-N}^{N}\sum_{k=1}^{K}\frac{1}{(n^2+m^2)^{\frac{3}{2}}}\begin{pmatrix}f_k^{(1)}n^2\\f_k^{(2)}m^2\\0\end{pmatrix},$$

where $\mathbf{f}_k = (f_k^{(1)}, f_k^{(2)}, f_k^{(3)})^T$ and the last equality follows because of symmetry.

It now follows that the Stokeslet double sum (B.1) converges if and only if we have convergence of the leading order term

$$\sum_{m=-N}^{N}\sum_{n=-N}^{N}\sum_{k=1}^{K}\left(\frac{\mathbf{f}_k+\mathbf{C}_k}{|\mathbf{n}|}\right) = \sum_{m=-N}^{N}\sum_{n=-N}^{N}\left[\frac{\sum_{k=1}^{K}\mathbf{f}_k}{8\pi(n^2+m^2)^{\frac{1}{2}}} + \frac{\begin{pmatrix}n^2\sum_{k=1}^{K}f_k^{(1)}\\m^2\sum_{k=1}^{K}f_k^{(2)}\\0\end{pmatrix}}{8\pi(n^2+m^2)^{\frac{3}{2}}}\right]$$

___
[1] Note that $\mathbf{B}_{k,\hat{\mathbf{n}}}$ and $E_{k,\hat{\mathbf{n}}}$ have odd degree in $\hat{\mathbf{n}}$ and $\mathbf{C}_{k,\hat{\mathbf{n}}}$ has even degree in $\hat{\mathbf{n}}$.

as $N \to \infty$. Therefore convergence of the Stokeslet double sum is equivalent to the zero net force condition

$$\sum_{k=1}^{K} \mathbf{f}_k = 0.$$

In case of convergence the claims about the decay rate of the tail follow readily from Eqs. (B.2) and (B.3). The function $\mathbf{L}$ is found by expanding

$$\frac{\mathbf{L(x)}}{N}$$
$$= \sum_{\max(|n|,|m|)>N} \sum_{k=1}^{K} \frac{-4D_k \mathbf{f}_k + 3E_{k,\hat{\mathbf{n}}}^2 \mathbf{f}_k + 8\mathbf{A}_k - 12D_k \mathbf{C}_{k,\hat{\mathbf{n}}} - 12E_{k,\hat{\mathbf{n}}} \mathbf{B}_{k,\hat{\mathbf{n}}} + 15E_{k,\hat{\mathbf{n}}}^2 \mathbf{C}_{k,\hat{\mathbf{n}}}}{8\,|\mathbf{n}|^3}.$$

(B.4)

It is straightforward to show that the degree of $\mathbf{L}$ is at most 2 in $\mathbf{x}$ and also that none of the quadratic terms in $\mathbf{x}$ depend on $\mathbf{x_k}$. Therefore all quadratic terms cancel because of the zero net force. $\qquad\square$

B.2 Leading order term of the error

An exact expression for $\mathbf{L}$ can be derived by expanding Eq. (B.4). The computation is purely technical so we just list the final result[2]. Since we only need compute $\mathbf{L}$ as part of the reference solution, for simplicity we limit ourselves to the case $L_x = L_y := L$. We find

$$\frac{\mathbf{L(x)}}{N} = \begin{pmatrix} S_1^{N^+} & S_2^{N^+} & S_3^{N^+} & S_4^{N^+} \end{pmatrix} \begin{pmatrix} \mathbf{a}_{11} & \mathbf{a}_{1x} & \mathbf{a}_{1y} & \mathbf{a}_{1z} \\ \mathbf{a}_{21} & \mathbf{a}_{2x} & \mathbf{a}_{2y} & \mathbf{a}_{2z} \\ \mathbf{a}_{31} & \mathbf{a}_{3x} & \mathbf{a}_{3y} & \mathbf{a}_{3z} \\ \mathbf{a}_{41} & \mathbf{a}_{4x} & \mathbf{a}_{4y} & \mathbf{a}_{4z} \end{pmatrix} \begin{pmatrix} 1 \\ x \\ y \\ z \end{pmatrix},$$

_____

[2] _see_ Mathematica notebook L.nb (also L.pdf)

where

$$\mathbf{a}_{11} = \begin{pmatrix} x_k \left(f_k^{(1)} x_k + f_k^{(2)} y_k + f_k^{(3)} z_k \right) - \frac{1}{2} f_k^{(1)} \left(x_k^2 + y_k^2 + z_k^2 \right) \\ y_k \left(f_k^{(1)} x_k + f_k^{(2)} y_k + f_k^{(3)} z_k \right) - \frac{1}{2} f_k^{(2)} \left(x_k^2 + y_k^2 + z_k^2 \right) \\ z_k \left(f_k^{(1)} x_k + f_k^{(2)} y_k + f_k^{(3)} z_k \right) - \frac{1}{2} f_k^{(3)} \left(x_k^2 + y_k^2 + z_k^2 \right) \end{pmatrix},$$

$$\mathbf{a}_{21} = \begin{pmatrix} -6 f_k^{(1)} x_k^2 - 6 f_k^{(2)} x_k y_k - 3 f_k^{(3)} x_k z_k - \frac{3}{2} f_k^{(1)} z_k^2 \\ -6 f_k^{(1)} x_k y_k - 6 f_k^{(2)} y_k^2 - 3 f_k^{(3)} y_k z_k - \frac{3}{2} f_k^{(2)} z_k^2 \\ \frac{3}{2} f_k^{(3)} x_k^2 + \frac{3}{2} f_k^{(3)} y_k^2 - 3 f_k^{(1)} x_k z_k - 3 f_k^{(2)} y_k z_k \end{pmatrix},$$

$$\mathbf{a}_{31} = \begin{pmatrix} \frac{15}{2} f_k^{(1)} x_k^2 \\ \frac{15}{2} f_k^{(2)} y_k^2 \\ 0 \end{pmatrix},$$

$$\mathbf{a}_{41} = \begin{pmatrix} 15 f_k^{(2)} x_k y_k + \frac{15}{2} f_k^{(1)} y_k^2 \\ 15 f_k^{(1)} x_k y_k + \frac{15}{2} f_k^{(2)} x_k^2 \\ 0 \end{pmatrix},$$

$$\mathbf{a}_{1x} = \begin{pmatrix} -f_k^{(1)}x_k - f_k^{(2)}y_k - f_k^{(3)}z_k \\ f_k^{(2)}x_k - f_k^{(1)}y_k \\ f_k^{(3)}x_k - f_k^{(1)}z_k \end{pmatrix}, \quad \mathbf{a}_{2x} = \begin{pmatrix} 12f_k^{(1)}x_k + 6f_k^{(2)}y_k + 3f_k^{(3)}z_k \\ 6f_k^{(1)}y_k \\ -3f_k^{(3)}x_k + 3f_k^{(1)}z_k \end{pmatrix},$$

$$\mathbf{a}_{3x} = \begin{pmatrix} -15f_k^{(1)}x_k \\ 0 \\ 0 \end{pmatrix}, \quad \mathbf{a}_{4x} = \begin{pmatrix} -15f_k^{(2)}y_k \\ -15f_k^{(2)}x_k - 15f_k^{(1)}y_k \\ 0 \end{pmatrix},$$

$$\mathbf{a}_{1y} = \begin{pmatrix} -f_k^{(2)}x_k + f_k^{(1)}y_k \\ -f_k^{(1)}x_k - f_k^{(2)}y_k - f_k^{(3)}z_k \\ f_k^{(3)}y_k - f_k^{(2)}z_k \end{pmatrix}, \quad \mathbf{a}_{2y} = \begin{pmatrix} 6f_k^{(2)}x_k \\ 6f_k^{(1)}x_k + 12f_k^{(2)}y_k + 3f_k^{(3)}z_k \\ -3f_k^{(3)}y_k + 3f_k^{(2)}z_k \end{pmatrix},$$

$$\mathbf{a}_{3y} = \begin{pmatrix} 0 \\ -15f_k^{(2)}y_k \\ 0 \end{pmatrix}, \quad \mathbf{a}_{4y} = \begin{pmatrix} -15f_k^{(2)}x_k - 15f_k^{(1)}y_k \\ -15f_k^{(1)}x_k \\ 0 \end{pmatrix},$$

$$\mathbf{a}_{1z} = \begin{pmatrix} -f_k^{(3)}x_k + f_k^{(1)}z_k \\ -f_k^{(3)}y_k + f_k^{(2)}z_k \\ -f_k^{(1)}x_k - f_k^{(2)}y_k - f_k^{(3)}z_k \end{pmatrix}, \quad \mathbf{a}_{2z} = \begin{pmatrix} 3f_k^{(3)}x_k + 3f_k^{(1)}z_k \\ 3f_k^{(3)}y_k + 3f_k^{(2)}z_k \\ 3f_k^{(1)}x_k + 3f_k^{(2)}y_k \end{pmatrix},$$

$$\mathbf{a}_{3z} = \begin{pmatrix} 0 \\ 0 \\ 0 \end{pmatrix}, \quad \mathbf{a}_{4z} = \begin{pmatrix} 0 \\ 0 \\ 0 \end{pmatrix}.$$

where $\mathbf{f} = \left(f_k^{(1)}, f_k^{(2)}, f_k^{(3)} \right)^T$, $\mathbf{x} = (x, y, z)^T$, $\mathbf{x}_k = (x_k, y_k, z_k)^T$, and

$$S_1^{N^+} = \frac{1}{L^3} \cdot \sum_{\max\{|n|,|m|\}>N} \frac{1}{(n^2 + m^2)^{\frac{3}{2}}},$$

$$S_2^{N^+} = \frac{1}{L^3} \cdot \sum_{\max\{|n|,|m|\}>N} \frac{n^2}{(n^2 + m^2)^{\frac{5}{2}}},$$

$$S_3^{N^+} = \frac{1}{L^3} \cdot \sum_{\max\{|n|,|m|\}>N} \frac{n^4}{(n^2 + m^2)^{\frac{7}{2}}},$$

$$S_4^{N^+} = \frac{1}{L^3} \cdot \sum_{\max\{|n|,|m|\}>N} \frac{n^2 m^2}{(n^2 + m^2)^{\frac{7}{2}}}.$$

In order to compute the sums we write, for instance in the case of $S_1^{N^+}$,

$$\sum_{\max\{|n|,|m|\}>N} \frac{1}{(n^2 + m^2)^{\frac{3}{2}}} = \sum_{\substack{(n,m)\neq(0,0) \\ n,m=-\infty}}^{\infty} \frac{1}{(n^2 + m^2)^{\frac{3}{2}}} - \sum_{\substack{(n,m)\neq(0,0) \\ n,m=-N}}^{N} \frac{1}{(n^2 + m^2)^{\frac{3}{2}}}.$$

On the right-hand side, the partial sum can be computed during execution depending on what N is chosen while the infinite series is independent of N and can be computed beforehand. However, computation of the infinite double sums

$$S_1 = \sum_{(n,m)\neq(0,0)} \frac{1}{(n^2 + m^2)^{\frac{3}{2}}}, \quad S_2 = \sum_{(n,m)\neq(0,0)} \frac{n^2}{(n^2 + m^2)^{\frac{5}{2}}},$$

$$S_3 = \sum_{(n,m)\neq(0,0)} \frac{n^4}{(n^2 + m^2)^{\frac{7}{2}}}, \quad S_4 = \sum_{(n,m)\neq(0,0)} \frac{n^2 m^2}{(n^2 + m^2)^{\frac{7}{2}}}. \tag{B.5}$$

is not trivial because of the slow decay of the summands. In fact, summing up to $N = 1,000$, which exploiting symmetry corresponds to adding up half a million values each, only gives the first two to three significant digits. The fast computation of accurate estimates is the goal of the next subsection (see Lemmas B.3.1 and B.3.2).

In summary we find[3]

$$S_1 = 9.033621683100950...,$$

$$S_2 = 4.516810841550475...,$$

$$S_3 = 3.745708094289508...,$$

$$S_4 = 0.771102747260967....$$

B.3 Approximation of the algebraic sums

Our goal is the fast computation of the four infinite series in Eq. (B.5). By noting that

$$S_1 = 2S_2 = 2(S_3 + S_4),$$

it becomes clear that it suffices to compute, for instance, S_2 and S_4. A closed formula for S_1 is known [CP77, Eq. (14)] and is also used in other areas of computational physics, for instance in thermodynamics [ZP78, Eq. (18)].

Lemma B.3.1. *It holds true that*

$$S_1 = 4\zeta\left(\frac{3}{2}\right)\beta\left(\frac{3}{2}\right),$$

where $\zeta(t) = \sum_{n=1}^{\infty} \frac{1}{n^t}$ is the classical Riemann zeta function and $\beta(t) = \sum_{n=0}^{\infty} \frac{(-1)^n}{(2n+1)^t}$ is the Dirichlet beta function[4].

Proof. This proof was presented to us by Tewodros Amdeberhan[5] through personal communication. Let $r_2(k)$ denote the number of ways a number $k \in \mathbb{N}$ can be written as the sum of squares of two integers. For every such pair, each permutation is

---

[3] *see* Mathematica notebook algebraicSums.nb (also algebraicSums.pdf)

[4] The Dirichlet beta function can be expressed in terms of the Hurwitz zeta function $\zeta(t, a)$ as $\beta(t) = \left(\zeta\left(t, \frac{1}{4}\right) - \zeta\left(t, \frac{3}{4}\right)\right)/4^t$, which can be evaluated efficiently in most computer algebra systems and libraries for computational mathematics.

[5] Tewodros Amdeberhan, Tulane University.

counted separately so that, for instance, $5 = (\pm 1)^2 + (\pm 2)^2 = (\pm 2)^2 + (\pm 1)^2$ implies that $r_2(5) = 8$. This allows us to write

$$S_1 = \sum_{(n,m)\neq(0,0)} \frac{1}{(n^2 + m^2)^{\frac{3}{2}}} = \sum_{k=1}^{\infty} \frac{r_2(k)}{k^{\frac{3}{2}}}.$$

By [Red96, Thm 6.8] we can write $r_2(k) = 4\sum_{d|k}\left(\frac{-4}{k}\right) = 4(1 * \left(\frac{-4}{k}\right))(k)$, where $\left(\frac{a}{b}\right)$ is the Jacobi symbol[6] . Using $\left(\frac{-4}{2k}\right) = 0$ and $\left(\frac{-4}{2k+1}\right) = (-1)^k$, it follows that

$$\sum_{k=1}^{\infty} \frac{r_2(k)}{k^{\frac{3}{2}}} = \sum_{k=1}^{\infty} \frac{4(1 * \left(\frac{-4}{k}\right))(k)}{k^{\frac{3}{2}}}$$

$$= 4\sum_{n=1}^{\infty} \frac{1}{n^{\frac{3}{2}}} \sum_{k=1}^{\infty} \frac{\left(\frac{-4}{k}\right)(k)}{k^{\frac{3}{2}}}$$

$$= 4\zeta\left(\frac{3}{2}\right) \sum_{n=0}^{\infty} \frac{(-1)^n}{(2n+1)^{\frac{3}{2}}}$$

$$= 4\zeta\left(\frac{3}{2}\right)\beta\left(\frac{3}{2}\right),$$

where we used the fact that the Dirichlet series translates arithmetic convolution to multiplication, that is $\sum \frac{(a*b)(k)}{k^s} = \sum \frac{a(k)}{k^s} \cdot \sum \frac{b(k)}{k^s}$. □

Unfortunately the presented combinatorial approach does not generalize easily to sums S_3 and S_4. Another way of evaluating the sums at least numerically is to derive equivalent expressions using Bessel functions, which have exponential decay.

---

[6] For an integer a and a prime $p \neq 2$ define the *Legendre symbol*

$$\left(\frac{a}{p}\right) = \begin{cases} 0 & \text{if } a \equiv 0 \pmod{p} \\ 1 & \text{if } a \not\equiv 0 \pmod{p}, \text{ and there exists an integer } x \text{ such that } a \equiv x^2 \pmod{p} \\ -1 & \text{there is no such } x. \end{cases}$$

Then for a positive odd integer n with prime factorization $n = p_1^{\alpha_1} p_2^{\alpha_2}...p_k^{\alpha_k}$ the *Jacobi symbol* is defined as

$$\left(\frac{a}{n}\right) = \prod_{j=1}^{k} \left(\frac{a}{p_j}\right)^{\alpha_j}.$$

For the empty product we define $\left(\frac{a}{1}\right) = 1$.

Lemma B.3.2. *Let $K_\nu(t)$ be the modified Bessel function of the second kind of degree ν. Then it holds true that*

i.

$$S_2 = \frac{4\pi^2}{9} + \frac{32\pi^2}{3} \sum_{m,n=1}^{\infty} n^2 K_2(2\pi mn),$$

ii.

$$S_4 = \frac{4\pi^2}{45} - \frac{32\pi^3}{15} \sum_{m,n=1}^{\infty} mn^3 \left(K_1(2\pi mn) + K_3(2\pi mn) \right)$$
$$+ \frac{32\pi^2}{5} \sum_{m,n=1}^{\infty} n^2 K_2(2\pi mn).$$

We present a proof that follows [LM76, Lir95], where similar sums are approximated by evaluating certain complex integrals. The equivalence of the expression for S_1 in Lemma B.3.1 with the expression for S_2 in Lemma B.3.2 is also recorded in [BGM$^+$13, Ch. 1.3, Table III]. The speed of convergence of the Bessel sums is phenomenal. Summing m and n up to 10 we recover the exact value for S_2 up to machine precision (16 digits). Before we prove Lemma B.3.2 we review a Lemma from [LM76], which unfortunately is stated there without proof.

Lemma B.3.3. *Let $m \in \mathbb{R}$ and let $F(z)$ be an even meromorphic function that decays to zero exponentially on the real axis. Then*

$$\int_0^\infty J_\nu(mt)t^{\nu+1}F(t)dt = \pi i \cdot (\text{sum of residues in } \mathbb{H} \text{ of } H_\nu^{(1)}(mt)t^{\nu+1}F(t)$$

$$\text{including one half of the residue at } 0),$$

where $\mathbb{H}$ is the complex upper half plane and $H_\nu^{(1)}(t)$ is the first Hankel function of degree ν.

Proof of Lemma B.3.2.

i. It follows from Hankel's generalization of the Lipschitz integral that [Wat66, Ch. 13.2]

$$\frac{2^\nu \Gamma\left(\nu + \frac{1}{2}\right) m^\nu}{\sqrt{\pi}\left(n^2 + m^2\right)^{\left(\nu + \frac{1}{2}\right)}} = \int_0^\infty e^{-|n|t} J_\nu(mt) t^\nu dt,$$

where $J_\nu(t)$ is the Bessel function of the first kind of order ν. Setting $\nu = 2$ and using $\Gamma\left(\frac{5}{2}\right) = \frac{3\sqrt{\pi}}{4}$ [7], gives

$$\frac{m^2}{\left(n^2 + m^2\right)^{\frac{5}{2}}} = \frac{1}{3} \int_0^\infty e^{-|n|t} J_2(mt) t^2 dt. \tag{B.6}$$

This allows us to write

$$\begin{aligned} S_2 &= \sum_{(n,m)\neq(0,0)} \frac{m^2}{\left(n^2 + m^2\right)^{\frac{5}{2}}} \\ &= 2 \sum_{m=1}^\infty \sum_{n=-\infty}^\infty \frac{m^2}{\left(n^2 + m^2\right)^{\frac{5}{2}}} \\ &= \frac{2}{3} \sum_{m=1}^\infty \int_0^\infty \sum_{n=-\infty}^\infty e^{-|n|t} J_2(mt) t^2 dt. \end{aligned}$$

From the geometric series it now follows that for $t > 0$

$$\sum_{n=-\infty}^\infty e^{-|n|t} = \frac{1 + e^t}{-1 + e^t}, \tag{B.7}$$

and hence

$$S_2 = \frac{2}{3} \sum_{m=1}^\infty \int_0^\infty J_2(mt) t^2 \frac{1 + e^t}{-1 + e^t} dt. \tag{B.8}$$

Lemma B.3.3 applies to Eq. (B.8) with $\nu = 2$ and $F(t) = \frac{1}{t} \cdot \frac{1+e^t}{-1+e^t} = \frac{1}{t} \cdot \frac{\cosh(t/2)}{\sinh(t/2)}$, which is an even function. Therefore we have to compute the residues of the function $g(z) = H_\nu^{(1)}(mz) z^2 \frac{1+e^z}{-1+e^z}$. If the reader wishes to review the theory of residues of meromorphic functions at poles, any introductory text on complex analysis will do, for instance [BC09, Sec. 73].

---

[7] This follows from $\Gamma\left(\frac{1}{2}\right) = \sqrt{\pi}$ and $\Gamma(n+1) = n\Gamma(n)$ for any positive real n [Bow58, §61].

(a) *Residue at 0:* The leading order term of $H_2^{(1)}(z)$ is $\frac{-4i}{\pi z^2}$. Therefore $g(z)$ has a simple pole at $z = 0$ and the residue is given by

$$\frac{\pi i}{2} \cdot \operatorname*{Res}_{z=0} g(z) = \frac{\pi i}{2} \lim_{z\to 0} z \left(\frac{-4i}{\pi(mz)^2} z^2 \frac{1+e^z}{-1+e^z} \right)$$

$$= \frac{\pi i}{2} \cdot \frac{-8i}{\pi m^2} \lim_{z\to 0} \frac{z}{-1+e^z}$$

$$= \frac{4}{m^2}.$$

(b) *Residues in* $\mathbb{H}$: The function $g(z)$ has simple poles at $z = 2\pi ni$ for $n = 1, 2, \dots$. Using the relation $H_\nu^{(1)}(ix) = \frac{2}{\pi} i^{-\nu-1} K_\nu(x)$, where $K_\nu(x)$ is the modified Bessel function of the second kind, gives

$$\pi i \cdot \operatorname*{Res}_{z=2\pi ni} g(z) = \pi i \lim_{z\to 2\pi ni} (z - 2\pi ni) \left(H_2^{(1)}(mz) z^2 \frac{1+e^z}{-1+e^z} \right)$$

$$= \pi i \cdot \frac{2}{\pi} i K_2(2\pi nm)(2\pi ni)^2 \cdot 2 \lim_{z\to 2\pi ni} \frac{z - 2\pi ni}{-1+e^z}$$

$$= 16\pi^2 n^2 K_2(2\pi nm).$$

Thus

$$S_2 = \frac{8}{3} \sum_{m=1}^{\infty} \frac{1}{m^2} + \frac{32\pi^2}{3} \sum_{m,n=1}^{\infty} n^2 K_2(2\pi mn)$$

$$= \frac{4\pi^2}{9} + \frac{32\pi^2}{3} \sum_{m,n=1}^{\infty} n^2 K_2(2\pi mn).$$

ii. Writing Eq. (B.6) as

$$\frac{m^2}{(n^2 x + m^2)^{\frac{5}{2}}} = \frac{1}{3} \int_0^\infty e^{-|n|\sqrt{x}\, t} J_2(mt) t^2 dt,$$

and differentiating with respect to x, gives

$$-\frac{5}{2} \cdot \frac{m^2 n^2 x}{(n^2 x + m^2)^{\frac{7}{2}}} = \frac{1}{3} \int_0^\infty -\frac{|n| t}{2\sqrt{x}} e^{-|n|\sqrt{x}t} J_2(mt) t^2 dt.$$

Note that we can switch the order of differentiation and integration by the Lebesgue dominated convergence theorem for $n \neq 0$. Also note that since the new formula trivially holds for $n = 0$, in fact it holds for all real n. Setting $x = 1$ produces

$$\frac{m^2 n^2}{(n^2 + m^2)^{\frac{7}{2}}} = \frac{1}{15} \int_0^\infty |n| e^{-|n|t} J_2(mt) t^3 dt.$$

The procedure is now analogous to above. It follows that

$$S_4 = 2 \sum_{m=1}^\infty \sum_{n=-\infty}^\infty \frac{m^2 n^2}{(n^2 + m^2)^{\frac{7}{2}}}$$

$$= \frac{2}{15} \sum_{m=1}^\infty \int_0^\infty \sum_{n=-\infty}^\infty |n| e^{-|n|t} J_2(mt) t^3 dt.$$

Differentiating the geometric series (B.7) produces

$$\sum_{n=-\infty}^\infty -|n| e^{-|n|t} = -\frac{2e^t}{(-1 + e^t)^2}, \tag{B.9}$$

which yields

$$S_4 = \frac{4}{15} \sum_{m=1}^\infty \int_0^\infty J_2(mt) \frac{t^3 e^t}{(-1 + e^t)^2} dt.$$

Once more we can use Lemma B.3.3 with $\nu = 2$ since Eq. (B.9), being the derivative of the odd function (B.7), is an even function. Therefore, we have to compute the residues of the function $g(z) = H_2^{(1)}(mz) \frac{z^3 e^z}{(-1+e^z)^2}$.

(a) *Residue at* 0: As mentioned before, the leading order term of $H_2^{(1)}(z)$ is $\frac{-4i}{\pi z^2}$,

which gives

$$
\begin{aligned}
\frac{\pi i}{2} \cdot \operatorname*{Res}_{z=0} &= \frac{\pi i}{2} \lim_{z \to 0} z \cdot \left(\frac{-4i}{\pi (zm)^2} \cdot \frac{z^3 e^z}{(-1 + e^z)^2} \right) \\
&= \frac{2}{m^2} \lim_{z \to 0} \frac{z^2 e^z}{(-1 + e^z)^2} \\
&= \frac{2}{m^2}.
\end{aligned}
$$

(b) *Residues in* $\mathbb{H}$: Note that the poles at $z = 2\pi n i$ for $n = 1, 2, ...$ are of order two. Using the relations $H_\nu^{(1)}(it) = \frac{2}{\pi} i^{-1-\nu} K_2(t)$ and $\frac{d}{dz} H_2^{(1)}(z) = \frac{1}{2} \left(H_1^{(1)}(z) - H_3^{(1)}(z) \right)$, gives

$$
\begin{aligned}
&\pi i \cdot \operatorname*{Res}_{z=2\pi n i} \\
&= \lim_{z \to 2\pi n i} \frac{d}{dz} ((z - 2\pi n i)^2 g(z)) \\
&= \pi i \cdot \left(4i\pi^3 m n^3 \left(-H_1^{(1)}(2\pi m n i) + H_3^{(1)}(2\pi m n i) \right) - 12\pi^2 n^2 H_2^{(1)}(2\pi m n i) \right) \\
&= -8\pi^3 m n^3 \left(K_1(2\pi m n) + K_3(2\pi m n) \right) + 24\pi^2 n^2 K_2(2\pi m n).
\end{aligned}
$$

Since $\sum_{m=1}^{\infty} \frac{1}{m^2} = \frac{\pi^2}{6}$, it follows that

$$
\begin{aligned}
S_4 = \ &\frac{4\pi^2}{45} - \frac{32\pi^3}{15} \sum_{m,n=1}^{\infty} m n^3 \left(K_1(2\pi m n) + K_3(2\pi m n) \right) \\
&+ \frac{32\pi^2}{5} \sum_{m,n=1}^{\infty} n^2 K_2(2\pi m n).
\end{aligned}
$$

$\square$

Bibliography

[ADE$^+$08]   J. Ainley, S. Durkin, R. Embid, P. Boindala, and R. Cortez. The method of images for regularized Stokeslets. *Journal of Computational Physics*, 227:4600–4616, 2008. doi:10.1016/j.jcp.2008.01.032.

[Bat67]   G. K. Batchelor. *An introduction to fluid dynamics*. Cambridge University Press, 1967.

[BC09]   J. W. Brown and R. V. Churchill. *Complex variables and applications*. McGraw-Hill, eighth edition, 2009.

[Bee86]   C. W. J. Beenakker. Ewald sum of the Rothe-Prager tensor. *Journal of Chemical Physics*, 85:1581–1582, 1986. doi:10.1063/1.451199.

[BGM$^+$13]   J. Borwein, L. Glasser, R. McPhedan, J. Wan, and J. Zucker. *Lattice sums then and now*. Cambridge University Press, 2013.

[Bla71a]   J. R. Blake. A note on the image system for a Stokeslet in a no-slip boundary. *Proceedings of the Cambridge Philosophical Society. Mathematical and Physical Sciences*, 70:303–310, 1971. doi:10.1017/S0305004100049902.

[Bla71b]   J. R. Blake. A spherical envelope approach to ciliary propulsion. *Journal of Fluid Mechanics*, 46(1):199–208, 1971. doi:10.1017/S002211207100048X.

[Bla72]   J. R. Blake. A model for the micro-structure in ciliated organisms. *Journal of Fluid Mechanics*, 55(1):1–23, 1972. doi:10.1017/S0022112072001612.

[Ble12]   J. Bleibel. Ewald sum for hydrodynamic interactions with periodicity in two dimensions. *Journal of Physics A: Mathematical and Theoretical*, 45(22):225002, 2012. doi:10.1088/1751-8113/45/22/225002.

[Bow58]   F. Bowman. *Introduction to Bessel functions*. Dover Publications, Inc., 1958.

[CCLH13]   C.-Y. Chen, C.-Y. Chen, C.-Y. Lin, and Y.-T. Hu. Magnetically actuated artificial cilia for optimum mixing performance in microfluidics. *Lab on a Chip*, 13:2834–2839, 2013. doi:10.1039/c3lc50407g.

[CCLV10]   R. Cortez, B. Cummins, K. Leiderman, and D. Varela. Computation of three-dimensional Brinkman flows using regularized methods. *Journal of Computational Physics*, 229:7609–7624, 2010. doi:10.1016/j.jcp.2010.06.012.

[CFM05]   R. Cortez, L. Fauci, and A. Medovikov. The method of regularized Stokeslets in three dimensions: Analysis, validation, and application to helical swimming. *Physics of Fluids*, 17(3):031504, 2005. doi:10.1063/1.1830486.

[CH14]   R. Cortez and F. Hoffmann. A fast numerical method for computing doubly-priodic regularized Stokes flow in 3D. *Journal of Computational Physics*, 258:1–14, 2014. doi:10.1016/j.jcp.2013.10.032.

[CM00]   A. J. Chorin and J. E. Marsden. *A mathematical introduction to fluid dynamics*. Springer, fourth edition, 2000.

[CN12]   R. Cortez and M. Nicholas. Slender body theory for Stokes flows with regularized forces. *Communications in Applied Mathematics and Computational Science*, 7(1):33–62, 2012. doi:10.2140/camcos.2012.7.33.

[Cor01]   R. Cortez. The method of regularized Stokeslets. *SIAM Journal on Scientific Computing*, 23(4):1204–1225, 2001. doi:10.1137/S106482750038146X.

[CP77]   A. Chaba and R. Pathria. Evaluation of lattice sums using Poisson's summation formula IV. *Journal of Physics A: Mathematical and General*, 10(11):1823–1830, 1977. doi:10.1088/0305-4470/10/11/010.

[CV15]   R. Cortez and D. Varela. A general system of images for regularized Stokeslets and other elements near a plane wall. *Journal of Computational Physics*, 285:41–54, 2015. doi:10.1016/j.jcp.2015.01.019.

[DNMNK14] Y. Ding, J. C. Nawroth, M. J. McFall-Ngai, and E. Kanso. Mixing and transport by ciliary carpets: A numerical study. *Journal of Fluid Mechanics*, 743:124–140, 2014. doi:10.1017/jfm.2014.36.

[DS09]   M. T. Downton and H. Stark. Beating kinematics of magnetically actuated cilia. *Europhysics Letters*, 85(4):44002–p1–p6, 2009. doi:10.1209/0295-5075/85/44002.

[dTO13]   J. M. den Toonder and P. R. Onck. Microfluidic manipulation with artificial/bioinspired cilia. *Trends in Biotechnology*, 31(2):85–91, 2013. doi:10.1016/j.tibtech.2012.11.005.

[EG13]   J. Elgeti and G. Gompper. Emergence of metachronal waves in cilia arrays. *Proceedings of the National Academy of Sciences*, 110(12):4470–4475, 2013. doi:10.1073/pnas.1218869110.

[FB86]   G. R. Fulford and J. R. Blake. Muco-ciliary transport in the lung. *Journal of Theoretical Biology*, 121(4):381–402, 1986. doi:10.1016/S0022-5193(86)80098-4.

[GDS09]   E. M. Gauger, M. T. Downton, and H. Stark. Fluid transport at low Reynolds number with magnetically actuated artificial cilia. *The European Physical Journal E - Soft Matter and Biological Physics*, 28:231–242, 2009. doi:10.1140/epje/i2008-10388-1.

[GLG98]   S. Gueron and K. Levit-Gurevich. Computation of the internal forces in cilia: Application to ciliary motion, the effects of viscosity, and cilia interactions. *Biophysical Journal*, 74:1658–1676, 1998. doi:10.1016/S0006-3495(98)77879-8.

[GLG99]   S. Gueron and K. Levit-Gurevich. Energetic considerations of ciliary beating and the advantage of metachronal coordination. *Proceedings of the National Academy of Sciences*, 96(22):12240–12245, 1999. doi:10.1073/pnas.96.22.12240.

[GLGLB97]   S. Gueron, K. Levit-Gurevich, N. Liron, and J. J. Blum. Cilia internal mechanism and metachronal coordination as the result of hydrodynamical coupling. *Proceedings of the National Academy of Sciences*, 94(12):6001–6006, 1997. doi:10.1073/pnas.94.12.6001.

[Has59]   H. Hasimoto. On the periodic fundamental solutions of the Stokes equations and their application to viscous flow past a cubic array of spheres. *Journal of Fluid Mechanics*, 5:317–328, 1959. doi:10.1017/S0022112059000222.

[HC]   F. Hoffmann and R. Cortez. The method of images for doubly-periodic reguarized Stokes flow. *in preparation.*

[HOdPG07]   J. P. Hernàndez-Ortiz, J. J. de Pablo, and M. D. Graham. Fast computation of many-particle hydrodynamic and electrostatic interactions in a confined geometry. *Physical Review Letters*, (140602), 2007. doi:10.1103/PhysRevLett.98.140602.

[HSB+11]   J. Hussong, N. Schorr, J. Belardi, O. Prucker, J. Rheb, and J. Westerweel. Experimental investigation of the flow induced by artificial cilia. *Lab on a Chip*, 11:2017–2022, 2011. doi:10.1039/C0LC00722F.

[Hun07]   J. D. Hunter. Matplotlib: A 2D graphics environment. *Computing In Science & Engineering*, 9(3):90–95, 2007. doi:10.1109/MCSE.2007.55.

[JOP+]   E. Jones, T. Oliphant, P. Peterson, et al. SciPy: Open source scientific tools for Python, 2001–. ☞ http://www.scipy.org/.

[KB12]   A. Keißner and C. Brücker. Directional fluid transport along artificial ciliary surfaces with base-layer actuation of counter-rotating orbital beating patterns. *Soft Matter*, 8:5342–5349, 2012. doi:10.1039/C2SM25287B.

[KdTO11] S. N. Khaderi, J. M. J. den Toonder, and P. R. Onck. Microfluidic propulsion by the metachronal beating of magnetic artificial cilia: A numerical analysis. *Journal of Fluid Mechanics*, 688:44–65, 2011. doi:10.1017/jfm.2011.355.

[KG12]   A. Kumar and M. D. Graham. Accelerated boundary integral method for multiphase flow in non-periodic geometries. *Journal of Computational Physics*, 231(20):66826713, 2012. doi:10.1016/j.jcp.2012.05.035.

[LBCL13] K. Leiderman, E. L. Bouzarth, R. Cortez, and A. T. Layton. A regularization method for the numerical solution of periodic Stokes flow. *Journal of Computational Physics*, 236:187–202, 2013. doi:10.1016/j.jcp.2012.09.035.

[Lir95]   N. Liron. Stokes flow due to infinite arrays of Stokeslets in three dimensions. *Journal of Engineering Mathematics*, 30:267–297, 1995. doi:10.1007/BF00118835.

[LL10]   C. B. Lindemann and K. A. Lesich. Flagellar and ciliary beating: The proven and the possible. *Journal of Cell Science*, 123:519–528, 2010. doi:10.1242/jcs.051326.

[LM75]   N. Liron and S. Mochon. The discrete-cilia approach to propulsion of ciliated micro-organisms. *Journal of Fluid Mechanics*, 75(3):593–607, 1975. doi:10.1017/S0022112076000402.

[LM76]   N. Liron and S. Mochon. Stokes flow for a Stokeslet between two parallel flat plates. *Journal of Engineering Mathematics*, 10(4):287–303, 1976. doi:10.1007/BF01535565.

[Lor96]   H. A. Lorentz. A general theorem concerning the motion of a viscous fluid and a few consequences derived from it. *Zittingsverslag van de Koninklijke Akademie van Wetenschappen teAmsterdam*, 5:168–175, 1896. doi:10.1007/BF00118821. Translation into English: Journal of Engineering Mathematics 30:19-24, 1996.

[LR06]   P. Lenz and A. Ryskin. Collective effects in ciliar arrays. *Physical Biology*, 3:285–294, 2006. doi:10.1088/1478-3975/3/4/006.

[LT10]   D. Lindbo and A.-K. Tornberg. Spectrally accurate fast summation for periodic Stokes potentials. *Journal of Computational Physics*, 229:8994–9010, 2010. doi:10.1016/j.jcp.2010.08.026.

[LT11]   D. Lindbo and A.-K. Tornberg. Fast and spectrally accurate summation of 2-periodic Stokes potentials. 2011. ☞ http://arxiv.org/abs/1111.1815.

[Mit07]   S. M. Mitran. Metachronal wave formation in a model of pulmonary cilia. *Computers and Structures*, 85:763–774, 2007. doi:10.1016/j.compstruc.2007.01.015.

[MN06]   W. F. Marshall and S. Nonaka. Cilia: Tuning in to the cell's antenna. *Current Biology*, 16(15):604–614, 2006. doi:10.1016/j.cub.2006.07.012.

[OV11]   N. Osterman and A. Vilfan. Finding the ciliary beating pattern with optimal efficency. *Proceedings of the National Academy of Sciences*, 108(38):15727–15732, 2011. doi:10.1073/pnas.1107889108.

[Poz92]   C. Pozrikidis. *Boundary integral and singularity methods for linearized viscous flow.* Cambridge University Press, 1992.

[Poz96]   C. Pozrikidis. Computation of periodic Green's functions of Stokes flow. *Journal of Engineering Mathematics*, 30:79–96, 1996. doi:10.1007/BF00118824.

[Poz97]   C. Pozrikidis. *Introduction to Theoretical and Computational Fluid Dynamics.* Oxford University Press, 1997.

[Pur77]   E. M. Purcell. Life at low Reynolds number. *American Journal of Physics*, 45(1):3–11, 1977. doi:10.1063/1.30370.

[Red96]   D. Redmond. *Number theory - An introduction.* Marcel Dekker Inc., 1996.

[SB01]   A. Sierou and J. F. Brady. Accelerated Stokesian dynamics simulations. *Journal of Fluid Mechanics*, 448:115–146, 12 2001. doi:10.1017/S0022112001005912.

[SBG08]   D. Smith, J. R. Blake, and E. A. Gaffney. Fluid mechanics of nodal flow due to embryonic primary cilia. *Journal of the Royal Society Interface*, 5:567–573, 2008. doi:10.1098/rsif.2007.1306.

[SDS05]   D. Saintillan, E. Darve, and E. S. G. Shaqfeh. A smooth particle-mesh Ewald algorithm for Stokes suspension simulations: The sedimentation of fibers. *Physics of Fluids*, 17(3):033301, 2005. doi:10.1063/1.1862262.

[SFE+10]   A. R. Shields, B. L. Fiser, B. A. Evans, M. R. Falco, S. Washburn, and R. Superfine. Biometric cilia arrays generate simultaneous pumping and mixing regimes. *Proceedings of the National Academy of Sciences*, 107(36):15670–15675, 2010. doi:10.1073/pnas.1005127107.

[SGB07] D. Smith, E. A. Gaffney, and J. R. Blake. Discrete cilia modelling with singularity distributions: Application to the embryonic node and the airway surface liquid. *Bulletin of Mathematical Biology*, 69:1477–1510, 2007. doi:10.1007/s11538-006-9172-y.

[SS81] M. J. Sanderson and M. A. Sleigh. Ciliary activity of cultured rabbit tracheal epithelium: Beat pattern and metachrony. *Journal of Cell Science*, 47:331–347, 1981.

[Tay51] G. Taylor. Analysis of the swimming of microscopic organisms. *Proceedings of the Royal Society, London*, 209:447–461, 1951. doi:10.1098/rspa.1951.0218.

[VPK+10] M. Villfan, A. Potočnik, B. Kavačič, N. Osterman, I. Poberaj, A. Vilfan, and D. Babič. Self-assembled artificial cilia. *Proceedings of the National Academy of Sciences*, 107(5):1844–1847, 2010. doi:10.1073/pnas.0906489107.

[Wat66] G. N. Watson. *A treatise on the theory of Bessel functions*. Cambridge University Press, second edition, 1966.

[WCF14] J. K. Wróbel, R. Cortez, and L. Fauci. Modeling viscoelastic networks in Stokes flow. *Physics of Fluids*, 26(113102), 2014. doi:10.1063/1.4900941.

[WGW+13] Y. Wang, Y. Gao, H. Wyss, P. Anderson, and J. den Tonder. Out of the cleanroom, self-assembled magnetic artificial cilia. *Lab on a Chip*, 13:3360–3366, 2013. doi:10.1039/c3lc50458a.

[WGW+14] Y. Wang, Y. Gao, H. M. Wyss, P. D. Anderson, and J. M. J. den Toonder. Artificial cilia fabricated using magnetic fiber drawing generate substantial fluid flow. *Microfluid Nanofluid*, 2014. doi:10.1007/s10404-014-1425-8.

[ZP78] C. Zasada and R. Pathria. Statistical thermodynamics of superfluid helium confined to a cuboidal enclosure below 0.5K. *Journal of Physics A: Mathematical and General*, 12(9):1531–1539, 1978. doi:10.1088/0305-4470/12/9/020.

Index

Biography

The author was born in Freiberg (Sachsen), Germany, in 1986 and studied mathematics at Technische Universität Darmstadt in Darmstadt, Germany, from April 2006 until August 2010, when he graduated with a graduate degree in mathematics (Diplom in Mathematik). The author was enrolled at Tulane university during the academic year 2008-09 as an exchange student and earned an MS in mathematics in August 2009. The author started the PhD program at the Tulane University mathematics department in August 2010, eventually completing the program in May 2015.